Growth and Characterisation of Wide-bandgap γ-CuCl on near lattice-matched Si

By

Lisa O'Reilly, B.A. (Mod)

Thesis Submitted for the Degree of

Doctor of Philosophy

Research Supervisor

Prof. Patrick J. McNally

Dublin City University

School of Electronic Engineering

May, 2006

I hereby certify that this material, which I now submit for assessment on the programme of study leading to the award of Doctor of Philosophy is entirely my own work and has not been taken from the work of others save and to the extent that such work has been cited and acknowledged within the text of my work.

Signed: Lisa O'Reilly ID No.: 52163041
Candidate

Date: 5th May 2006

Acknowledgments

I am indebted to my supervisor, Prof Patrick J McNally for his support, encouragement and advice throughout this PhD His energy and enthusiasm for this work and unwavering confidence in me, inspired me to persevere, even when it seemed like the problems were never-ending

I appreciate the help of the electronic engineering technical staff, Liam Meany, Conor Maguire, Ger Considine and Paul Wogan and also Michael May of the mechanical engineering department I am especially grateful to Robert Clare and Billy Roarty who came to my assistance almost on a daily basis and never complained about it!

Thanks to Alec Reader, a fountain of knowledge on semiconductors, whose experience and guidance helped to solve many puzzles Thanks also to David Cameron for his support in the lab as well as many helpful discussions, and to Stephen Daniels for adopting the CuCl project in its later stages, bringing some new ideas to the group

I am grateful to Ger Lardner for her continual encouragement and advice since my arrival in DCU and for reminding me to take care of my PhD before worrying about anything else

I value the support of Gomathi and Francis, who truly understand the joys and heartache of working with CuCl Thanks also to Xu Lu for keeping me company in the lonely basement!

Thanks to Andreas Danilewsky (Dany) for his interest and enthusiasm in the CuCl project, for welcoming me to Freiburg and for patiently explaining the workings of Orient Express to me on more than one occasion

My collaborators in Trinity College, Anirban Mitra, Miguel Martinez-Rosas and Louise Bradley are gratefully acknowledged for performing the invaluable photoluminescence measurements

I acknowledge Enda McGlynn of the Physics department for being a thorough internal examiner and for the use of the Hall effect system Thanks to James Fryar for performing luminescence and reflectivity measurements and to Jean-Rene Duclere for his help and advice on electrical measurements

My dinner-cooking, fashion consultant sister Paula deserves a special mention for looking after me so well throughout my studies and along with Mary for putting up with me being such an anti-social housemate especially during the very long write-up period

Finally, thanks to my sister Sandra for never complaining about my long-term "struggling-student" status and to my parents for their absolute faith in me

Abstract

Growth and Characterisation of Wide-bandgap γ-CuCl on near lattice-matched Si

Lisa O'Reilly

The need for blue and ultra-violet (UV) solid-state emitters and detectors has propelled the investigation of several wide-bandgap semiconducting materials γ-CuCl is a wide-bandgap (E_g = 3 395eV at 4 K), direct bandgap, semiconductor material with a cubic zincblende lattice structure A very large exciton binding energy (190meV), assures efficient exciton based UV emission at room temperature Its lattice constant, a_{CuCl} = 0 541 nm means that the lattice mismatch to Si (a_{Si} = 0 543 nm) is <0 5% implying that low defect-density heteroepitaxy of CuCl on Si should be possible

γ-CuCl on Si - the growth of a wide-bandgap, direct bandgap, optoelectronics material on silicon substrate is a novel material system, with compatibility to current Si based electronic/optoelectronics technologies Polycrystalline γ-CuCl thin films are grown on Si (111), Si (100), and glass substrates by physical vapour deposition X-ray diffraction (XRD) studies confirm that CuCl has a cubic zincblende structure with a preferred (111) orientation Importantly, chemical interactions between CuCl and Si are eliminated

Photoluminescence (PL) and cathodoluminescence (CL) results for CuCl, deposited on either (100) or (111) Si, reveal a strong room temperature Z_3 excitonic emission at ~ 387nm We have developed and demonstrated the room temperature operation of an ultra-violet electroluminescent device fabricated by the growth of γ-CuCl on Si Electroluminescence measurements confirm UV light emission at wavelengths of ~380nm and ~387nm, due to excitonic behaviour A further emission occurs in the bandgap region at ~360nm

The most efficient solid-state emitters are p-n junctions, therefore research on the possibility of doping CuCl is of great interest The impact on structural, optical and electrical properties of CuCl by incorporation of Zn for n-type doping, by co-evaporation of CuCl and $ZnCl_2$ is investigated Electrical measurements indicate n-type conductivity with resistivity ~ 34Ωcm

Table of Contents

Chapter 1
Introduction

Chapter 2
Characterisation Techniques

Chapter 3
Structural Properties of CuCl

Chapter 4
Optical Properties of CuCl

Chapter 5
Electrical Properties and Doping of CuCl

Chapter 6
Conclusions and Future Work

Appendix A
Characterisation of Si-SiGe Heterostructures using Micro-Raman Spectroscopy and Synchrotron X-Ray Topography

Appendix B
Micro-Raman Study of Self-Assembled Ge Quantum Dots on Silicon

List of Publications

I “Impact on structural, optical and electrical properties of CuCl by incorporation of Zn for n-type doping” L O’Reilly, A Mitra, Gomathi Natarajan, O F Lucas, P J McNally, S Daniels, D C Cameron, A L Bradley and A Reader, *J Cryst Growth* **287**, 139-144 (2006)

II “Room-temperature ultraviolet luminescence from γ-CuCl grown on near lattice-matched silicon” L O’Reilly, O F Lucas, P J McNally, A Reader, Gomathi Natarajan, S Daniels, D C Cameron, A Mitra, M Martinez-Rosas, and A L Bradley, *J Appl Phys* **98** (11), 113512 (2005)

III “Growth and characterisation of wide-bandgap I-VII optoelectronic materials on silicon” L O'Reilly, G Natarajan, P J McNally, D Cameron, O F Lucas, M Martinez-Rosas, L Bradley, A Reader and S Daniels, *J Mater Sci Mater Electron* , **16** (7), 415-419 (2005)

IV “The use of wide-bandgap CuCl on silicon for ultra-violet photonics” L O'Reilly, G Natarajan, P J McNally, S Daniels, O F Lucas, A Mitra, M Martinez-Rosas, L Bradley, A Reader and D Cameron, *Opto-Ireland 2005 Optoelectronics, Photonic Devices, and Optical Networks, SPIE Proc* **5825**, 29-36 (2005)

V “Encapsulation of the heteroepitaxial growth of wide band gap gamma-CuCl on silicon substrates” F O Lucas, L O’Reilly, G Natarajan, P J McNally, S

Daniels, D M Taylor, S William, D C Cameron, A L Bradley, A Miltra, *J Cryst Growth* **287**, 112-117 (2006)

VI "Structural and optoelectronic properties of sputtered copper (I) chloride", G Natarajan, L O'Reilly, S Daniels, D C Cameron, P J McNally, O Lucas, A Reader, A Mitra, L Bradley, *Opto-Ireland 2005 Optoelectronics, Photonic Devices, and Optical Networks, SPIE Proc* **5825**, 364-369 (2005)

VII "Structural and Compositional Evolution of Self-Assembled Germanium Islands on Silicon (001) During High Growth Rate LPCVD", G D M Dilliway, N E B Cowern, C Jeynes, L O'Reilly, P J McNally, D M Bagnall, *Mat Res Soc Symp Proc*, **775**, 275-280, (2003)

VIII "Defectivity study of Cu metallization process by dark-and bright field inspection", L Carbonell, F Holsteyns, Z Tokei, L O'Reilly, K Maex and P Mertens, *Ultra Clean Processing of Silicon Surfaces V, Solid State Phenomena* **92**, 281-285 (2003)

IX "Synchrotron X-ray topographic study of dislocations and stacking faults in InAs", A Lankinena, T Tuomi, J Riikonen, L Knuuttila, H Lipsanen, M Sopanen, A Danilewsky, P J McNally, L O'Reilly, Y Zhilyaev, L Fedorov, H Sipila, S Vaijarvi, R Simon, D Lumb and A Owens, *J Cryst Growth*, **283** (3-4), 320-327 (2005)

X Synchrotron X-ray topography study of defects in indium antimonide P-I-N structures grown by metal organic vapour phase epitaxy, J Riikonen, T Tuomi, A Lankinen, J Sormunen, A Saynatjoki, L Knuuttila, H Lipsanen, P J McNally, L O'Reilly, A Danilewsky, H Sipila, S Vaijarvi, D Lumb and A Owens, *J Mater Sci Mater Electron*, **16** (7), pp 449-453 (2005)

Author's Contribution

The author played a major role in the preparation of manuscripts for publications I- IV and assisted in the experimental work for publications V and VI Results of characterisation performed by the author are included in publications VII and VIII The author participated in synchrotron x-ray topography experiments reported in IX and X

List of Figures

Chapter 1

Chapter 2

Chapter 3

Chapter 4

Chapter 5

Appendix A

Appendix B

List of Tables

Chapter 1

Introduction

1.1 Wide-Bandgap Semiconductors

The past decade has seen an explosion of research, development and production interest in wide-bandgap semiconductors This interest has focussed on the production of blue and ultra-violet light emitting and solid-state laser diodes The search for optoelectronics devices, operating in the energy range of >3 eV, is an important one, as it leads to considerable technical advantages in electronic storage because the density of optical storage, in optical disc systems (e g CD-ROMs, DVDs) increases as the wavelength of the laser light decreases [1] Other applications include the production of white light arrays (using red, green and blue pixels), ultra-violet lasers and UV sensors There are numerous applications for UV sensors such as biological and chemical sensors, flame sensors, optical communications and UV emitter calibration [2]

Much of the research has been concentrated on variants of the III-Nitride, III-V and II-VI compounds The ability to fabricate devices emitting in the blue-UV portion of the electromagnetic spectrum is the result of the large direct bandgap in these materials (3 – 6 eV) The wide-bandgap of ZnO (3 3eV at room temperature [3]) and its binding energy of 60meV for the free exciton[a] have prompted much investigation of this semiconductor However it has proven difficult to produce high-conductivity

---

[a] An exciton is formed from a free electron in the conduction band and hole in the valence band bound together by a Coulombic attraction such that the electron can orbit about the hole as if this were a hydrogen-like atom

p-type ZnO [4] It is the III-Nitride materials which have become synonymous with blue-violet light emitting and laser diodes [5] These materials also possess high electron mobilities, high breakdown electric fields and good thermal conductivities

GaN and its related alloys are hexagonally co-ordinated crystals, which are not usually grown as single wafers, due to the severe difficulty of so doing Instead, these are grown epitaxially in thin single crystal layers on suitable substrates, typically α-Al_2O_3 (sapphire) or SiC The main problem with this is that there are large lattice constant differences between the epilayers and the substrate For example, in the case of GaN epitaxy on (0001) Al_2O_3, the lattice misfit is as high as 13 9% [6] This leads to the generation of misfit dislocations with densities reported to be as high as 10^{10} cm^{2}, which are deleterious to the performance of light emitting devices produced thereupon [7,8,9] Despite this problem these materials have developed rapidly with much of the research to date focussing on improvements in the epitaxial techniques (e g epitaxial lateral overgrowth and pendeo-epitaxy) for growing the III-Nitride on the highly mismatched substrate and hence reducing the misfit dislocation density

By 1997, Nichia Chemical Industries Ltd in Japan had succeeded in the commercial production of high-brightness blue/green light emitting diodes (LEDs) with a luminous intensity of 12cd [10,11] In addition, room temperature violet laser emission in InGaN based multi-quantum well heterostructures has been demonstrated under pulsed and continuous wave operation conditions [1,12] However, these early devices were, and indeed still are, plagued by the presence of numerous threading dislocations (TDs), which impacted severely on the lifetimes and optical performance of laser diodes (LDs) in particular These densities reached values as high as ~10^{10}

cm^{2}, and were due mainly to the severe lattice mismatch between the substrate materials (e g 6H-SiC or Al_2O_3) and the grown III-Nitride epilayers The introduction of epitaxial lateral overgrowth (ELOG) techniques [13,14] has facilitated the production of III-Nitride films with threading dislocation densities reduced by 3-4 orders of magnitude with respect to conventional metalorganic chemical vapour deposition techniques on both sapphire and SiC substrates [8,9]

Studies of the optical properties of ELOG GaN [15,16] have indicated that there is a clear improvement in the optical quality of the GaN materials in the area of lateral epitaxial overgrowth Also, reducing the TD density has been shown to reduce the reverse leakage current by up to 3 orders of magnitude in GaN p-n junctions [17], InGaN single [9] and multiple quantum well LEDs [18] and GaN/AlGaN heterojunction field effect transistors [19] fabricated on ELOG GaN

In the standard ELOG technique, a GaN layer 2-3μm thick is grown on the sapphire substrate by metal-organic chemical vapour deposition (MOCVD), the sample is then patterned and a second MOCVD growth is performed If instead the GaN is grown on patterned sapphire substrates only one MOCVD growth is needed and a reduction in threading dislocation density and improved electroluminescence output of the resulting LEDs was reported [20,21]

Other researchers have investigated the lateral growth of GaN films suspended from $\{11\bar{2}0\}$ sidewalls of an aligned series of [0001] oriented GaN columns or trenches using the metal-organic vapour phase epitaxy (MOVPE) technique, without the use of, or contact with, a supporting mask or substrate (as in ELOG) [22,23] This technique has become known as *pendeo-epitaxy* and it also serves to reduce TD densities to 10^4-10^5 cm^{2} – many orders of magnitude lower than bulk GaN, but still very high compared to mature technologies such as Si or GaAs

In 1998 Nakamura *et al* reported an InGaN multi-quantum well-structure laser diode with a lifetime of more than 1150 hours under room-temperature continuous-wave operation [13] This drastically improved on the lifetime of 35 hours previously reported [11], and was thought to be mainly due to the reduction in dislocation density arising from the use of the ELOG substrate However, for applications such as read/write laser light sources of DVD's, laser diodes are required to have higher power and a longer lifetime An InGaN multi-quantum-well laser diodes with an output power of 30mW and an estimated lifetime of 15,000 hours at a case temperature of 60°C has been recently reported [24] The improved laser diode lifetime was attributed to a reduction in dislocation density to 7 x 10^5 cm^{2} by using a GaN substrate with ELOG However, large volume production of these lasers would be limited by the lack of available high quality GaN substrates

In the past few years a number of research groups have been investigating the possibility of merging the ultraviolet capabilities of group III nitrides into the existing silicon microelectronics industry by attempting to grow III-Nitride epilayers on a Si substrate Examples of technological advantages include the ability to develop nitride-based short wavelength ultraviolet pixelated LED arrays on cheap Si substrates, which in conjunction with organic colour converters can create small, full colour, high resolution displays [25] GaN and AlGaN ultraviolet photo detectors on a silicon substrate have already been grown and characterised [26,27] As well as the obvious advantages of combining the optoelectronic properties of GaN with advanced Si electronic devices, Si substrates possess many advantages over the substrates conventionally used to grow GaN such as insulating sapphire and expensive SiC Low cost, large area silicon wafers with high crystalline perfection are widely available, and silicon has well-developed handling and packaging methods [28,29,30,31,32] Also, the good electrical conductivity of silicon substrates makes it attractive for devices operating at a high current density because the ohmic contacts can be formed on the substrate [30]

One favoured substrate has been Si (111), as this surface has a 120° symmetry that is somewhat compatible with the hexagonal III-Nitrides The (0001) plane of GaN is almost parallel to the (111) plane of Si, and the [11$\bar{2}$0] direction of GaN is parallel to the [1$\bar{1}$0] direction of Si [33] This route is proving difficult, as the difference in lattice parameters (lattice mismatch between GaN and Si is 17%) and the strength of the Si-N bond prevents the formation of smooth, single crystal GaN on Si (111) [34,35] To some extent this has been alleviated by using a two-step method involving various buffer layers such as SiC [30,36,37], GaN [38], AlN [25,29,33,39,40], GaAs [41], AlO_x, [42] and SiN_x [43] These typically yield smooth morphologies and columnar microstructures with a TD density of around 10^{10} cm^{2} – comparable to the quality of films grown on sapphire but no real advance

For an easier integration of GaN-based devices with mainstream silicon technology, growth on the more widely used Si (100) substrate would be preferred A small number of researchers have attempted to grow GaN on Si (100) substrates [28,31,44] but again the films are of poor quality with the occurrence of cracks, stacking faults and TDs even with the use of a buffer layer Some improvement in this area has been achieved recently, and the growth of single domain GaN on Si (100) was realized by metalorganic vapour-phase epitaxy (MOVPE) using a high temperature AlN seed layer on a Si (100) substrate with an off-orientation of 4° towards the Si [110] direction [45] Advances in growth have lead to the development of the first GaN field-effect-transistors on Si (100) substrates, which were reported in the last year [46]

The principal weakness of these approaches lies in the fact that the additional heteroepitaxial layer does not necessarily alleviate mismatch problems due to the fundamental incompatibility of hexagonal III-Nitrides and cubic Si or GaAs Almost all results showed that the epitaxial film has a high density of dislocations and cracks A bottom line has emerged the reduction of deleterious threading dislocations in wide-bandgap materials for optoelectronics devices is essential to their operation and in particular to their longevity The lattice mismatch between the substrate materials and the overgrown epilayers is the main culprit This project proposes a radically different approach in the field of wide-bandgap optoelectronics, investigating the growth of lattice matched CuCl on cubic Silicon

1.2 Physical Properties of CuCl

The cuprous halides, e g CuCl, CuBr, CuI, are ionic I-VII compounds with the zincblende ($T_d^2, F\bar{4}3m$) structure at room temperatures [47] At room temperature and atmospheric pressure, the prevalent phase of CuCl is called γ-CuCl γ–CuCl is a wide-bandgap, direct bandgap, semiconductor material, with a cubic zincblende lattice structure. The zincblende lattice is composed of two interpenetrating f.c.c. (face-centred-cubic) sublattices occupied by Cu^+ and Cl^- atoms respectively (Fig 1.1).

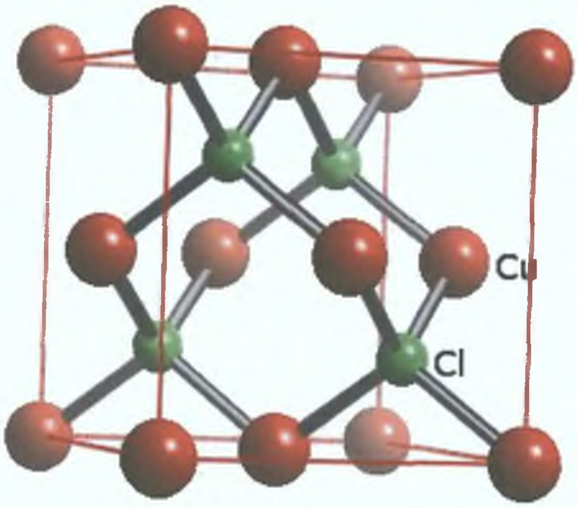

Fig. 1.1 Cubic zincblende lattice structure of CuCl unit cell [48]

If all zincblende lattice points are occupied with identical atoms, (e.g. in the case of group IV elemental semiconductors) it becomes the diamond (O_h^7) structure. The unit cell contains four CuCl molecules. Each Cu atom is surrounded by a regular tetrahedron built by four Cl atoms (and vice versa), at a nearest-neighbour distance of $\frac{a\sqrt{3}}{4}$, where a is the lattice constant [49]. The second nearest-neighbours are twelve atoms of the same kind at a distance of $\frac{a\sqrt{2}}{4}$. A notable feature of this structure is the lack of an inversion or symmetry centre; therefore the possibility exists for electro-optic (Pockels) effects [50].

The lattice constant, $a_{\mathrm{CuCl}} = 0.541$ nm, means that the lattice mismatch to Si ($a_{\mathrm{Si}} = 0.543$ nm) is <0.5%. Silicon is clearly a suitable substrate for the low defect density heteroepitaxy of γ–CuCl The diamond structure is equivalent to the zincblende structure and the lattice constants of Si and CuCl are closely matched As discussed above, the threading dislocations in GaN are caused by a fundamental incompatibility with the available substrates, therefore a similar problem should not arise in the case of CuCl on Si Although there is quite a large difference in the coefficient of thermal expansion of Si and CuCl, i e 2 59 x 10^{6}K^{1} and 13 80 x 10^{6}K^{1}, respectively [51], compared to the growth temperature of GaN on Si, ~ 1000°C, it is possible to grow CuCl on Si at very low temperatures, typically < 200°C and a single crystal CuCl thin film has even been grown on Si at room temperature [52] Interestingly CuCl exhibits a strongly negative coefficient of thermal expansion at temperatures below 100K [53]

Another widely available semiconductor with mature technology is GaAs Given that the lattice constant for zincblende GaAs is a_{GaAs} = 0 565 nm, growth of γ-CuCl on GaAs may also be possible as the lattice misfit of CuCl is ~ 4% with respect to (100) GaAs The ionicity of CuCl is 0 75 on the Phillips scale [54], which is close to the maximum found for zincblende materials (the critical value f_c = 0 785 marks the idealised boundary dividing compounds characterised by the fourfold-coordinated crystal structures and those with six fold-coordinated rock salt type structures [55]), while that of GaAs and Si is 0 31 and 0, respectively [56,57] This also suggests that studies of the growth of γ-CuCl on GaAs may be profitable as it could be possible to form strong ionic bonds at the GaAs-CuCl interface This material combination is not investigated in this work, but it illustrates the potential existing for related research

The melting point of γ-CuCl is ~ 430°C and its boiling point is ~1490°C [48,58] Since this melting point is significantly lower than that of Si (1414°C), it may be possible to grow γ-CuCl on Si (and also GaAs, m p =1240°C) using liquid phase epitaxy

One challenge associated with the use of CuCl is that it is sensitive to moist air Under the influence of light and moisture, hydrated oxyhalides of Cu^{++} are formed [49] This reaction can be easily recognised by a colour change in CuCl associated with the presence of the greenish colour Cu^{++} ions Auger spectroscopy has confirmed the presence of oxygen in CuCl crystals [59] Suitable storage conditions are therefore necessary to prolong the lifetime of CuCl and ultimately a protective layer will be needed to prevent this reaction

1.3 Growth of CuCl

Early work on the growth of CuCl crystals took place in the 1960s using various crystal growth techniques such as gel growth [60,61,62,63], Stockbarger growth [64], Bridgman method [65,66,67], Czochralski growth [68], growth from aqueous solution [69] and growth by the travelling heater method [70,71] This work was mainly motivated by the electro-optical properties and wide transmission range (0 4μm-20μm) of CuCl, which make it a suitable material for laser modulation [72]

As CuCl is cooled below its melting point (≈430°C) it crystallises in a hexagonal wurtzite phase known as β-CuCl As further cooling occurs, CuCl undergoes a solid-state phase transition at ~ 407°C from the β-CuCl phase, to the cubic zincblende γ-CuCl phase [49] This creates difficulties in the growth of large, strain-free, cubic CuCl crystals from the melt [68,73,74] as a volume change occurs during the transition causing stress, which can be released by the formation of grain boundaries, hence forming polycrystalline material The lattice constants of β-CuCl are *a*=0 391 nm and *c*=0 642 nm [49], therefore the volume of the hexagonal unit cell is approximately 53% of the volume of the cubic CuCl unit cell However, CuCl forms eutectics[b] with numerous halides and the addition of small amounts of these compounds (1 8-15 mole %) can be used to lower the melting point of the CuCl/flux mixture below the phase transition temperature resulting in the growth of higher quality crystals The most commonly used compounds for flux growth of γ-CuCl are KCl [64,65,66,67,68,70,71,73,74], $SrCl_2$ [65,70,73], $PbCl_2$ [65,68,73] and $BaCl_2$ [65,70,73] Phase diagrams for KCl-CuCl, $SrCl_2$-CuCl, $PbCl_2$-CuCl and $BaCl_2$-CuCl are given by Parker and Pinnell [73] The KCl-CuCl phase diagram is shown in figure 1 2 below

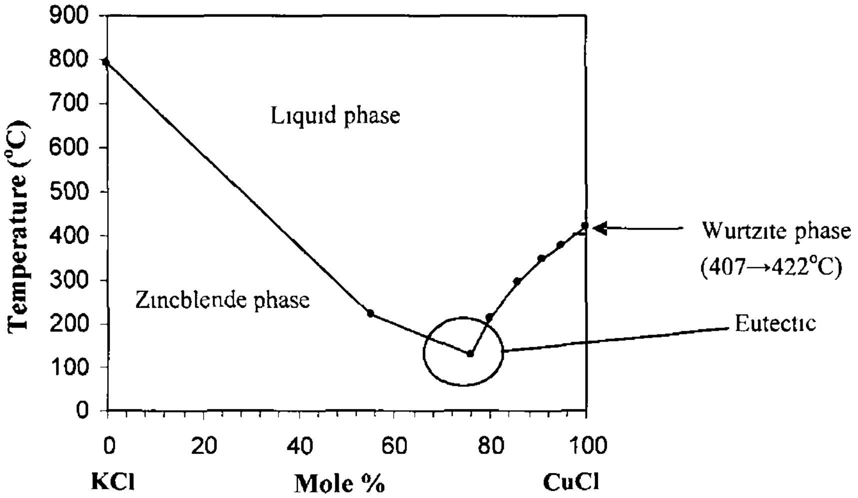

Fig 1 2 Phase Diagram for KCl-CuCl system [73]

---

[b] A eutectic is a mixture of two or more elements which has a lower melting point than any of its constituents The eutectic point appears as a 'V' in the phase diagram, giving the lowest temperature at which the mixture of materials will melt

It can clearly be seen that addition of just a few mole percent of KCl to CuCl suppresses the melting point of CuCl to below the solid-state phase transition temperature of 407°C, and by adding approximately 20 mole per cent KCl the melting point of CuCl is lowered to below 150°C However it has been reported that greater impurity content in the CuCl crystal will result in poorer optical and electrical properties, therefore growth conditions are most favourable at a temperature just below the phase transition temperature [70]

Over the past decade or so, research on CuCl growth mechanisms has focussed on surface studies involved in the heteroepitaxy of CuCl single crystals on a number of substrates Growth studies have involved the use of reflection high-energy electron diffraction during molecular beam epitaxy (MBE) of CuCl on MgO (001) [75,76] and CaF_2 (111) [77] and low energy electron diffraction (LEED) during MBE on reconstructed (0001) haematite (α-Fe_2O_3) [78] One group of researchers has examined the surface growth mechanisms in the heteroepitaxy of single crystalline films of CuCl on both Si and GaAs substrates by MBE [56] Again, this study focussed on the fundamental physics of the island growth process and the nature of the interfacial bonding Angle-resolved photoelectron spectroscopy has also been used to examine the surface electronic states for a CuCl (100) single crystalline film grown on a Si (100) surface [52]

1.4 Electronic Properties of CuCl

CuCl has a direct band structure with the top of the valence band and the bottom of the conduction band at **k**=0 The bandgap, E_g = 3 395eV at 4K [51], corresponds to light emission at a wavelength ~ 366nm (the ultra-violet to violet region in the electromagnetic spectrum) The valence bands of I-VII semiconductors originate from the filled d^{10} shell of the $metal^+$ ions and the s^2p^6 rare gas configuration of the halogen ions The electronic configuration of Cu is [Ar] $3d^{10}$ $4s^1$ and that of Cl is [Ne] $3s^2$ $3p^5$ The halogen s-levels are situated more than 10eV below the p-levels and hence form a rather isolated s-like band, which is the predominant contribution to the lowest conduction band level The spatial extent of the d-levels is large and their energies are close to those of the p-levels of the halogen In the case of CuCl this leads to a strong hybridization of the d-levels of Cu with the p-levels of Cl, dramatically increasing the number of valence electrons per unit formula from 8 to 18 This has a significant effect on the physical and electronic properties of CuCl, especially compared to III-V or II-VI group semiconductors in which the valence bands are derived from an s^2p^6 configuration One result of the p-d mixing in CuCl is its non-linear optical properties [79] Second order non-linear optical effects in CuCl could lead to practical devices such as second harmonic generators, tunable parametric oscillators and optical mixers [49] Further evidence of the importance of the Cu d-levels compared to the p-levels is that the band gaps of the Cu-halides differ by less than 0 3eV, despite the fact that the p-levels of the isoelectronic anions Cl, Br and I differ by about 2eV, i e the anion levels have only a small influence on the band gap [80]

As shown schematically in fig 1 3, in the CuCl zincblende structure the top of the valence band (Γ_{15}[c]) is triply degenerate without spin-orbit splitting The spin-orbit interaction results in the splitting of the p-d mixed Γ_{15} state into a twofold degenerate

---

[c] Γ_{15} Γ_6 Γ_7 and Γ_8 are irreducible representations of the space group T_d^2 at the Γ point

Γ_7 state at the uppermost valence band and the next lower, fourfold degenerate valence band exhibiting Γ_8 symmetry When subjected to a crystal field of T_d symmetry, the orbital d-levels split into one twofold degenerate Γ_{12} level, and two Γ_{15} levels, which hybridize with the chlorine p-levels resulting in two threefold degenerate Γ_{15} levels

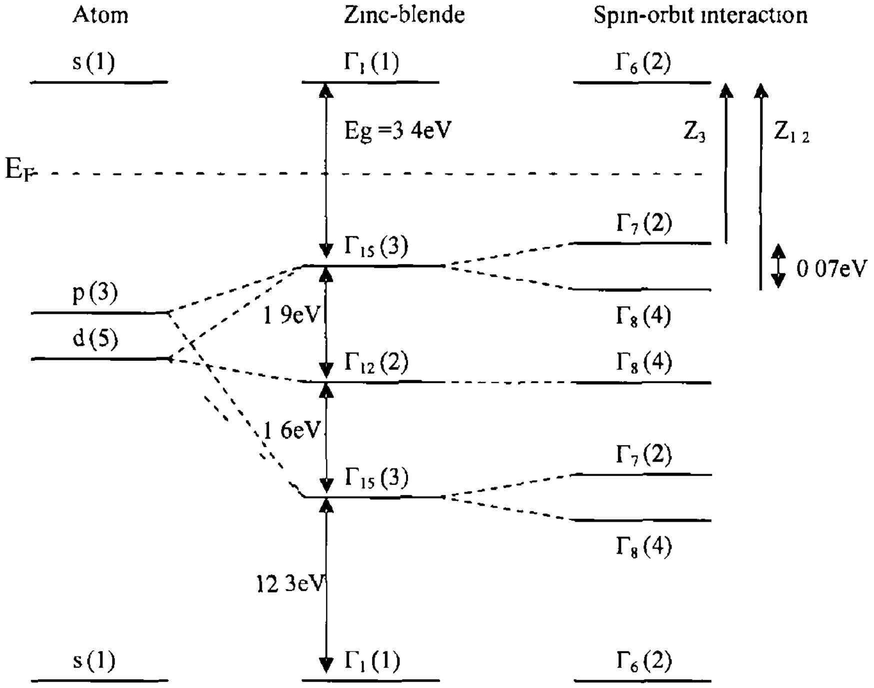

Fig 1 3 Schematic development of conduction and valence states due to s, p and d electrons at the Brillouin Zone Centre Γ in the cubic crystal field of the zincblende structure (not to scale) Energies given are experimental results for CuCl [81,82] The numbers in brackets indicate the degeneracy of the corresponding state

Coupling of the lowest conduction band state Γ_6 to both the uppermost valence band holes Γ_7 and Γ_8 gives rise to the Z_3 and $Z_{1\,2}$ edge excitons, respectively This spin-orbit splitting in CuCl is reversed with respect to the typical Cu-halide and Ag-halide zincblende semiconductors resulting in the Z_3 exciton appearing at a lower energy than the $Z_{1\ 2}$ exciton This was confirmed by Cardona [81] by examining the energy of the exciton peaks as a function of concentration in the CuBr-CuCl system The energy values and temperature dependence of the exciton energies in CuCl are well documented and a selection of data from different techniques is shown in table 1 1 below for a range of temperatures

Technique	**T(K)**	**Z_3 (eV)**	**$Z_{1,2}$ (eV)**	**Temp Dependence (10^{4} eV/K)**	**Ref**
Luminescence	12	3 204	3 27		[83]
Reflection, Emission	12	3 212	3 283	+2 5 (range 10K to 80K)	[67]
Absorption	80 300	3 237 3 27	3 306 3 34	+1 4 (range 4K to room temp)	[81] [84]
Three-wave mixing	85	3 228		+2 8 (range 30K to 100K)	[85]

Table 1 1 Energy positions and temperature dependence of the Z_3 and $Z_{1\ 2}$ excitons

Thermal shifts of peak energies are mainly caused by the electron-phonon interaction as the thermal expansion of the lattice (volume effect) is negligible in CuCl

The differences in temperature dependence result from the non-linear energy increase with temperature from low temperature to room temperature In fact at ~100K a distinct change in the slope occurs, above this temperature the slope is lower by approximately an order of magnitude Garro *et al* [86] offer an explanation for this based on the difference between the vibrational frequencies of Cu and Cl Cu vibrates predominately at low frequencies (~50cm^{1}), while Cl vibrates mainly at high frequencies (~200cm^{1}) because of its smaller mass The contribution of the Cl vibrations to the dependence of the exciton energy on temperature is opposite to that of the positive Cu contribution, but does not become noticeable until T>100K, hence causing the change in slope It is important to note that the energy separation between the Z_3 and $Z_{1\,2}$ excitons of ~ 0 07eV, remains approximately constant, independent of temperature

1.5 Luminescence and Excitonic Properties of CuCl

Excitonic-based luminescence in CuCl, CuBr and copper halide mixed crystals has been of interest to researchers for the past four decades [81,83, 87,88,89,90] The free exciton binding energies, 190meV for CuCl and 108meV for CuBr [90], are much larger than those of III-V and II-VI semiconductors resulting in a high stability of the exciton even at room temperature An in-depth analysis of the temperature and power dependence of free and bound excitons and biexcitons[d] was performed by these authors Other studies included investigations into the nature of isoelectronic luminescence centres in CuCl, namely bromine and iodine ions [89] It was found that different roles were played by the isoelectronic impurity depending on the ratio of the difference in the electron affinity of the two individual components to the energy width of the exciton band When this ratio is large, two exciton peaks appear, one corresponding to the host exciton and the other to an exciton bound to an impurity When this ratio is small, only one exciton peak appears but it is shifted (depending on impurity concentration) compared to the position of the exciton in pure material

In nanocrystals, electrons, holes, and excitons are confined spatially and their energy levels are quantised It is well known that the confinement of an exciton in a quantum

---

[d] A biexciton (or excitonic molecule) is a complex of two excitons bound by a Coulomb interaction

dot (QD) is classified into two extreme cases which depend on the size of excitons relative to that of the quantum dot. "Exciton confinement" occurs for the case where $a>a_{ex}$ and "electron-hole individual confinement" for $a\leq a_{ex}$, where a is the radius of the QD and a_{ex} is the effective Bohr radius of the bulk exciton [91]. When $a>a_{ex}$, the internal motion of an exciton keeps most of its characteristics as in a bulk crystal. A CuCl QD satisfies the criteria for exciton confinement because the exciton Bohr radius of 0.7nm is much smaller than the radius of the QD [92]. This, along with the very large free exciton binding energy, and the enhancement of non-linear optical properties in nanocrystals compared to bulk materials [93], has prompted many fundamental photoluminescence and spectroscopic studies of CuCl quantum dots embedded in NaCl crystals [94,95,96,97] and glass matrices [98,99].

CuCl is an exceptional compound in which the value of the biexciton binding energy, $E^{b}_{biex} = 32meV$ is much larger than in other semiconductors in which biexcitons have been observed [100], for example in CdS $E^{b}_{biex} = 6.3meV$ [101]and in ZnO $E^{b}_{biex} = 15meV$ [102]. Optical bistability, which is of interest due to its possible device application in integrated optics, has been observed in CuCl due to biexcitons [103,104,105]. Its biexcitonic properties have also prompted investigations of CuCl as a candidate for the observation of Bose-Einstein condensation[e] by generation of a high density of biexcitons in CuCl films via two-photon absorption. It was found that several features of the optical properties of biexcitons in CuCl could be explained by assuming that a Bose-Einstein-condensed state exists at high biexciton densities and at sample temperatures up to 40K [106].

---

[e] The occurrence at sufficiently low temperatures of a phase transition in which all particles exceeding a critical density condense into a single quantum state is known as Bose-Einstein condensation.

Biexcitonic lasing (stimulated emission) in CuCl single crystals at a wavelength ~ 392nm has been reported [107,108] in the 1970's but recently the use of quantum dots to investigate the biexcitonic laser process is more usual [109,110,111]. Kagotani *et al.* [110] confirmed that it was the biexciton state that is excited directly by the pump laser causing the laser emission, by observing that the lasing mode was present with linearly polarized pump light, but disappeared with pumping light that was circularly polarised. However, it will be difficult to generate a high enough density of biexcitons by current injection to be suitable for laser diode applications. At least one group has reported optically pumped violet laser emission from CuCl single crystals without the participation of biexcitons at a wavelength of 391.9nm [112]. In this case the laser transition is thought to occur between the bottleneck of the exciton polariton[f] and the longitudinal optical phonon. This mechanism for the laser emission should also allow pumping by current injection.

1.6 Conductivity of CuCl

Experiments to understand the conductivity mechanisms of CuCl were underway as early as the 1950's. Wagner et *al.* [113] measured the total electrical conductivity and hole conductivity of Cu-halides in the temperature range of 250 to 450°C and concluded that above 300°C the conductivity is dominated by ionic conduction. Later measurements indicated that the hole conductivity, $\sigma = 8.6 \times 10^{-8}$ ohm^{-1}cm^{-1} at 332°C, was about five orders of magnitude lower than the total electrical conductivity in CuCl [114]. Using electrochemical techniques the hole carrier concentration and mobility were determined as 8.8×10^{12} cm^{-3} and 6.1×10^{-2} cm^{2}V^{-1}sec^{-1}, respectively.

---

[f] A polariton is the complex resulting from the polarising interaction between an electromagnetic wave and an oscillator resonant at the same frequency, e.g. the interaction between excitons and photons.

(also at 332°C) In compound semiconductors a deviation from stoichiometry generates donors or acceptors depending on whether it is the cation or the anion which is in excess In PbTe it has been shown that it is not the excess ion but rather the vacancy which determines whether the material is n-type or p-type [115] The aforementioned hole conduction in CuCl is due to the presence of Cu vacancies resulting from excess halogen [113,114] The ionisation of copper vacancies results in holes, represented in Kroger-Vink notation [116] as

$$V_{Cu} \rightarrow V'_{Cu} + h^{\bullet}$$

where, V_{Cu} represents a vacancy on a Cu site, V'_{Cu} is a singly ionised Cu vacancy and $h^{\bullet}$ is a hole Attempts to dope CuCl with Cu_2S [117], Al_2O_3 [118] and CsCl [119] all resulted in an increase in conductivity (up to two orders of magnitude greater in the case of Al_2O_3) However, this was attributed to an increase in the ionic conduction and not an electronic doping effect

Knauth *et al* [120] have performed Hall effect measurements demonstrating p-type semiconductivity of CuBr due to metal deficiency, but found that the measured acceptor concentration $\sim 9 \times 10^{17}\ \mathrm{cm}^{3}$ was enhanced by incorporation of oxygen at the surface and was not exclusively due to holes resulting from Cu vacancies Oxygen introduces acceptor levels in CuBr by filling Br sites in the lattice according to

$$\frac{1}{2}O_2(g) + V_{Br} \rightarrow O'_{Br} + 2h^{\bullet}$$

Hence, oxygen doping enhances the density of holes in Cu-halides It is expected that the oxygen was mainly near the surface as the oxygen bulk diffusion is very slow at room temperature

In related experiments the I-V characteristics of gold and copper electrodes on CuBr were investigated [121,122,123] It was found that Au acted as an ion blocking electrode resulting in non-linear I-V characteristics, while ohmic contacts were achieved with Cu electrodes The ability to suppress the ionic current using Au contacts enabled a measurement of purely electronic hole conductivity, σ~ 10^{5} ohm^{1}cm^{1} for CuBr thin films deposited on glass substrates With thin films deposited on Cu substrates, the same experiments resulted in electronic conductivities three orders of magnitude lower [121] This was explained by a reduction in the non-stoichiometry of the CuBr film due to equilibration with the Cu substrate,

$$Cu_{(s)} + V'_{Cu} + h^{\bullet} \rightarrow Cu_{Cu}$$

Hence there are fewer holes in the valence band available for conduction and the electronic conductivity is reduced

1 7 Objectives of this Project

γ-CuCl on Si - the growth of a wide-bandgap, direct bandgap, optoelectronics material on silicon substrates is a completely novel material system, with compatibility to current Si based electronic/optoelectronics technologies The potential of this exciting new area in wide-bandgap semiconductor growth - “blue” optoelectronics on Si wafers - is investigated

The aims of this project include an early evaluation of the feasibility of growing γ-CuCl on Si by means of a simple vapour deposition growth technique on a suitably prepared Si substrate Analysis of the structural, optical and electrical properties of the grown thin film will be used to assess the quality of the films The ultimate goal is to fabricate and test a simple metal-pn junction-metal blue-light emitting diode structure using a Si substrate with doped CuCl epilayers

Structural, optical and electrical characterisation of this new optoelectronics material system was performed by techniques such as x-ray diffraction (XRD), micro-Raman spectroscopy, UV-visible spectroscopy (UV-VIS), cathodoluminescence (CL), photoluminescence (PL), resistivity and Hall effect measurements

XRD was used to examine the crystallinity of γ-CuCl thin films on nearly lattice matched Si substrates as a function of growth parameters such as rate, thickness, substrate orientation and thermal treatments

Investigations of the optical properties of the CuCl thin films were performed by UV-VIS, PL and CL The UV excitonic emission was studied at room temperature using UV-VIS and CL and a temperature dependent study was performed with PL

Electrical characterisation included resistivity measurements, current-voltage response of metal contacts and determination of the carrier type using the rectifying probe technique and Hall effect measurements

Working towards the ultimate goal of a light emission across a pn junction, the possibility of doping CuCl was investigated A simple electroluminescent device structure was developed and tested This opens up the possibilities for UV optoelectronics on lattice-matched silicon substrates

1 8 Overview of this Report

In chapter one the rationale behind the project has been discussed An introduction to the properties of CuCl is given and the main areas of research performed previously on CuCl are described The fundamental aims of this research have been outlined

In chapter two the experimental techniques and instruments used for the growth and analysis of CuCl on Si are described

The main experimental results obtained are presented and discussed in three sections The structural, optical and electrical characterisation of CuCl is discussed in chapters three, four and five, respectively

Conclusions are given in chapter six and the areas of most importance for future work are highlighted

In order to obtain a more rounded view of advanced semiconductor technologies, work was performed throughout this PhD on a variety of semiconductor materials A study on Si-SiGe heterostructures and Ge quantum dots on Si, using synchrotron x-ray topography and micro-Raman spectroscopy is presented in appendices A and B, respectively

Chapter 2

Characterisation Techniques

2.1 Sample Preparation

A silicon sample with (100) or (111) surface orientation, approximately 2cm x 1 5cm in size is cleaved from a 4 inch silicon wafer The wafers are single-side polished, p-type, boron-doped silicon, with a resistivity in the range of 0 – 20 Ωcm The samples were cleaned first by scrubbing with Decon™ solution, then dipping in trichloroethylene, acetone and methanol, each for 5-10 minutes to degrease the substrate The solvents were removed by dipping in deionised water for 5 minutes The native silicon oxide was etched by dipping in a Hydrofluoric acid solution of five parts 48% HF and one part de-ionised water for one minute The sample is then rinsed in deionised water, blown dry using a Nitrogen gun and immediately loaded into the vacuum chamber of an Edwards Evaporator system

The vacuum system used in this work was an Auto 306 Edwards evaporation system, which operates as a thermal resistance evaporator The Auto 306 is an automated system with a base pressure of 1 x 10^{6} mbar and evaporation pressure of ~ 3 0 x 10^{6} mbar An FTM6 thickness monitor, used in conjunction with a water-cooled crystal holder is built into the Auto 306 evaporation system It is designed to measure and display the thickness of films deposited in vacuum coating systems A schematic diagram of the evaporator system is shown in fig 2 1

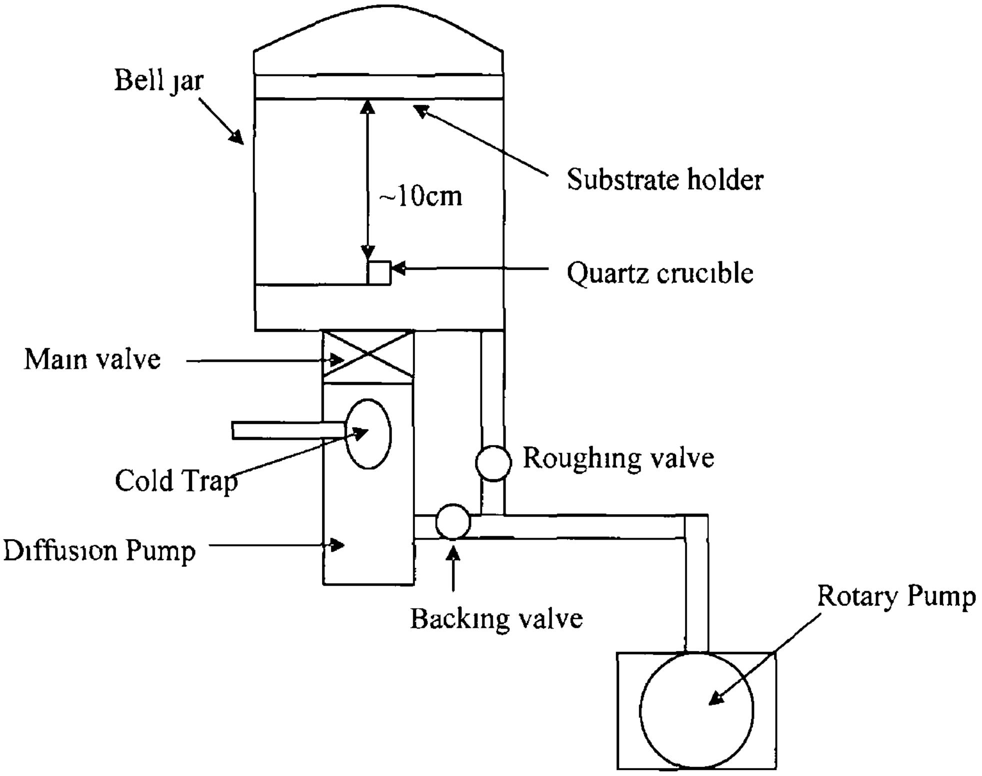

Fig 2 2 Schematic diagram of an Edwards Evaporator System

The rotary pump is used to remove 99% of the air from the chamber, reducing the pressure to the correct operating range for the oil diffusion pump - approximately 0 2 mbar as measured by the Pirani gauge At this backing pressure the diffusion pump begins to function The diffusion pump is cooled by the continuous flow of water around the diffusion chamber The working fluid is an organic silicone compound from Dow Corning, having a vapour pressure at cooling water temperature in the range 10^{3} – 10^{-4} mbar, and boiling under a backing pressure of ~ 0 2 mbar in the temperature range 150 – 250°C The basic principle under which the diffusion pump operates is that the silicone fluid boils under reduced pressure and is formed into a vapour jet into which the gas molecules to be pumped diffuse, and are carried by the vapour jet towards the rotary pump, where they are expelled to the atmosphere, reducing the chamber pressure [124] The pump fluid must be removed and returned to the boiler after it has performed a cycle, hence the water cooling of the pump casing Liquid nitrogen is added to the cold trap before deposition to ensure that the diffusion pump is working most efficiently during evaporation and minimising the passage of fluid from the pump to the evaporation chamber

The system is ready for evaporation when the pressure reaches ~ 10^{6} mbar, as measured by the Penning gauge Commercially supplied CuCl powders with purities of either 97% (Merck) or 99 999% (Alfa Aesar), respectively, were heated by resistive heating of a quartz crucible The CuCl powder was evaporated and deposited onto the substrate positioned approximately 10cm above the crucible This process is known as thermal evaporation and is a physical vapour deposition (PVD) technique The angular distance between the crucible and substrate was also noted as slight variations in the deposit thickness were evident depending on the position of the substrate Adjusting the current flowing through the crucible controls the rate of evaporation, which was estimated by monitoring the resonant frequency of a crystal oscillator using either the FTM6 thickness monitor This frequency changes as the film thickness of the deposit on the crystal changes Film thickness is calculated from the measured crystal resonant frequency and the default or specified deposition material density and tooling factors, as follows,

$$T_c = \frac{F\, D_q\, N_q\, (P_q - P_6)}{D_e} \qquad (2\ 1)$$

where T_c is the calculated film thickness, F is the tooling factor, D_q is the density of quartz, N_q is the frequency constant of quartz, P_q is the period of a loaded crystal (period = 1/frequency), D_e is the density of the deposition material and P_6 is the period of a 6 MHz crystal used in the thickness monitor The density of the film material is calculated as follows,

$$D_e = D_a \frac{T_i}{T_m} \qquad (2\ 2)$$

where D_a is the actual density of the bulk material, which is 4 14gcm^{1} for CuCl [**48**], T_i is the thickness measured by the thickness monitor and T_m is the average actual thickness The tooling factor, *F*, is the average actual thickness divided by the thickness measured by the thickness monitor,

$$F = \frac{T_m}{T_i} \qquad (2\ 3)$$

The tooling factor is used to compensate for differences between the source-to-substrate and source-to-crystal distance If the crystal is further from the source than the substrate, the crystal will receive a thinner deposit than the substrate A tooling factor of 1 0 implies that the crystal and substrate receive the same deposit thickness In this case, a tooling factor of 3 13 was calculated for use with CuCl, implying that the crystal receives a thinner deposit than the substrate Evaporation rates used range from 2Å/sec to 150Å/sec An evaporation rate of ~ 5Å/sec was found to be optimum for sample quality and reproducibility Faster evaporation rates result in particles on the surface of the film Slower evaporation rates were non-uniform, did not yield any advantage in terms of crystallinity and were more time consuming CuCl thickness is typically around 500nm After deposition, samples are annealed in a home built graphite strip annealer in the temperature range of 50°C to 430°C in forming gas, (95% nitrogen, 5% Hydrogen), nitrogen or argon

2.2 X-Ray Diffraction (XRD)

In order to examine the fine details of molecular or crystalline structure with lattice dimensions 10^{8} to 10^{-10} m, it is necessary to use radiation of a wavelength comparable to, or smaller than the dimensions of atoms X-rays, having wavelengths in this region, are therefore a useful radiation source for such studies X-rays are produced by bombarding a target composed of an element of intermediate atomic number, (e g Cr, Mo, Cu) with fast electrons [125] A Bruker Advanced X-Ray Solutions D8 X-Ray Diffractometer with a Cu target is used for our studies of the structural properties of CuCl thin films on Si and glass substrates The Cu target (anode) is held at a potential difference of 40keV with respect to the W filament source of electrons (cathode) and a filament current of 40mA results in the emission of x-rays at wavelengths of 1 5406 Å and 1 5444 Å characteristic of $CuK_{\alpha1}$ and $CuK_{\alpha2}$ x-rays, respectively In general a Ni filter is used to minimise diffraction from CuK_{β} x-rays However, occasionally a weak diffraction peak resulting from CuK_{β} x-rays with a wavelength of 1 3959 Å appears in the spectrum Characteristic Cu $K_{\alpha2}$ reflections can be removed from the diffraction pattern using software provided by the manufacturer

In 1913 W L Bragg showed that the diffracted beams behaved as if they were reflected from planes passing through points of the crystal lattice Waves scattered from adjacent lattice planes will be just in phase (i e the difference in the paths travelled by these waves will be an integral multiple of the wavelength, nλ) only for certain angles of scattering This is illustrated in fig 2 2 below

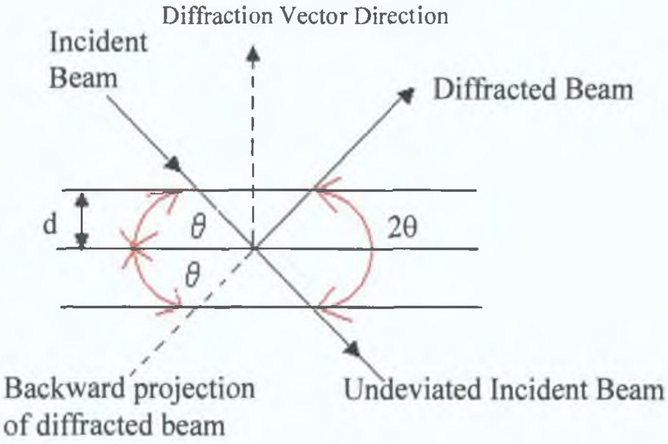

Fig. 2.2 Schematic diagram of Bragg diffraction

From this Bragg derived his famous equation [125],

$$2d\sin\theta = n\lambda \quad (2.4)$$

where d is the distance between lattice planes in a crystal and θ is the angle of incidence of the x-ray beam with respect to the diffracting planes. Since it appears as if reflection has occurred from these lattice planes with the direct beam deviated by the angle 2θ from its original direction, diffraction beams are often referred to as reflections.

The most basic set up of the x-ray diffractometer is the Bragg-Brentano geometry as shown in fig. 2.3. The sample rotates at a constant angular velocity such that the angle of incidence of the primary beam changes whilst the detector rotates at double angular velocity around the sample. The diffraction angle 2θ is thus always equal to twice the incident angle, θ. The focus, sample and detector slit are on the focussing circle; the focus and detector slit are also located on the measuring circle. The radiation emanating from the line focus of the x-ray tube is diffracted at the sample and recorded by the detector. Each time the Bragg condition is satisfied the primary beam is reflected from the sample to the detector. The detector and the connected measuring electronics measure the intensity of the reflected radiation; the angular position of the reflections is displayed at the controller. Pulse counts of diffraction patterns are obtained in this way.

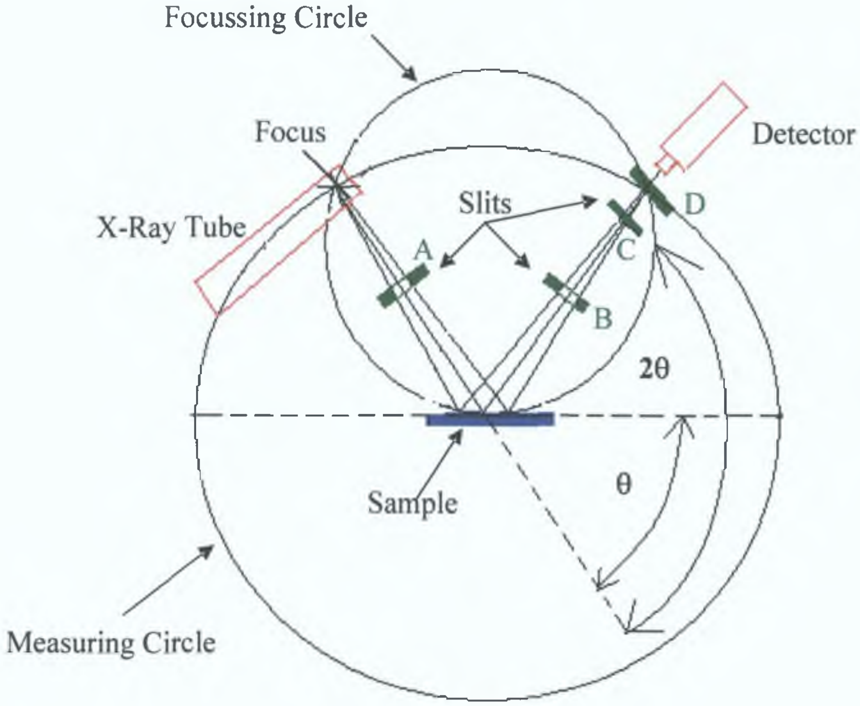

Fig. 2.3 Set –Up of D8 Advance X-Ray Diffractometer in Bragg Brentano Geometry [126].

A: aperture slit, B: scattered radiation slit, C: Kβ filter, D: detector slit.

A system of slits is used as labelled in fig. 2.3. The aperture slit, A, delimits the irradiated sample area. The scattered radiation slit, B, suppresses undesired scattered radiation. The Kβ Ni filter, C, reduces the intensity of the characteristic Cu Kβ reflections and the detector slit, D, aligns X-rays into the detector.

When glancing angle (GAXRD) geometry is used, the X-ray beam falls on the sample at a fixed low angle of incidence thus limiting the penetration of the x-rays into the sample. Therefore it is possible to get information from upper surface regions of the film. However this technique is only applicable to polycrystalline samples in which the crystallites are randomly oriented. For single crystals, the Bragg condition cannot be satisfied unless the angle of the incident x-rays is equal to θ.

Other possible diffraction geometries including rocking curves, 2θ – omega (ω) and phi (ϕ) scans are also used to examine the growth of CuCl on (100) and (111) Si substrates.

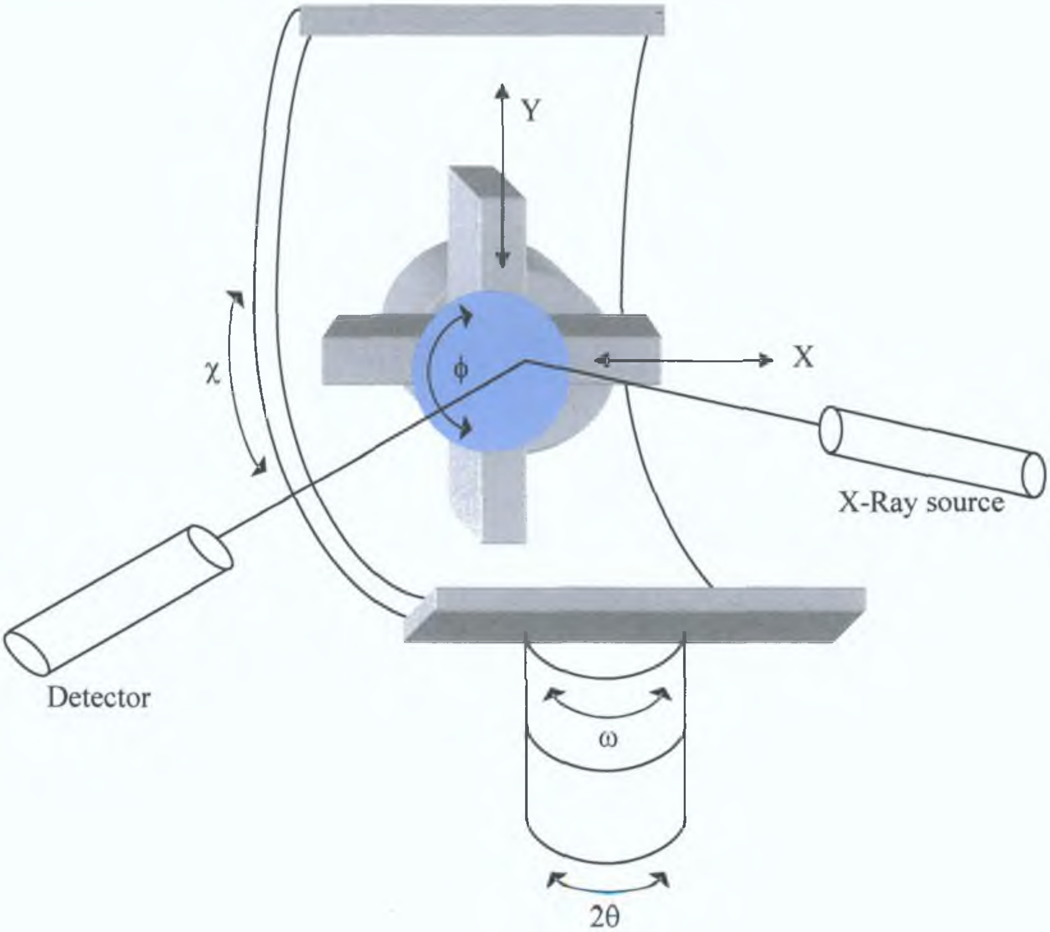

Fig. 2.4 Illustration of the x-ray diffractometer, goniometer [127]

When performing a rocking curve the 2θ value is set to a known Bragg angle of the sample (i e the detector is fixed) and the crystal is then tilted (rocked) within the diffraction plane over a small angular range while a scan is performed over the specified θ values The resulting θ vs intensity curve is known as a rocking curve The width of the rocking curve is an indication of the range of orientation present in the irradiated area of the crystal, as each sub grain of the crystal will come into orientation as the crystal is rotated The FWHM of a rocking curve of the epilayer peak is a measurement of the quality of the layer It is compared to the width of a high quality single crystal (e g Si) which gives an indication of the instrument broadening which is a function of the slits and step size used

Having performed a rocking curve on a single Bragg peak, the detected offset between the θ and 2θ angles due to the tilt of the lattice planes found from the rocking curve peak position can be used when scanning over the full 2θ range with a 2θ-ω scan This differs from the Bragg-Brentano geometry in which the sample and detector move together as a locked couple at fixed θ-2θ angles

An in-plane sample rotation is performed by a ϕ scan A fixed Bragg angle is selected and the sample is rotated by up to 360° Depending on the symmetry of the crystal, diffraction peaks will be detected at fixed intervals as the sample rotates Therefore this geometry is often used to confirm epitaxial growth [45,128]

2.3 Micro-Raman Spectroscopy

An Indian physicist named C V Raman first reported the Raman effect in the 1920's [129] It is based on the inelastic scattering of monochromatic radiation When a photon interacts with a molecule, the vast majority of the light is scattered elastically However a small percentage of the light undergoes an energy exchange with the molecule such that the scattered photon is of higher or lower energy than the incident photon, (see fig 2 5) The difference in energy is made up of a change in the rotational and vibrational energy of the molecule by absorbing or emitting a phonon and gives information on its energy levels

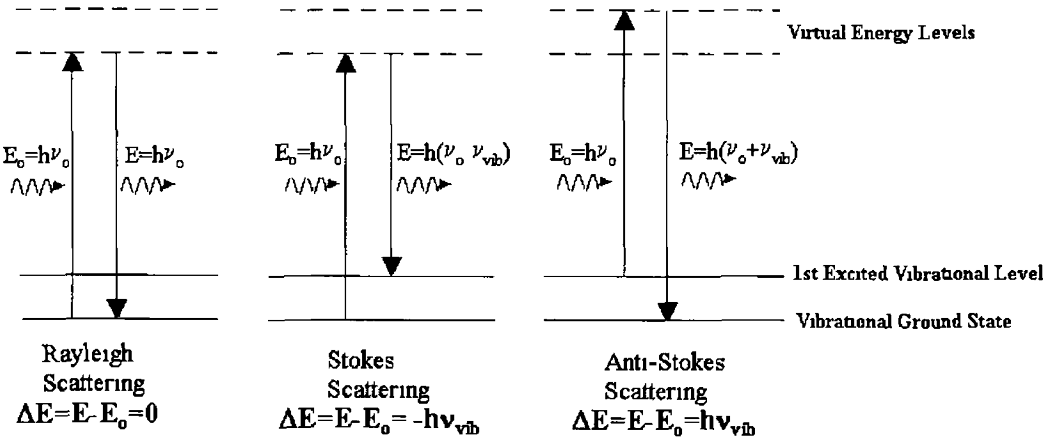

Fig 2 5 Schematics of Rayleigh, Stokes and Anti-Stokes scattering

High intensity Rayleigh scattering occurs when an atom is excited by a photon, $E_0=hv_0$ to a virtual energy level The atom can be returned to the ground state by emitting a photon of the same energy, $E=hv_0$ If instead, the atom is returned to an excited vibrational level, the energy difference is emitted as a photon of lower energy, $E=h\ (v_0-v_{vib})$ This results in the emission of light of a longer wavelength and is known as Stokes Scattering If an atom is situated for example on the first excited vibrational level and absorbs a photon of energy, $E_o = h\nu_o$, it gets excited to a virtual energy level, which is higher in energy than the case for Rayleigh or Stokes scattering When the atom relaxes it is returned to the vibrational ground state by emitting a photon of energy, $E = h\,(\nu_o + \nu_{vib})$ This light is of shorter wavelength and is called Anti-Stokes Scattering [130] Conservation of energy and momentum requires that the energy gained by absorbing a phonon (anti-Stokes shifted), or energy lost by emitting a phonon (Stokes shifted), is balanced by the phonon frequency and wave vector of the vibration

$$h\omega_s = h\omega_i \pm h\omega_j \qquad (2\ 5)$$

$$\mathbf{K}_s = \mathbf{K}_i \pm \mathbf{q}_j \qquad (2\ 6)$$

where $h\omega_s$ and $h\omega_i$ are the scattered and incident photon energies respectively and $h\omega_j$ is the energy of the phonon vibration, $\mathbf{K}_s$ and $\mathbf{K}_i$ are the wave vectors of the scattered and incident photons respectively, and $\mathbf{q}_j$ is the wave vector for the phonon vibration [131] The Maxwell-Boltzmann distribution law states that the population ratio of the v=1 and v=0 vibrational levels is given by

$$\frac{P_{v=1}}{P_{v=0}} = e^{-\Delta E / kT} \qquad (2\ 7)$$

where ΔE is the energy difference between the two states, k is Boltzmann's constant and T is the absolute temperature [132] In accordance with this law the population of molecules at v=0 is in general much greater than that at v=1, thus the Stokes lines are stronger than the anti-Stokes lines

Not all molecular vibrations are Raman active, therefore infrared (IR) spectroscopic data is usually also taken in conjunction with Raman data A vibration is IR active if the dipole moment is changed during the vibration and Raman active if the polarizability is changed during a vibration According to classical theory, Raman scattering can be explained as follows [132], the electric field strength, E, of an electromagnetic wave (in this case the laser beam) fluctuates with time, t, given by

$$E = E_0 \cos 2\pi \nu_0 t \qquad (2\ 8)$$

where E_0 is the vibrational amplitude and ν_0 is the frequency of the laser light If this light irradiates a diatomic molecule, an electric dipole moment P is induced

$$P = \alpha E = \alpha E_0 \cos 2\pi \nu_0 t \qquad (2\ 9)$$

α is a proportionality constant called the polarizability If the molecule is vibrating with a frequency ν_m, the nuclear displacement q is written

$$q = q_0 \cos 2\pi \nu_m t \qquad (2\ 10)$$

where q_0 is the vibrational amplitude of the molecule For small amplitudes of vibration, α is a linear function of q Therefore

$$\alpha = \alpha_0 + \left(\frac{\partial \alpha}{\partial q}\right)_0 q + \quad , \qquad (2\ 11)$$

where α_0 is the polarizability at the equilibrium position, and $(\partial\alpha/\partial q)_0$ is the rate of change of α with respect to the change in q, evaluated at the equilibrium position Combining the above equations to first order

$$P = \alpha E_0 \cos 2\pi \nu_0 t$$

$$P = \alpha_0 E_0 \cos 2\pi \nu_0 t + \left(\frac{\partial \alpha}{\partial q}\right)_0 q E_0 \cos 2\pi \nu_0 t$$

$$P = \alpha_0 E_0 \cos 2\pi \nu_0 t + \left(\frac{\partial \alpha}{\partial q}\right)_0 q_0 E_0 \cos 2\pi \nu_0 t \cos 2\pi \nu_m t \qquad (2\ 12)$$

$$2 \cos A \cos B = \cos(A+B) + \cos(A-B)$$

$$\Rightarrow P = \alpha_0 E_0 \cos 2\pi \nu_0 t + \frac{1}{2}\left(\frac{\partial \alpha}{\partial q}\right)_0 q_0 E_0 [\cos\{2\pi(\nu_0 + \nu_m)t\} + \cos\{2\pi(\nu_0 - \nu_m)t\}]$$

The first term represents an oscillating dipole that radiates light of frequency ν_0, i e Rayleigh scattering, while the second term corresponds to the Raman scattering of frequency ($\nu_0 + \nu_m$) and ($\nu_0 - \nu_m$), anti-Stokes and Stokes scattering respectively It is clear that if $(\partial \alpha / \partial q)_0$ is zero, the second term equals zero and the vibration is not Raman active This confirms what was already stated above to be Raman-active, the rate of change of polarizability α with the vibration must not be zero

In this work the micro-Raman spectroscopy measurements were performed by a Jobin Yvon LabRam HR800 μRS system in backscattering geometry using both a 488 nm Ar^+ laser and a 325 nm HeCd UV laser excitation at room temperature A 100× (or 40× for the UV laser) objective was used to focus the laser source to a diameter of about 1 μm on the sample surface The Raman signal from the sample was collected by the same objective and detected by a liquid nitrogen cooled charge coupled device (CCD) detector A confocal hole of 100 μm and a grating of 1800 g/mm were chosen during the experiments Before measurement the equipment was calibrated carefully with a strain free Si Raman peak position Each spectrum was obtained with 3 accumulation times to surpass noise effects

The distance between two points of the same phase in successive waves of electromagnetic radiation is called the wavelength, λ The frequency, ν, is the number of waves contained in the distance light travels in one second $\nu = \frac{c}{\lambda}$, where c is the velocity of light A related parameter, which is most commonly used in vibrational spectroscopy, is the wavenumber $\tilde{\nu}$, defined by $\tilde{\nu} = \frac{\nu}{c}$ The units of $\tilde{\nu}$ are therefore cm^{-1} which defines the number of waves of electromagnetic radiation of wavelength λ, which exist in a unit length, in this case 1 cm Measuring the energy of the photons emitted during Stokes or anti-Stokes scattering as already described creates the Raman spectrum The energy is related to the wavenumber by

$$E = h\nu = h\frac{c}{\lambda} = hc\tilde{\nu} \qquad (2.13)$$

Vibrational transitions which are observed in infrared (IR) or Raman spectra appear in the 10^2 cm^{-1}-10^4 cm^{-1} region of the electromagnetic spectrum Lasers of different wavelengths can be used to excite the samples In order that vibrational modes are always recorded at the same spectral position, the frequency of the modes are always measured relative to the frequency of the laser light and the units are most correctly denoted relative cm^{-1} (Rcm^{-1}) However, Raman spectra are commonly labelled by simply cm^{-1} In our system, the Raman peak positions were found to an accuracy of 0.04 cm^{-1} by fitting the original experimental spectrum with a Gauss/Lorentz function using the software provided by the equipment manufacturer During the visible laser micro-Raman measurement, the laser plasma line position was used as an internal reference to ensure the measurement accuracy [133]

The intensity of the laser light decreases as it passes through the sample due to absorption of the light by the material The total scattered light intensity, I_s, integrated from the surface of the sample to a depth d, is given by [134]

$$I_s = I_0 D \int_0^d e^{-2\alpha x} dx = \frac{I_0 D}{2\alpha}\left(1 - e^{-2\alpha d}\right) \qquad (2\ 14)$$

where I_0, D and α are the incident light intensity, the Raman scattering cross section and the absorption coefficient of the probed material at the wavelength of the laser source, respectively The total scattered light intensity integrated from the depth d to infinity, I_d, is given by

$$I_d = I_0 D \int_d^\infty e^{-2\alpha x} dx = \frac{I_0 D}{2\alpha} e^{-2\alpha d} \qquad (2\ 15)$$

It is often assumed [133,135] that the penetration depth d_p is given by the depth that satisfies the relationship

$$\frac{I_d}{I_s + I_d} = 0\ 1 \qquad (2\ 16)$$

Therefore, the penetration depth is given by

$$d_p = \frac{-\ln 0\ 1}{2\alpha} = \frac{2\ 3}{2\alpha} \qquad (2\ 17)$$

The absorption coefficients for some common materials can be found in references [135,136]

2.4 X-ray Microanalysis

When an electron beam interacts with matter, the following products may occur as shown in fig 2 6 backscattered electrons, secondary electrons, x-rays, cathodoluminescence and Auger electrons. Backscattered and secondary electrons are used for imaging in the scanning electron microscope (SEM). Auger electrons occur when the energy emitted by an electron transition is absorbed by another electron, which is raised to a higher-energy state in the conduction band. This energy is then dissipated by emission of phonons. Auger effects are not examined in this work.

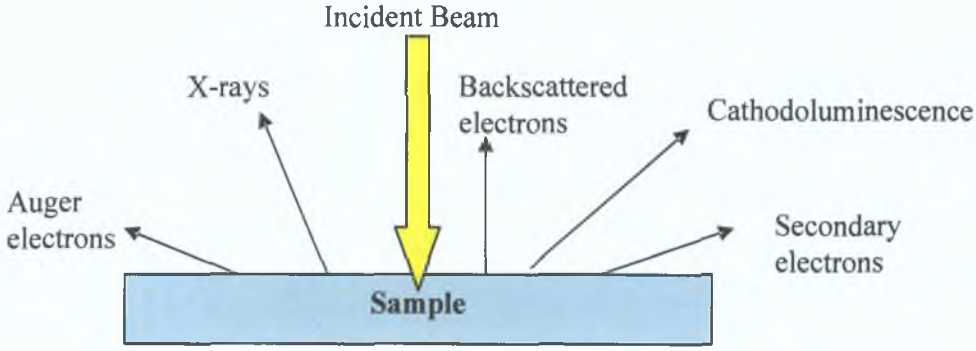

Fig. 2.6 Signals produced when an electron beam is incident on a sample

Whenever an electron beam interacts with a material, x-rays characteristic of the material are produced. According to the Bohr model of the atom, electrons are arranged in distinct energy bands or shells. The principal quantum number, n, is used to label a shell in which all the electrons have approximately the same energy. The n=1 shell is the energy level closest to the nucleus. In the standard nomenclature used in x-ray spectroscopy the n=1, n=2, n=3 shells are referred to as the K, L, M shells, etc [137]. The electrons in the K shell are therefore closest to the nucleus and require the most energy to remove them from the atom (i.e. they have the highest ionisation energy).

An electron beam incident on a material can interact with the electrons of the material's atoms, causing the ejection of the electron from its shell in the atom The resulting atom is then in an excited state and there are several ways in which it can relax to the ground state depending on the shell from which the electron has been ejected from For example if a vacancy has been created in the K shell, an M shell electron can fall down to fill the K shell vacancy, or an L shell electron can fill the vacancy in the K shell and the resulting vacancy created in the L shell can be filled by an M shell electron The rearrangement of electrons results in the emission of quanta of energy in the form of x-rays, which returns the atom to its lowest energy state

K, L, and M shells have distinct energies for each atomic number, Z Therefore whenever an electron transitions occurs in an atom, the energy of the x-ray quantum created can be related back to the element of origin The relationship of x-ray energy to the element of origin is given by Moseley's law [138],

$$E^{1/2} = C_1 (Z-C_2) \qquad (2\ 18)$$

where C_1 and C_2 are different constants for each series Thus for lighter atoms populated only up to the L shell only one transition is possible and the resulting spectrum will consist of a single peak at one energy value For heavier elements, many shells are populated and many different re-arrangements of energy are possible to return the atom to the ground state Therefore the spectrum of heavier elements will contain several lines There is an accepted nomenclature for the naming of the various lines that may appear in an x-ray spectrum X-rays produced from electrons falling to the K shell are referred to as K lines and x-rays produced from electrons falling to the L shell are called L lines If the electron falling into the K shell comes from the L shell the L line is called K_α; if the electron falling into the K shell comes from the M shell the line is called the K_β line (see fig.2.7).

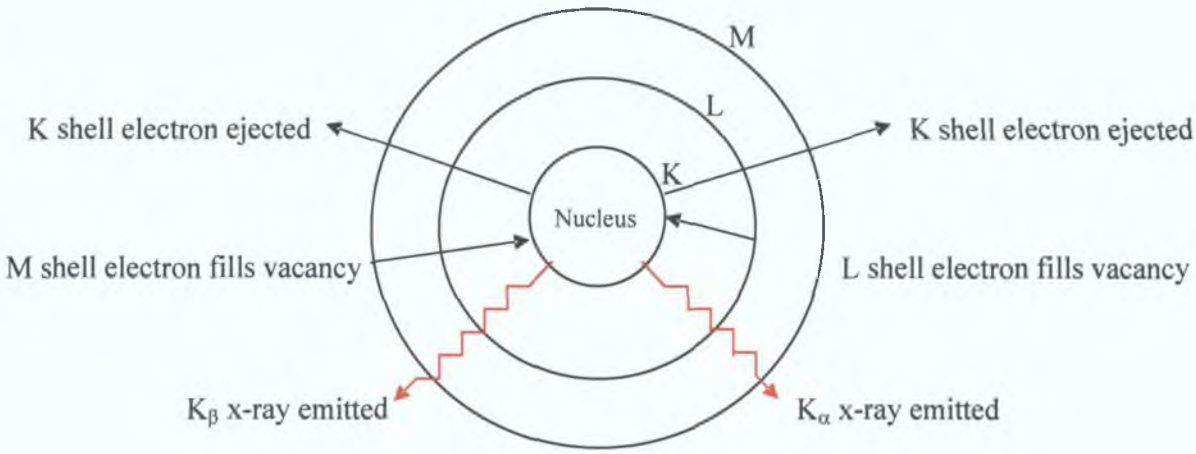

Fig. 2.7 Schematic diagram showing naming scheme of emitted x-rays

The nomenclature scheme does not strictly follow a predictable pattern as already illustrated but all possible transitions in all the elements of the periodic table have been identified and the families of lines named [138].

When an electron beam hits a sample, the x-rays produced have energies characteristic of the atom emitting them. The x-ray monitoring is carried out with energy dispersive spectrometers. Thus different elements present in the material can be catalogued according to the energy of the x-rays they emit. This gives an elemental microanalysis of the sample. The composition of CuCl thin films on Si was investigated using a LEO Stereoscan 440 scanning electron microscope and Princeton Gamma Tech energy dispersive x-ray (EDX) analyser with a silicon (Li) detector. The Li window which covers the Si detector will absorb low energy x-rays, therefore light elements such as hydrogen cannot be detected using this technique An accelerating voltage of 15keV and probe current of 800pA was found to be suitable for a qualitative comparison of the CuCl composition as a function of time and heat treatment

2.5 Luminescence

Luminescence is the general term to describe the emission of electromagnetic radiation from a solid when it is supplied with some form of energy The interaction of light with semiconductors is an important and powerful means of their characterisation It is non-contacting and non-destructive In semiconductors light is emitted as the result of electronic transitions between quantum mechanical states separated by energy levels of less than 1eV to about 4eV Energy and momentum must be conserved during the electronic transitions When the maximum of the valence band and the minimum of the conduction band occur at the same value of the wave vector **k**, transitions are direct (fig 2 8 (a)), and the material is known as a direct gap semiconductor, for example GaN, GaAs and CuCl

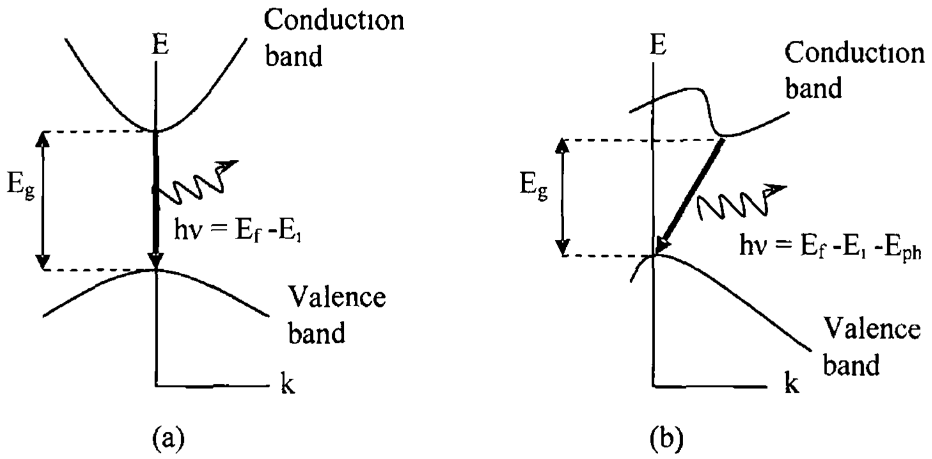

Fig 2 8 Energy transitions in (a) direct and (b) indirect gap semiconductors between initial states E_i and final states E_f For indirect transitions (b) the participation of a phonon, E_{ph}, is required [139]

If the band extrema do not occur at the same wave vector **k**, transitions are indirect and energy-momentum conservation requires that a phonon be emitted to complete the transition as shown in fig 2 8 (b)

When an electron is promoted from the valence band into the conduction band, the electron and hole become free A free hole and a free electron as a pair of opposite charges experience a Coulombic attraction and hence the electron can orbit about the hole as if this were a hydrogen-like atom [140] This excited state is referred to as a free exciton The Coulombic interaction between the electron-hole pair, modified by the dielectric constant of the semiconductor, brings their energy levels closer together than the width of the band gap An exciton can move through the crystal, but because it is a bound electron-hole pair, both electron and hole move together so it does not contribute to the conductivity of the semiconductor In general excitonic levels are only observable at low-temperatures at which *k*T is smaller than the excitonic binding energy where *k* is Boltzmann's constant However in a few wide-bandgap materials such as ZnO and CuCl, a very strong exciton binding energy (~190meV for CuCl [90]) means that excitonic transitions are observed even at room temperature, where kT ~ 26meV Fig 2 9 below illustrates some of the common radiative transitions which can occur in a semiconductor resulting in light emission [139]

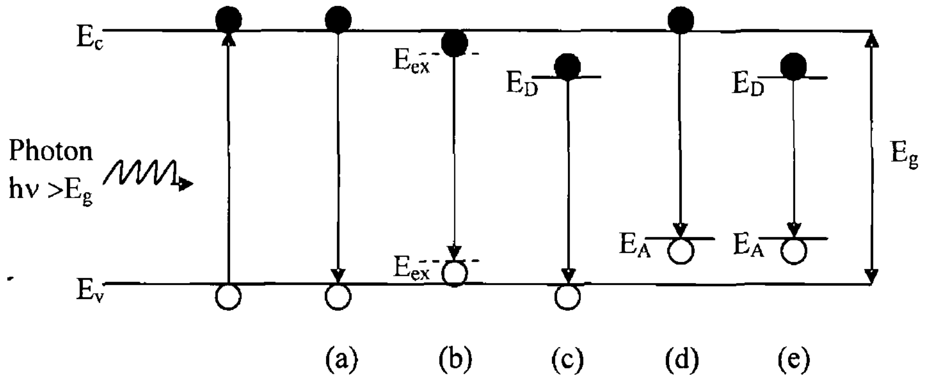

Fig 2 9 Schematic diagram of radiative transitions between the conduction band (E_c), the valence band (E_v) and exciton (E_{ex}), donor (E_D) and acceptor (E_A) energy levels in a semiconductor

For the example given in fig 2 9, the sample is excited with an optical source such as a laser, with energy hv >E_g, generating electron-hole pairs which recombine by one of several mechanisms Process (a) is an interband transition resulting from the recombination of electrons in the conduction band to holes in the valence band

Band-to-band recombination dominates at room temperature in typical semiconductors If the material is sufficiently pure, free excitons form and recombine by emitting photons as shown in process (b) of fig 2 9 In a direct band-gap semiconductor, the energy of the photon emitted when the exciton collapses radiatively is [141]

$$h\nu = E_g - E_x \qquad (2\ 19)$$

where E_x is the excitonic binding energy Transitions which start or finish on localised impurity states, e g donors just below the conduction band, or acceptors just above the valence band are illustrated in fig 2 9 (c) and (d) A free hole can couple with a neutral donor to form a positively charged excitonic ion known as a bound exciton The electron bound to the donor travels in a wide orbit about the donor as shown in fig 2 10 below

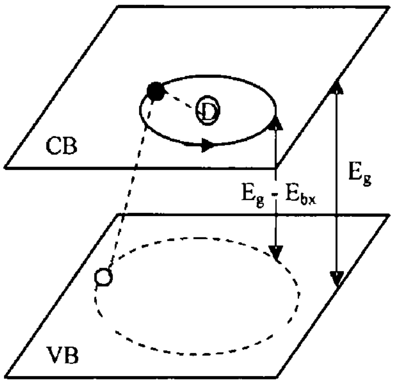

Fig 2 10 Illustration of an exciton bound to donor, D [140] E_{bx} is the binding energy of a bound exciton

The associated hole, then also travels about this donor by moving in the electrostatic field of the "fixed" dipole, determined by the instantaneous position of the electron [140] Similarly an electron can couple with a neutral acceptor also forming a bound exciton In the presence of impurities, free and bound excitons can occur simultaneously in the same material The emission of the bound exciton is characterised by a narrow spectral width at a lower photon energy than that of the free exciton, therefore it is possible to distinguish between them In fig 2 9 (e) a donor-acceptor (D-A) recombination process is shown, where an electron on a neutral donor recombines with a hole on a neutral acceptor The emission has an energy modified by the Coulombic interaction between donors and acceptors [141],

$$h\nu = E_g - \left(E_A + E_D\right) + \frac{q^2}{\varepsilon_s \varepsilon_0 r} \qquad (2\ 20)$$

where q is the magnitude of the electronic charge, ε_s is the dielectric constant of the semiconductor, ε_0 is the permittivity in vacuum and r is the distance between the donor and acceptor

Two free holes and two free electrons can couple to form an excitonic complex known as a biexciton A schematic diagram is shown in fig 2 11

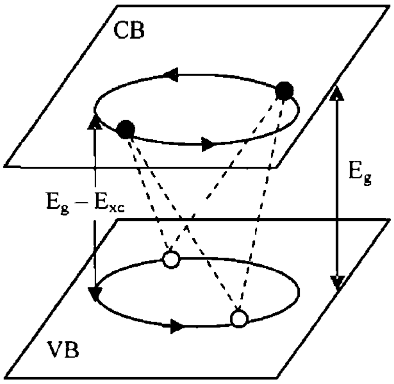

Fig 2 11 Excitonic complex (biexciton) consisting of two electrons associated with two holes [140] E_{xc} is the binding energy of the excitonic complex

The biexciton has a lower energy than two free excitons, since each carrier sees the coulombic attraction of two opposite charges Similar to the free exciton, Coulomb forces from donor or acceptor impurities attract free biexcitons to form bound biexcitons

2.6 Photoluminescence

Photoluminescence (PL) is the term used to describe the emission of light by a material illuminated by photons For semiconductors it is customary to use photons with energy greater than the band gap and this results in high densities of free electron-hole pairs whose recombination results in luminescence, albeit with less than 100% efficiency in most cases The recombination pathway for the electron-hole pairs is strongly influenced by the nature and degree of imperfection in the material, and this provides a powerful means of studying such imperfections as well as the intrinsic properties of the semiconductor itself As a result, PL is one of the most widely used techniques in semiconductor characterization Low temperature measurements are necessary to obtain the fullest spectroscopic information by minimising thermally activated non-radiative recombination processes and thermal line broadening The thermal distribution of carriers excited into a band contributes a width of approximately $kT/2$ to an emission line originating from that band This makes it necessary to cool the sample to reduce the width [141]

In this work, a UV Ar ion Innova laser with a second harmonic generation beta barium borate (BBO) crystal producing a 244nm line (E ~ 5 1eV) was used to excite photoluminescence, which was captured with a TRIAX 190 Jobin Yvon-Horiba spectrometer (resolution 0 3 nm) with liquid nitrogen cooled CCD detector The maximum excitation power was ~ 10W/cm^2 Temperature dependent measurements were performed from room temperature to 10K

2.7 Cathodoluminescence

Electron beam excitation can also be used to generate luminescence Cathodoluminescence (CL) is the name given to visible or near-visible radiation produced by a specimen under the irradiation of an electron beam [142] Light emission from a sample excited by an electron beam gives a good indication of whether it will be possible for light to be emitted by injection of an electron current and is therefore a good early indicator of the possibility of producing a light emitting device As it does not require an ohmic contact or Schottky barrier to operate, the semiconductor samples can be examined without elaborate and time consuming preparation

Room temperature cathodoluminescence studies were performed using a LEO Stereoscan 440 scanning electron microscope with a special CL mirror and monochromator Samples were typically excited with an electron beam of 5-10keV and probe current of 15nA A parabolic mirror with a 1mm diameter hole in the top allows the electron beam to pass through it The electrons incident on the sample excite luminescence and while some of the photons will escape back up the hole, the collection efficiency of the mirror is quite high, ~75% [143] The focal length of the mirror is 1mm and therefore precision is required when mounting the sample The photons collected are transferred via highly reflecting mirrors to the Gatan MonoCL monochromator equipped with a 1200 lines/mm grating where the luminescence spectra can be captured The spectral resolution was approximately 1 nm

The spatial resolution of the CL is determined by a combination of a number of factors the electron beam diameter and the size of the generation volume which is related to the beam penetration depth in the material and the minority carrier diffusion length

The incident electron undergoes a successive series of elastic and inelastic scattering events in the semiconductor As a result of these scattering events, the original trajectories of the electrons are randomised, with the range of the electron penetration being a function of the electron-beam energy E_b [139]

$$R_e = (k/\rho)E_b^{\alpha} \qquad (2\ 21)$$

where ρ is the density of the material and k and α depend on the atomic number of the material and electron-beam energy Kanaya and Okayama [144] derived a general equation for the electron-beam penetration depth (measured in μm) which was found to agree well with experimental results across a wide range of atomic numbers,

$$R_e = \left(0\ 0276A/\rho Z^{0\ 889}\right)E_b^{1\ 67} \qquad (2\ 22)$$

where E_b is in keV, A is the atomic weight in g/mol, ρ is in g/cm^{3} and Z is the atomic number The excitation volume of the electrons in the sample can be controlled by changing the energy of the electron beam In this way depth profiling may be used to investigate any changes in the optical quality of the crystal as a function of distance from the substrate A Monte Carlo simulation program available for downloading [145] was used to simulate the movement of electrons through a 500nm CuCl sample on a Si substrate using the density of 1 90gcm^{1} for an evaporated CuCl thin film, measured as described for calibration of the thickness monitor in the vacuum chamber

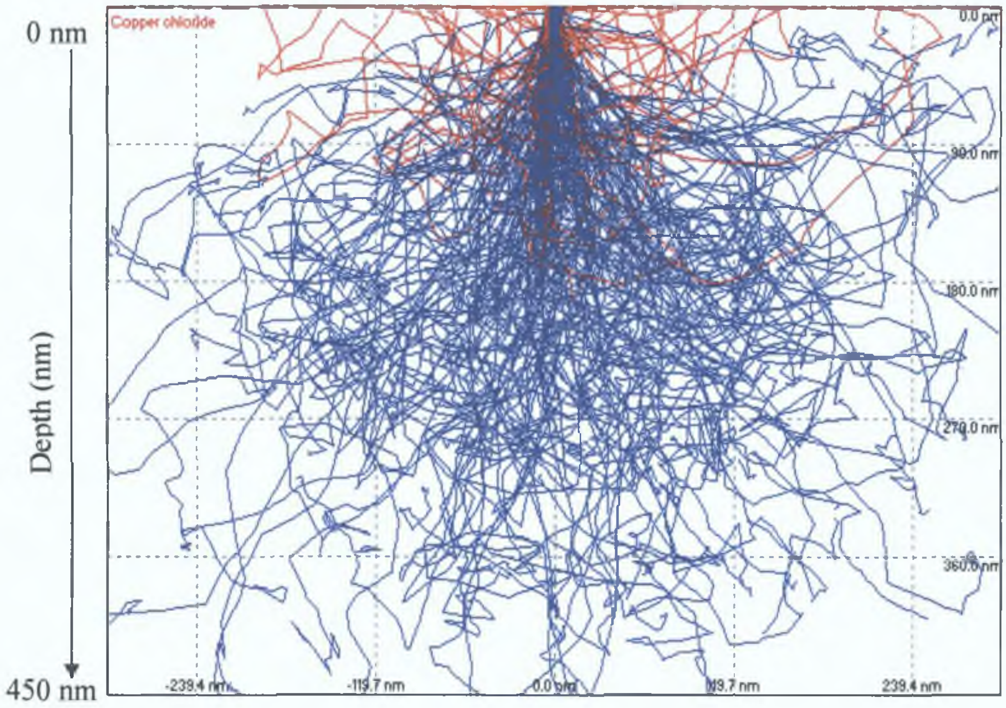

Fig. 2.12 Monte Carlo simulation for electron trajectories into a CuCl sample with an accelerating voltage = 5keV

As can be seen in fig. 2.12 an electron energy E = 5 keV will excite a large volume of a 500nm CuCl thin film. The blue part of the excitation volume represents the range of primary electrons in the material, while the red lines represent the backscattered electrons. The general shape of the excitation volume depends on the atomic number of the material, varying from a nearly pear-shaped volume for a low atomic number material, to a spherical shape for $15<Z<40$, to hemispherical for larger atomic numbers [139].

2.8 Electroluminescence

Electroluminescence (EL) is the phenomenon in which electrical energy is converted directly to luminous energy. A demonstration electroluminescent device (ELD) based on a single-insulating-layer thin film electroluminescent (TFEL) device structure consisting of a CuCl active layer grown on a silicon substrate was developed to investigate the EL characteristics of a CuCl thin film on Si. This will be discussed later in section 5.3 A schematic diagram of a general alternating current thin film electroluminescent (ACTFEL) test device structure is shown in fig.2.13.

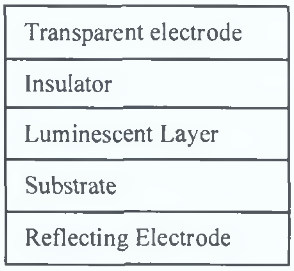

Fig. 2.13 Schematic of a typical ACTFEL device

The reflecting electrode typically has a layer thickness of 300-500nm. The main requirement is that it has a low resistivity. In addition, it must be resistant to electromigration under high electric fields. Aluminium is often used as the reflecting electrode because it has a good conductivity and resistance to ion migration, as well as being reasonably simple to deposit [146].

It is quite common in standard devices for the active layer to be sandwiched between two insulating layers which limit the current transport across the device [146]. However, in this case the research interest lies in the integration of CuCl with Si, and therefore a single insulating layer is used and the active CuCl layer is grown directly on the Si substrate. The most important requirements for the insulating layers are (1) a high dielectric constant, (2) a high electric field strength, (3) a uniform thickness, and (4) the layer must be pinhole free. To optimise device performance, it is necessary to maximise the electric field across the active layer, and minimise the field across the insulator To maximise the active layer electric field, the insulator should have a high dielectric constant and sufficient electric field strength to avoid breakdown The insulator should be processed to be as thin as possible without comprising device reliability In general, as the insulator thickness decreases, device reliability gets worse because pinholes in the films cause localised high field regions resulting in premature dielectric breakdown In our case the insulator also had the function of encapsulating CuCl to protect it from the ambient A commercially available polysilsesquioxane (PSSQ) based solution made by the Emulsitone® Inc (USA) was chosen as the insulator

The most common transparent electrode used is indium tin oxide (ITO) The optical and electronic properties of ITO films are highly dependent on the deposition parameters and the starting composition of evaporation material used ITO is optically transparent but has a high conductivity resulting from shallow donors that lie only a few meV below the conduction band [146] At room temperature, these donors are thermally activated into the conduction band and lead to high conductivity It has a resistivity of approximately 10 Ωcm and transmission >80% for typical electrode thicknesses of 300-500nm ZnO Al [147,148] has also been used as a transparent electrode However, deposition of ITO is difficult without the availability of an e-beam evaporator, or dedicated sputtering system, and to develop the knowledge necessary for preparation of ZnO contacts requires a lot of time Therefore, as a first test for our ELD, semi-transparent evaporated Al or Au contacts were used for the top electrode

The device physics of a standard ELD can be divided into four main topics, namely (1) tunnel emission of electrons from interface states, (2) acceleration of electrons to high energies, (3) impact excitation or impact ionisation of the luminescent centre, and (4) de-excitation of the excited electron by radiative (photon generation) or non-radiative recombination [146] These processes are illustrated in figure 2 14, (non-radiative recombination is omitted)

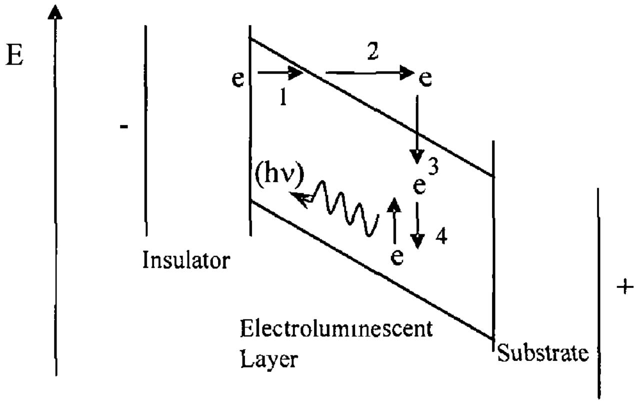

Fig 2 14 Mechanisms occurring in an ACTFEL device (1) tunnel emission of electrons from interface states, (2) acceleration of electrons to high energies, (3) impact excitation of the luminescent centre, and (4) radiative de-excitation of the excited state electron [146]

In general there are two mechanisms responsible for carrier injection in an ACTFEL device, thermionic emission and field emission or tunnelling While a pure tunnelling mechanism is expected to be temperature independent, there is a slight temperature dependence on the ACTFEL device current It is generally accepted therefore, that the electrons trapped at the electroluminescent layer/insulator interface are the carrier source, and that a thermally assisted tunnelling mechanism is responsible for their injection [146] Commercial ACTFEL devices are driven at 60Hz with a trapezoidal waveform As the voltage pulse rises, the energy bands begin to bend under the influence of the induced electric field Eventually a threshold voltage is reached when the energy bands are bent enough so that electrons tunnel into the electroluminescent layer conduction band from interface states Once the electrons are tunnel injected into the electroluminescent layer conduction band, they are accelerated under the influence of the electric field The following equation can be used to calculate the electric field in the electroluminescent layer [146],

$$E_{EL} = \frac{\varepsilon_i}{\varepsilon_i d_{EL} + \varepsilon_{EL} d_i} V_{tot} \qquad (2\ 23)$$

where ε is the dielectric constant, d is the layer thickness, and the subscripts i and EL represent the insulator and the electroluminescent layer respectively

If dopants or impurities are present in the electroluminescent material, these can act as luminescent centres After the electrons accelerate to high enough energy, they can interact with a luminescent centre and promote one of its ground state electrons The electron can either be promoted into a higher atomic state of the luminescent centre or into the conduction band of the host material

In the case of our γ-CuCl ELD, however, light emission occurs through hot-electron[g], impact excitation of electron-hole pairs The subsequent light emission is therefore intrinsic to CuCl and not dependent on the presence of impurities The most common radiative transitions which can occur in a semiconductor resulting in light emission from electron-hole recombination have already been discussed in section 2 5 Non-radiative relaxation occurs by phonon generation which produces heat from lattice vibrations Local lattice imperfections such as point defects(interstitials, vacancies),

---

[g] Hot electrons can be obtained either by raising the temperature of the whole system, or as in this case, by applying an electric field which will raise only the effective temperature of the electrons

line defects (dislocations), and volume defects (grain boundaries) all act as non-radiative recombination centres which are deleterious to the radiative efficiency of the EL device

The details of our γ-CuCl/Si ELD device structure will be discussed in section 5 3

The electroluminescence measurements of the test devices were evaluated using a SOFIE spectrophotometer with a photomultiplier tube (spectral range of 200-900 nm) The ELD device was driven by an a c sinusoidal waveform with a frequency of 1 kHz and a peak-to-peak voltage of 100V

2.9 UV-Visible spectroscopy

One of the most direct and perhaps simplest methods for probing the band structure of semiconductors is to measure the absorption spectrum In the absorption process, a photon of known energy excites an electron from a lower- to a higher-energy state Therefore by placing a semiconductor sample at the output of a monochromator and studying the changes in the transmitted radiation, one can discover the possible transitions being made by the electron Absorption is expressed in terms of a coefficient $\alpha(h\nu)$ which is defined as the relative rate of decrease in light intensity $L(h\nu)$ along its propagation path [149]

$$\alpha = \frac{1}{L(h\nu)}\frac{d\left[L(h\nu)\right]}{dx} \qquad (2\ 24)$$

The fundamental absorption refers to the band-to-band or to exciton transitions i e to the excitation of an electron from the valence band to the conduction band The fundamental absorption, easily identified by the rapid rise in absorption, can in principle be used to determine the energy gap of the semiconductor However, because the transitions are subject to certain selection rules, the estimation of the energy gap from the so called absorption edge is not a straightforward process An analysis to determine the energy gap is not pursued in this work as the presence of excitonic peaks close to the band gap edge further complicates the situation The presence of excitons usually appears as narrow peaks in the absorption edge of direct-gap semiconductors As already mentioned above (section 2 6), in direct gap materials the free exciton occurs when the photon energy is $h\nu = E_g - E_x$ At $k = 0$, this is a very pronounced transition which broadens with increasing temperature Therefore in the case of CuCl, we expect to see what are termed the $Z_{1\,2}$ and Z_3 free excitons in a low temperature absorption spectra but at room temperature one broad peak occurs which is a combination of the two free excitons Absorption and transmission spectra were recorded on a Perkin Elmer Lambda 40 UV/VIS spectrometer at room temperature in the wavelength range of 200-900nm with a resolution of 1nm One limitation of this technique is that the semiconductor film must be grown on an optically transparent substrate CuCl thin films on Si substrates therefore cannot be analysed with this method Instead films are grown on standard microscope glass slides or quartz substrates The absorption and transmission of the uncoated substrate is first measured, followed by the thin film on the substrate A subtraction is then automatically performed by the software, so that the UV-Vis spectra reported here are solely of CuCl without interference from the substrate

2.10 Resistivity

The resistivity ρ of a semiconductor is an important characteristic in the semiconductor industry because it contributes to the device series resistance, capacitance and threshold voltages. In this work is it used as an indication of the doping level of CuCl by comparing the resistivity of nominally undoped CuCl thin films, to those which have been intentionally doped. Resistivity depends on the free electron and hole densities n and p, and the electron and hole mobilities μ_n and μ_p according to the relationship [150]

$$\rho = \frac{1}{q(n\mu_n + p\mu_p)} \qquad (2.25)$$

where q is the electronic charge. Therefore, if the carrier density is increased due to doping, a corresponding drop in the value of ρ can be measured. However, the carrier densities and mobilities are generally not known and therefore an alternative measurement technique is used. The resistivity of CuCl thin films is measured using two complementary techniques: the four-point probe and van der Pauw resistivity methods. To avoid complications created by parallel conduction paths, the samples for resistivity measurements were grown on insulating glass substrates (rather than semiconducting silicon).

The resistance of the semiconductor is the ratio of the voltage to the value of the output current of the power supply. When a simple measurement of electrical resistance of a sample is performed using two wires, the total resistance R_T between the two probes is given by [150]

$$R_T = \frac{V}{I} = 2R_p + 2R_c + 2R_{sp} + R_s \qquad (2.26)$$

where R_p is the probe resistance, R_c the contact resistance at each probe/semiconductor contact, R_{sp} the spreading resistance under each probe, and R_s is the resistance of the semiconductor. The contact resistance arises from the mechanical metal probe contacting the semiconductor, while the spreading resistance arises from the resistance encountered by the current when it flows from the small metal probe into the semiconductor and vice-versa In general these contact and spreading resistances are very small compared to the resistance of the sample and can be ignored However in the case of a semiconductor they can easily obscure the desired data This difficulty is overcome by the use of a four- point probe

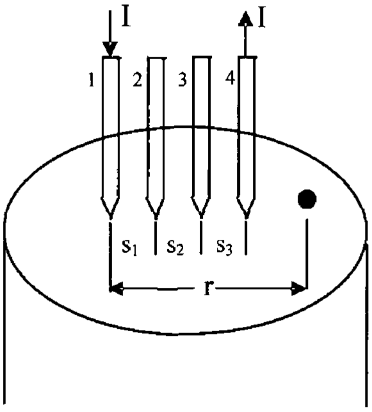

Fig 2 15 Schematic Diagram of a collinear four-point probe

The principle under which the four-point probe operates is that a constant current flows the length of the wafer through probes labelled 1 and 4 in fig 2 15 If the sample shows resistance to the flow of current there will be a drop in potential between probes 2 and 3 as the current flows across the sample Thus, since there is no potential drop across the contact resistance associated with probes 2 and 3, the parasitic resistances R_c, R_p and R_{sp} are negligible and only the resistance associated with the semiconductor, R_s, between probes 2 and 3 is measured If we consider the current I, entering through probe 1 and leaving through probe 4 as seen in fig 2 15, then the potential V at a distance *r* from an electrode carrying a current I in a material of resistivity ρ is given by the relationship [150]

$$V = \frac{\rho I}{2\pi r} \qquad (2\ 27)$$

If a semi-infinite medium is assumed (i e width of the wafer >>3s, where s is the probe separation), the voltage V_0, measured with respect to zero reference potential is,

$$V_0 = \frac{\rho I}{2\pi}\left(\frac{1}{r_1} - \frac{1}{r_4}\right) \qquad (2\ 28)$$

where r_1 and r4 are the distances from probes 1 and 4, respectively The minus sign accounts for current leaving through probe 4 The voltage at probe 2 is

$$V_2 = \frac{\rho I}{2\pi}\left(\frac{1}{s_1} - \frac{1}{s_2 + s_3}\right) \qquad (2\ 29)$$

for probe spacings s_1, s_2 and s_3 At probe 3 the voltage is given by

$$V_3 = \frac{\rho I}{2\pi}\left(\frac{1}{s_1 + s_2} - \frac{1}{s_3}\right) \qquad (2\ 30)$$

The total measured voltage $V = V_2 - V_3$ becomes

$$V = \frac{\rho I}{2\pi}\left(\frac{1}{s_1} - \frac{1}{s_2 + s_3} - \frac{1}{s_1 + s_2} + \frac{1}{s_3}\right) \qquad (2\ 31)$$

For most four-point probes, the probe spacings are equal This is the case for the typical four-point probe with collinear probes by Veeco instruments used in these experiments Therefore the above equation reduces to

$$V = \frac{\rho I}{2\pi s} \qquad (2\ 32)$$

which can be expressed in terms of the resistivity ρ as,

$$\rho = 2\pi s\left(\frac{V}{I}\right) \qquad (2\ 33)$$

ρ is usually expressed in terms of Ohm-cm, with V measured in volts, I in amperes, and s in cm In reality, semiconductor wafers are not semi-infinite in either the lateral or the vertical dimensions, therefore a correction must be applied to equation 2 33 above For an arbitrarily shaped sample, the resistivity is given by

$$\rho = 2\pi s F\left(\frac{V}{I}\right) \qquad (2\ 34)$$

where F is a correction factor which depends on the sample geometry and is a product of three independent correction factors $F = F_1 F_2 F_3$ These correct for sample thickness, lateral sample dimensions and the placement of the probes relative to the sample edge They are valid only in the regime where the sample thickness is smaller than the probe spacing As the typical thickness of the CuCl thin films studied is ~500nm, while the probe spacing is 1mm, these corrections are sufficient for the samples studied F_1 corrects for the thickness according to [150]

$$F_1 = \frac{t/s}{2\ln\{[\sinh(t/s)]/[\sinh(t/2s)]\}} \qquad (2\ 35)$$

for a non-conducting bottom wafer surface boundary, where t is the layer thickness For thin samples with $t \le s/2$ this equation reduces to

$$F_1 = \frac{t/s}{2\ln(2)} \qquad (2\ 36)$$

Combining equation 2 34 and 2 36 results in an expression for the resistivity

$$\rho = \frac{\pi t}{\ln(2)}\left(\frac{V}{I}\right) = 4\ 532t\left(\frac{V}{I}\right)F_2 F_3 \qquad (2\ 37)$$

F_2 corrects for the lateral sample dimensions according to [150]

$$F_2 = \frac{\ln(2)}{\ln(2) + \ln\{[(D/s)^2 + 3]/[(D/s)^2 - 3]\}} \qquad (2\ 38)$$

where D is the sample width of a rectangular sample In order for the correction factor F_2 to be equal to unity, the sample must satisfy $D \ge 40s$ The typical width of the samples used in this work ~2 5mm, therefore a correction must be applied Substituting into equation 2 38 for s = 1mm, results in a value of F_2= 0 986

The third correction factor, F_3, accounts for the proximity of the boundary to the probes It is dependent on whether the boundary is conducting or non-conducting [150] However when the normalised distance d from the boundary to the probes is greater than three to four probes spacings ($d \geq 4mm$ in our case which is easily satisfied), this correction factor reduces to unity Applying corrections F_2 and F_3, calculated for samples used in this study, the expression for ρ therefore becomes

$$\rho = 4\ 469t\left(\frac{V}{I}\right) \qquad (2\ 39)$$

Equation 2 39 is used for calculating the resistivity of the CuCl thin films on glass substrates Current was measured to a precision of 0 1nA and voltage to 0 1mV Slight variations in the measurements caused by fluctuations in the current and voltage readings and small changes in resistivity at different points on the sample were accounted for by taking 10 measurements on each sample, then averaging the results The standard deviation from the average measurement was used as an indication of the error in the measurement and the uniformity of the sample

Another method of measuring the resistivity of a semiconductor is by using the van der Pauw technique [151] A schematic of a rectangular van der Pauw configuration is shown in fig 2 16

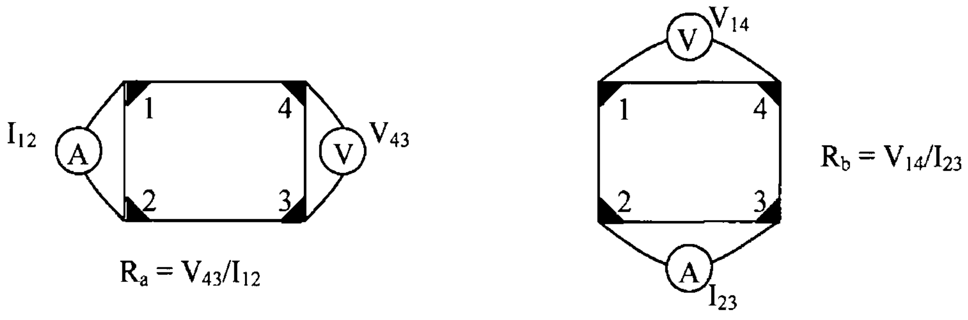

Fig 2 16 Rectangular sample used for van der Pauw resistivity measurement

With a constant current flowing, the potential between pairs of electrodes is measured as shown above The sheet resistivity ρ_s is given by [152],

$$\rho_s = \frac{\pi}{\ln 2}\left(\frac{R_a + R_b}{2}\right) f\left(\frac{R_a}{R_b}\right) \qquad (2\ 40)$$

where $R_a = V_{43}/I_{12}$, $R_b = V_{14}/I_{23}$ and $f\,(R_a/R_b)$ is a correction factor equal to unity for symmetrical structures for which $R_a = R_b$ [152] A table of correction factors to account for different probe geometries is presented by Ramadan et *al* [153] For greater accuracy the current should be reversed and measurements repeated and averaged If the thickness of the sample is known the resistivity ρ can then be calculated from $\rho = \rho_s t$, where t is the thickness of the film

2.11 Conductivity Type

The conductivity type of a semiconductor can be determined by thermal electromotive force (also know as the hot probe method), rectification and the Hall effect Rectification technique and Hall effect measurements are used in this work The Hall effect will be discussed in detail in the next section In the rectification method, the sign of the conductivity is determined by the polarity of a rectified ac signal at a point contact to the semiconductor When two probes are used, one should be rectifying and the other should be Ohmic Current flows through a rectifying contact to *n*-type material if the metal is positive and to *p*-type material if it is negative It is difficult to implement rectifying and Ohmic contacts with two-point contacts A standard four-point probe however, can be adapted for use as a rectifying probe as shown in fig 2 17 below [154]

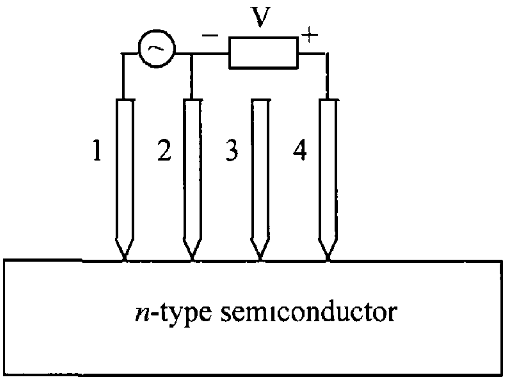

Fig 2 17 Rectifying probe for conductivity type measurements

A function generator is used to create an ac voltage which is applied between probes 1 and 2 The resulting potential is measured between probes 4 and 2 The voltage drop V_{42} is small and negative when the ac voltage at probe 2 is positive because the metal-semiconductor junction is forward biased But for a negative voltage at probe 2, the junction is reverse biased and therefore V_{42} is large and positive The large positive and small negative V_{42} result in a dc component with the polarity of the semiconductor-metal junction necessary to reverse bias the junction For *n*-type semiconductors $V_{42}>0$, and for *p*-type semiconductors $V_{42}<0$ For this work, the ac signal was a sine wave, generated at a frequency of 1MHz and a peak-to-peak voltage ~22 V

2.12 Hall Effect Measurements

The Hall Effect was discovered by E H Hall in 1879 [155] The key feature of Hall measurements is the ability to determine carrier types, carrier densities and mobilities with a relatively simple measurement Intrinsic, lightly doped or compensated semiconductors normally have two types of carriers In such a case, the quantitative interpretation of the Hall coefficient is more difficult, since both types of carriers contribute to the Hall field For the same electric field, the Hall voltage of p-carriers will be opposite in sign to that of the n-carriers The Hall theory predicts the Hall coefficient R as [156]

$$R=\frac{r(p-b^2n)}{q(p+bn)^2} \qquad (2\ 41)$$

with $b=\mu_n/\mu_p$, where μ_p and μ_n are the mobilities of holes and electrons, and p and n are the carrier densities of holes and electrons, respectively q is the magnitude of the electronic charge and r is a scattering factor whose value lies between 1 and 2 depending on the scattering mechanism in the semiconductor For lattice scattering $r=3\pi/18=1\ 18$, for ionized impurity scattering $r=315\pi/512=1\ 93$ and for neutral impurity scattering $r=1$ [156] The scattering factor is also a function of magnetic field and temperature In the high magnetic field limit r→1 The high fields necessary for r to approach unity (~ 10 Tesla) cannot be achieved in our laboratory As r is usually not known it is frequently assumed to be 1 This assumption is made for the Hall measurements described in this report

A static magnetic field has no effect on charges unless they are in motion When the charges flow, a magnetic field directed perpendicular to the direction of flow produces a mutually perpendicular force on the charges When this happens, electrons and holes will be separated by opposite forces resulting in an electric field $\bar{E}_h$ which depends on the cross product of the magnetic field intensity, $\bar{H}$, and the current density $\bar{J}$

$$\bar{E}_h = R\bar{J} \times \bar{H} \tag{2 42}$$

where R is the Hall coefficient If we consider a bar of semiconductor with dimensions x, y and thickness z with $\bar{J}$ directed along x and $\bar{H}$ along z, then $\bar{E}_h$ will be along y as shown in fig 2 18

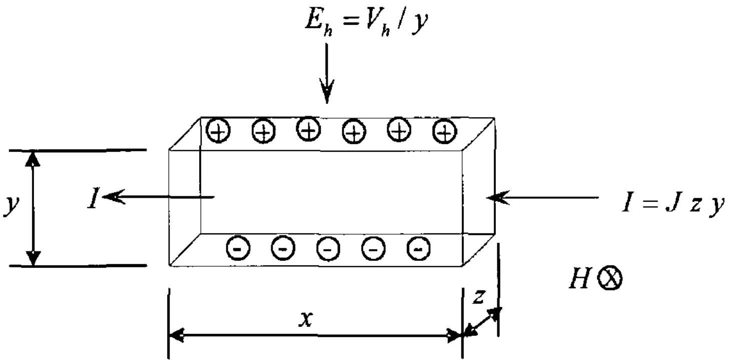

Fig 2 18 Sample for studying Hall effect

Then R can be determined experimentally as

$$R = \frac{V_h / y}{JH} = \frac{V_h z}{IH} \tag{2 43}$$

where V_h is the Hall voltage appearing between the two surfaces perpendicular to y and $I = Jyz$ In general the Hall voltage is not a linear function of magnetic field applied, i e the Hall coefficient is not generally a constant, but a function of the applied magnetic field If it is assumed that all carriers have the same drift velocity, then it is simple to calculate the Hall voltage which depends on whether there are one or two types of carrier present If we assume that one type of carrier dominates (such an assumption is valid for metals and degenerately doped semiconductors), then the magnetic force on the carriers is

$$\bar{F}_m = e\left(\bar{v} \times \bar{H}\right) \qquad (2\ 44)$$

where v is the drift velocity of the carriers It is compensated by the Hall force field

$$\bar{F}_h = e\bar{E}_h \qquad (2\ 45)$$

Assuming the directions of the various vectors as described result in the following expression for the electric field $\bar{E}_h$,

$$\bar{E}_h = \bar{v} \times \bar{H} \qquad (2\ 46)$$

The current density $\bar{J}$ is the charge q multiplied by the number of carriers traversing unit area in unit time, which is equivalent to the carrier density, n, multiplied by the drift velocity, $\bar{J} = qn\bar{v}$

Substituting into equation (2 43) gives

$$R = \frac{E_h}{JH} = \frac{vH}{qnvH} = \frac{1}{nq} \qquad (2\ 47)$$

It is clear that the sign of the Hall coefficient depends upon the sign of q Therefore in a p-type sample, R would be positive, while in an n-type sample it would be negative For a fixed magnetic field and input current, the Hall voltage is proportional to $1/n$ or its resistivity When one carrier dominates the conductivity of the material is $\sigma = nq\mu_H$, where μ_H is the Hall mobility of the carriers Substituting for n in equation (2 47) gives an expression for μ_H in terms of the Hall coefficient,

$$\mu_H = R\sigma \qquad (2\ 48)$$

Therefore the mobility can be measured experimentally R is expressed in cm^{3}Coulomb^{1}, thus μ_H is expressed in units of cm^{2}V^{1}s^{1} The Hall mobility is related to the drift mobility μ_0 by the scattering factor r $\mu_H = r\mu_0$

If the carrier concentration can be recorded as a function of temperature it is possible to extract additional information The hole concentration of a p-type semiconductor of doping concentration N_A, compensated with donors of concentration N_D is given by [157]

$$\frac{p(p+N_D)-n_i^2}{(N_A-N_D-p-n_i^2/p)}=\frac{N_v}{g}e^{-F_A/kT} \qquad (2\ 49)$$

where N_v is the effective density of states in the valence band, g is the degeneracy factor for acceptors (usually taken as 4), and E_A is the energy level of acceptors above the valence band with the top of the valence band being the reference energy For certain conditions equation 2 49 can be simplified [156]

1 At low temperatures where $p \ll N_D, p \ll (N_A - N_D)$ and $n = n_i^2/p \approx 0$

$$p \approx \frac{(N_A-N_D)N_v}{gN_D}e^{-E_A/kT} \qquad (2\ 50)$$

2 When N_D is negligibly small,

$$p \approx \sqrt{\frac{(N_A-N_D)N_v}{g}}e^{-E_A/2kT} \qquad (2\ 51)$$

3 At higher temperatures where $p \gg n_i$,

$$p \approx N_A - N_D \qquad (2\ 52)$$

According to equations (2 50) and (2 51) above, the slope of a log (p) vs 1/T plot gives an activation energy of either E$_A$ or E$_A$/2 depending on whether there is an appreciable donor concentration in the material or not At higher temperatures (room temperature and above), the net majority carrier concentration is obtained

Electrical measurements were carried out using a commercial HL5500PC Hall Effect apparatus from ACCENT The Hall voltages are obtained in the Van der Pauw configuration at typical current values of 0 1-1 0 μA Eight different measurements are taken and averaged to determine a single Hall voltage in order to minimise noise effects

2.13 Electrical contacts

In order to achieve high quality electrical measurements good metal contacts are required The choice of metal depends on whether a Schottky or Ohmic contact is desired If we assume that there are no localised states on the surface of the semiconductor, with no interfacial layer and a perfect contact between the metal and the semiconductor, the behaviour of the metal-semiconductor contact can be predicted according to Schottky-Mott theory [158] by comparing the metal work function[h] Φ_m to the semiconductor work function Φ_s In fig 2 19 (a) the metal work function Φ_m is less than the semiconductor work function Φ_s and the case of $\Phi_m > \Phi_s$ is shown in fig 2 19 (b) With this model, the barrier height Φ_B after contact is given by

$$\Phi_B = \Phi_M - \chi \qquad (2\ 53)$$

where χ is the electron affinity of the semiconductor, defined as the potential difference between the bottom of the conduction band and the vacuum level

---

[h] The work function is the potential difference between the Fermi level and the vacuum level, and is composed of bulk and surface contributions

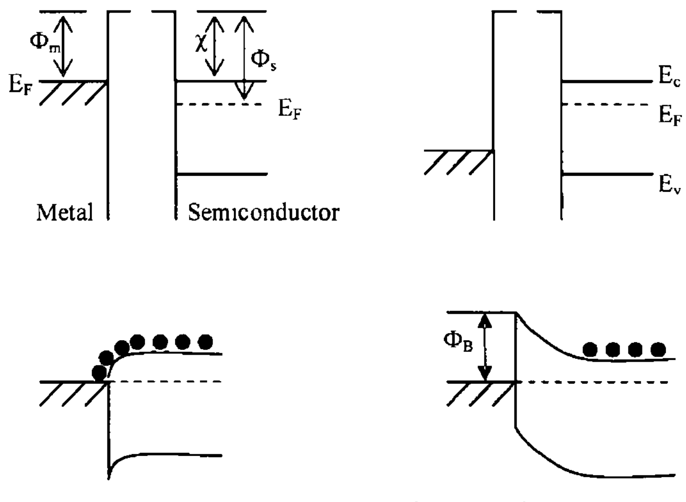

(a) Accumulation (b) Depletion

Fig 2 19 Formation of a barrier between a metal and a semiconductor The upper part of the figure shows the energy bands before contact, and the energy bands after contact are shown in the lower part of the figure

According to this Schottky-Mott theory, the barrier height therefore depends only on the metal work function and on the semiconductor electron affinity It is independent of the semiconductor doping concentration In principle it should be relatively simple to vary the barrier height by merely using metals of the appropriate work function in order to implement the accumulation or depletion contact type, so called because the majority carriers are accumulated or depleted compared to their concentration before the energy bands come into contact

For this work ohmic contacts to CuCl were desirable for Hall effect measurements An accumulation-type contact is the preferred ohmic contact because electrons in the metal and in the semiconductor encounter the least barrier to their flow into or out of the semiconductor In practice it is very difficult to alter the barrier height by using metals of different work functions The relative constancy of the barrier height with work function of metals is known as Fermi level pinning, due to the fact that the Fermi level in the semiconductor is pinned at some energy in the band gap to create a depletion-type contact The Fermi level pinning in GaAs has been widely investigated and it was found that the same pinning energies are observed for some metals e g Au, Ag and Cu, on n-type and p-type GaAs crystals [159] The measured barriers for most metals lie within a narrow range of about 0 3eV, being largest for the electronegative metals on n-type crystals Many definitions exist for an Ohmic contact as discussed by Look [160] who states that in the particular case of Hall effect measurements an ohmic contact is best defined as a source of carriers with an internal resistance, which is totally negligible compared with the semiconductor resistance or a source of carriers with non-negligible internal resistance, but one which obeys Ohm's law for current densities of interest As barrier height engineering is an impractical means of implementing ohmic contacts another approach is required Although the barrier height is independent of doping concentration, the barrier width does depend on the doping concentration [161] with the space-charge region width being proportional to $N_D^{1/2}$ For low levels of doping ($N_D \leq 10^{17}\mathrm{cm}^{3}$) the current flows as a result of thermionic emission, with electrons thermally excited over the barrier In the intermediate doping range ($10^{17} < N_D < 10^{19}\ \mathrm{cm}^{3}$) thermionic-field emission occurs where the carriers are thermally excited to an energy where the barrier is sufficiently narrow for tunnelling to take place At high doping levels ($N_D > 10^{19}\ \mathrm{cm}^{3}$) with narrow space-charge region widths, the barrier is sufficiently narrow at or near the bottom of the conduction band for the electrons to tunnel directly, known as field emission [150] Practical considerations are that the contacts must be able to supply the necessary device current, and the voltage drop across the contact should be small compared to the voltage drop across the active device region An Ohmic contact should not degrade the device to any significant extent and it should not inject minority carriers Additionally, it should be possible to make such contacts in a reproducible manner

Chapter 3

Structural Properties of CuCl

3.1 X-Ray Diffraction Results

Following deposition of CuCl on substrates of glass, Si (100) and Si (111), x-ray diffraction (XRD) measurements were performed to monitor the crystallinity of the deposited CuCl thin films These XRD scans were then compared to the International Centre for Diffraction Data (ICDD) powder diffraction files as provided by the manufacturer and to the XRD trace of the starting CuCl powder which was compressed into a pellet and measured

The positions of the main CuCl peaks and their relative intensities as measured by powder diffraction are listed in table 3 1

2θ	Intensity (%)	*h*	*k*	*l*
28 522	100	1	1	1
33 027	8	2	0	0
47 437	55	2	2	0
56 290	30	3	1	1

Table 3 1 Expected ratios of different CuCl peaks from Powder diffraction files [162]

Our CuCl starting material (Merck 97%) was compressed into a pellet and the diffraction pattern measured using the Bragg-Brentano geometry (section 2 2)

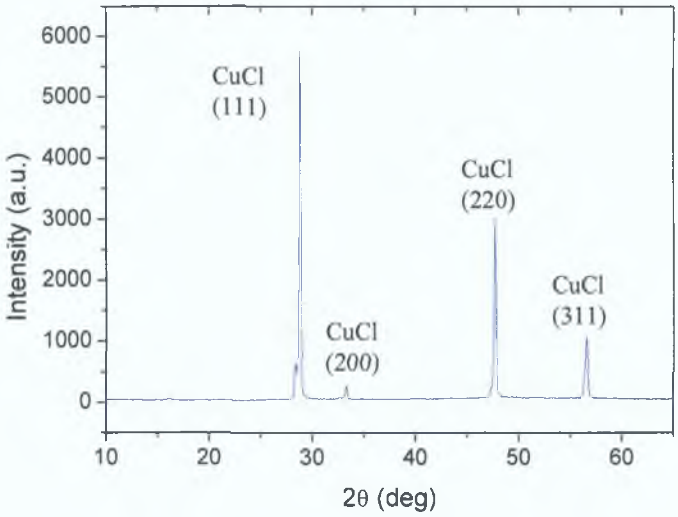

Fig. 3.1 X-ray θ-2θ diffraction pattern of compressed CuCl powder

From fig. 3.1 it is clear that as expected the CuCl (111) reflection is the most intense. The intensities of the CuCl (200), (220) and (311) reflections are 4.4%, 52.2% and 18.5% respectively with respect to the CuCl (111) intensity. Comparing these figures to the standard powder diffraction values given in table 3.1 it seems that although the intensity of the CuCl (220) reflection is within a few percent of the expected value, the CuCl (311) and (200) reflections are considerably smaller than those given for the standard CuCl powder. This information is used as a baseline when considering the growth of CuCl on substrates of different orientation.

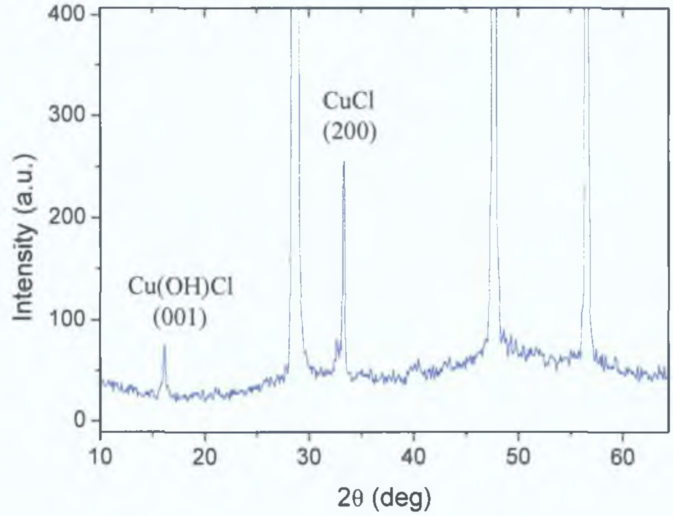

Fig. 3.2 X-ray θ-2θ diffraction pattern of compressed CuCl powders showing low intensity region

Focussing on the low intensity region of the spectrum (fig. 3.2) reveals a small weak peak at $2\theta \approx 16^o$. As already mentioned, when exposed to light and moist air, hydrated oxyhalides of Cu^{++} are formed, the so-called "green phase" of CuCl [49]. This CuCl powder of 97% purity is supplied in a sealed container but it is not stored under vacuum, therefore it is reasonable to assume that this reaction has occurred in the starting material, at least on a small scale. The oxidised Cu ions are reported to form compounds of $CuCl_2$ and Cu(OH)Cl [163]. In this case examination of the powder diffraction files [162] indicates that the reflection is due to (001) oriented crystals of Cu(OH)Cl.

A thin film of CuCl (~ 500nm) was deposited on a glass substrate at room temperature using the described vacuum deposition technique and XRD was used to examine the crystallinity. Indexing of the interplanar spacings using the Bragg equation for the cubic unit cell, $h^2 + k^2 + l^2 = \frac{4a^2}{\lambda^2}\sin^2\theta$ (where h,k,l are the Miller indices, a is the lattice constant, λ is the incident radiation wavelength and θ is the Bragg angle) confirmed that the CuCl was in the cubic zincblende form as expected at room temperature. The diffraction pattern is shown in fig. 3.3 below.

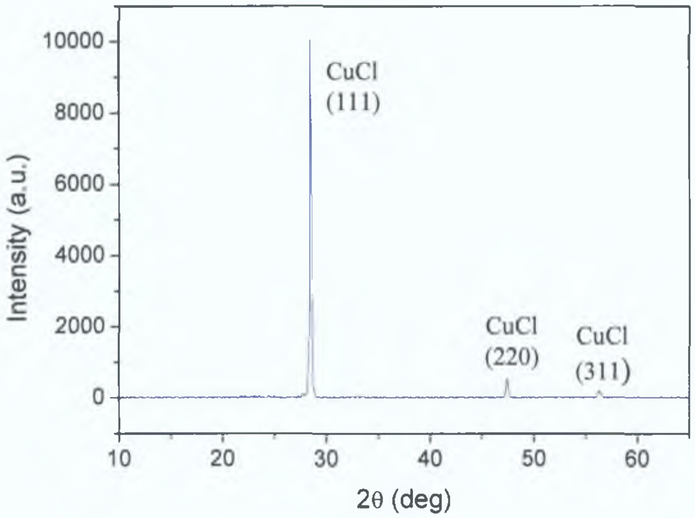

Fig. 3.3 X-ray θ-2θ diffraction pattern of evaporated CuCl thin film on a glass substrate.

Glass is an amorphous substrate and therefore should have no influence on the crystal orientation of a thin film grown upon it. The evaporated CuCl film on glass is strongly oriented in the <111> direction, which confirms that this is the preferred growth direction of the CuCl. CuCl (220) and (311) reflections are still present but their percentage intensity is much reduced compared to the diffraction pattern of CuCl powder. For this sample we see no evidence of a CuCl (200) peak. It is also interesting to note that despite the presence of a small Cu(OH)Cl peak in the starting powder, it does not appear in the evaporated sample. This may be due to the resistive heating of the CuCl under vacuum during the deposition process, as it has been reported that dihalides will decompose into monohalides during heating under vacuum and thus helps to purify the starting material [49].

(111) Silicon wafers cut off orientation by 2-4° towards the (110) plane (to aid epitaxial growth) are also used as substrates for CuCl deposition. The XRD pattern for a typical sample of CuCl on Si (111) is shown in fig. 3.4

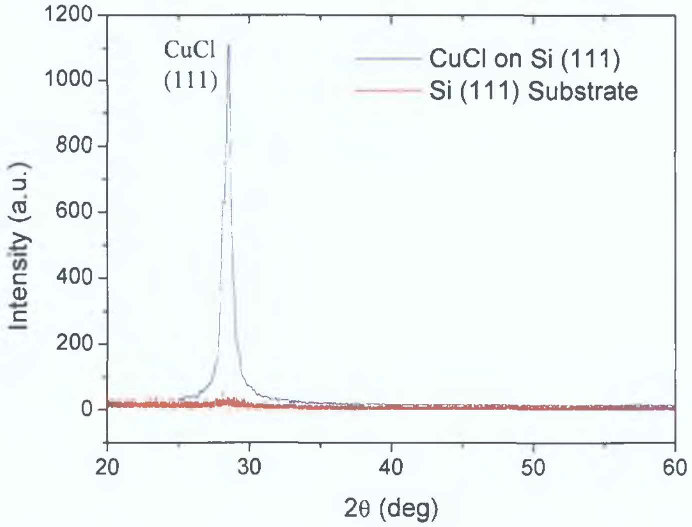

Fig. 3.4 X-ray θ-2θ diffraction pattern of evaporated CuCl thin film on a Si (111) substrate. The diffraction pattern of a Si (111) substrate is shown for comparison.

The only peak clearly seen in the Bragg-Brentano geometry for CuCl grown on a Si (111) substrate is an intense CuCl (111) reflection at 2θ ≈28.50°. Due to the small difference in the lattice constants of CuCl and Si, the Bragg peaks appear at similar 2θ values in the XRD spectra. The trace of our Si (111) substrate in the Bragg-Brentano geometry is shown for comparison. A silicon (111) reflection should appear at 2θ = 28.44°, however in this case due to the slight cutting off-orientation from the <111> direction of the silicon, it is only possible to see a diffraction peak from the Si substrate if a tilt is applied This suggests that the CuCl does not grow in perfect alignment with the Si substrate as it would then also be necessary to tilt the sample in order to see the CuCl (111) reflection As no tilt was applied for this measurement, the peak seen in fig 3 4 can be confidently assigned as a CuCl (111) reflection

A 2θ-omega (ω) geometry can be used to see the Si (111) peak as shown below

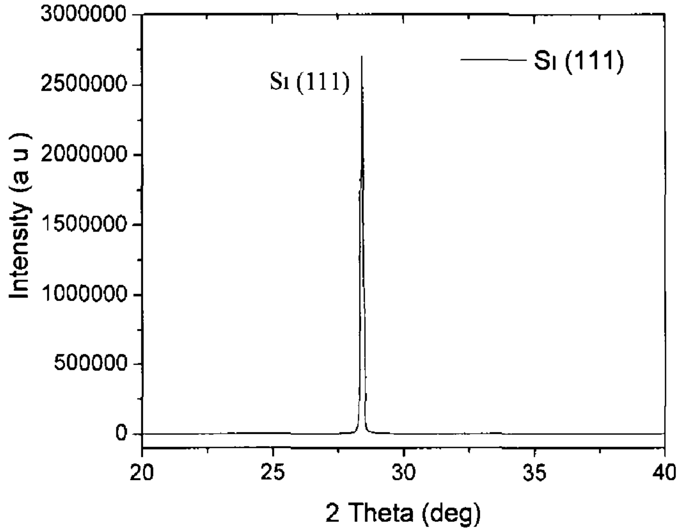

Fig 3 5 X-ray 2θ-ω diffraction pattern of a Si (111) substrate

In the 2θ-ω geometry the diffraction peak of interest is first analysed by performing a rocking curve The detected offset between the θ and 2θ angles due to the tilt of the lattice planes found from the rocking curve peak position can be used when scanning over the full 2θ range with a 2θ-ω scan An intense Si (111) reflection is detected in this way, but it is then impossible to separate the relatively weak CuCl (111) reflection from the dominating Si (111) reflection so no information is gained regarding the growth of the CuCl thin film

A rocking curve is used to further investigate the growth of CuCl on Si (111)

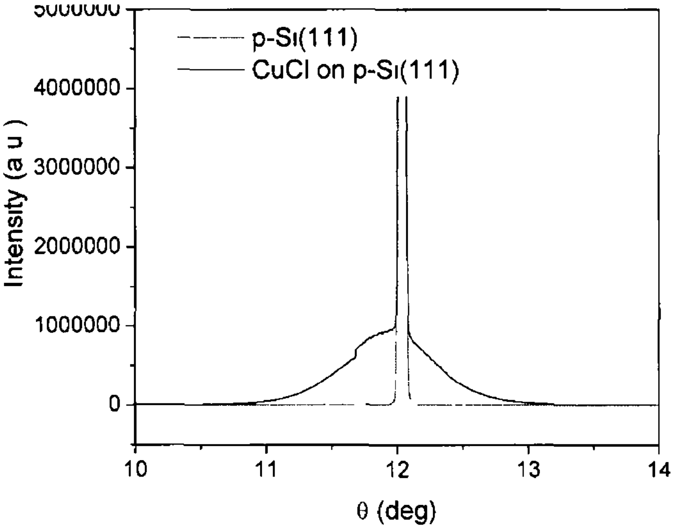

Fig 3 6 Rocking Curve of Si (111) and CuCl on Si (111)

A rocking curve of the Si (111) substrate is compared to the rocking curve of CuCl on Si (111) If the Si sample were cut perfectly along the <111> direction the peak of the rocking curve would be expected to appear at θ ≈14 22° as the Bragg peak occurs at 2θ ≈28 44° In this case the rocking curve peak is centred at θ ≈12 05° This confirms that the (111) wafers are cut slightly off-orientation by ~ 2° For the CuCl thin film sample, a broadening is seen at the base of the Si rocking curve peak This is most likely due to the presence of CuCl (111) grains that are growing close to, but not commensurately with the single crystal Si substrate

Glancing angle (GA) XRD is used to determine whether there are any other polycrystalline peaks near the surface of the CuCl thin film

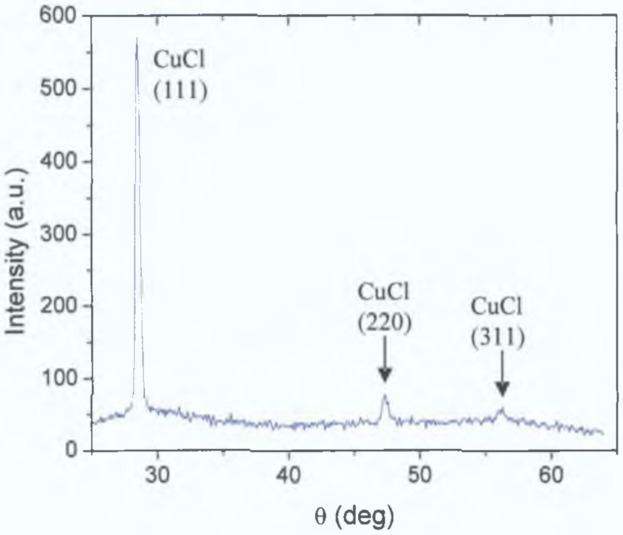

Fig. 3.7 Glancing Angle diffraction pattern (θ = 5°) of evaporated CuCl thin film on a Si (111) substrate.

A slightly less intense CuCl (111) peak appears in the glancing angle diffraction pattern as compared to the θ-2θ scan. A small signal from CuCl (110) planes and a very weak CuCl (311) reflection is also evident suggesting that there may be some relaxation of the CuCl lattice near the surface as the influence of the (111) oriented Si substrate is reduced.

The penetration depth t_p, (measured perpendicular to the surface) at which the intensity of the outgoing reflected x-ray beam has dropped to e^{-1} that of the incident beam due to absorption, was calculated using the kinematical approximation given by [164]

$$t_p = \frac{1}{\mu(\lambda)\left(\frac{1}{\sin\phi_i} + \frac{1}{\sin\phi_f}\right)}; \phi_i, \phi_f \gg \phi_c$$

where $\mu(\lambda)$ is the wavelength –dependent linear absorption coefficient, ϕ_i is the incidence angle, ϕ_f is the exit angle, and ϕ_c is the critical angle of total reflection measured from the wafer surface As the CuCl is polycrystalline the kinematical approach is valid, for a perfect low-absorption single crystal it would be necessary to use dynamical theory The attenuation length is defined as the depth into the material measured along the surface normal where the intensity of x-rays falls to 1/e of its value at the surface The attenuation length (L) of x-rays through a crystal varies according to the density of the compound and the energy of the x-rays A free software program that calculates the x-ray attenuation length as a function of energy, for a given set of material parameters is available to download [165] An example of a calculation performed for CuCl with a density of 4 14 gcm^{3} is shown in fig 3 8

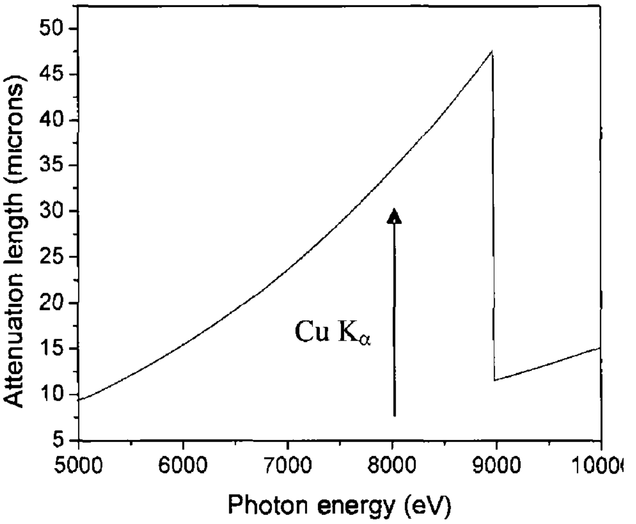

Fig 3 8 Attenuation length of x-rays in CuCl as a function of energy The energy of CuK_α radiation is indicated by the arrow

$\mu(\lambda) = 1/L(\lambda)$ Therefore the penetration depth of the x-rays into the CuCl sample can be calculated for the various diffraction peaks at a given glancing angle

	Bragg Angle	**G.A.= 5°**	**G.A.= 4°**	**G.A.= 3°**	**G.A.= 2°**	**G.A.= 1°**	**G.A.=0.5°**
CuCl (*hkl*)	t_p (μm)	t_p (μm)	t_p (μm)	t_p (μm)	t_p (μm)	t_p (μm)	t_p (μm)
(111)	5.70	2.60	2.14	1.66	1.15	0.593	0.302
(200)	6.58	2.65	2.18	1.68	1.16	0.596	0.303
(220)	9.18	2.75	2.25	1.72	1.17	0.601	0.304
(311)	10.59	2.78	2.27	1.74	1.18	0.602	0.304

Table 3.2 Penetration depths of x-rays in CuCl for various glancing angles (G.A.). (The penetration depths at the Bragg angles are shown for comparison)

It is possible to see these low intensity peaks more clearly in the glancing angle scan as the x-rays do not penetrate as far into the substrate resulting in a relatively larger contribution from the surface layers.

CuCl was grown on (100) silicon using exactly the same procedure as for the other substrates. The XRD pattern for a typical sample is shown in fig. 3.9.

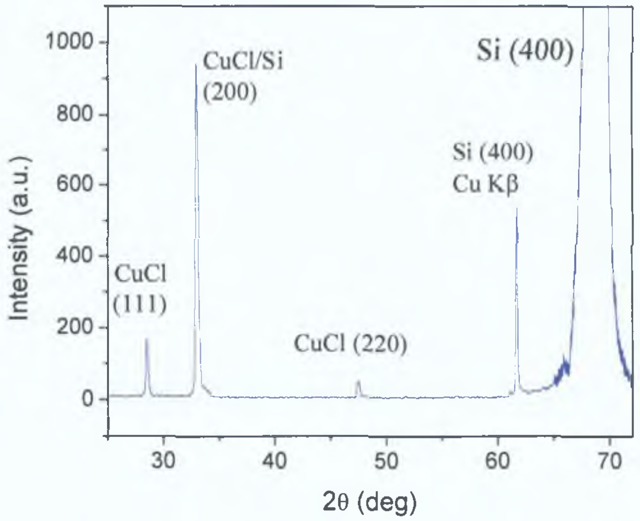

Fig. 3.9 X-ray θ-2θ diffraction pattern of evaporated CuCl thin film on a Si (100) substrate.

In this Bragg-Brentano geometry there is evidence of CuCl (111) and (220) crystal planes indicating that the CuCl thin film is polycrystalline in nature The large truncated peak at around 69° is the (400) reflection of the Si (100) substrate The peak at 61 7° is attributed to a Si (400) reflection from Cu K_β x-rays that have not been entirely filtered out An unfiltered Cu K_β x-ray would be 17% of the intensity of a Cu $K_{\alpha 1}$ x-ray [166] In this case the intensity of the Si (400) reflection at 61 7° is just 0 1% of the intensity of the main Cu K_α Si (400) reflection This explains why there is no evidence of Cu K_β x-ray peaks for any of the CuCl reflections, as any peak present would be lost in the background noise level We also see a relatively large peak at $2\theta \approx 33$ 00° The corresponding interplanar spacing coincides with a CuCl (200) reflection and a (200) reflection of Si The Si (200) reflection is forbidden due to its vanishing structure factors [167], however multiple diffraction can occur from the planes of a single crystal resulting in a final diffracted beam, which may appear to correspond to a forbidden reflection [168] We found that the intensity ratio of the CuCl (111) to (200) peaks varied dramatically depending on the rotation of the sample with respect to the x-rays, an example of which is shown in fig 3 10

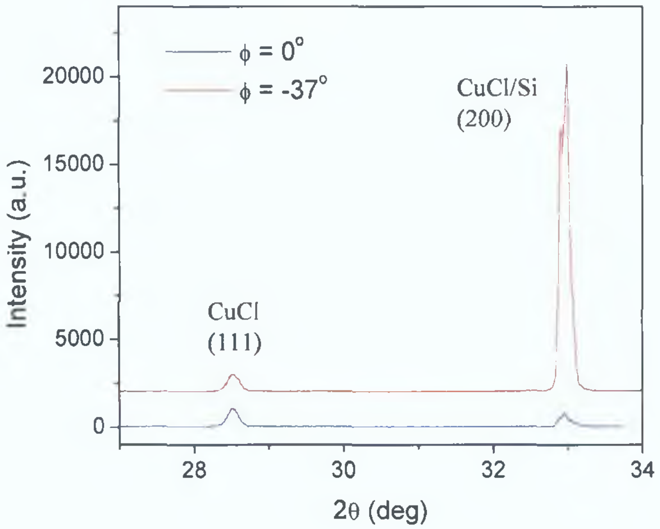

Fig. 3.10 X-ray θ-2θ diffraction pattern of evaporated CuCl thin film on a Si (100) substrate as a function of phi (ϕ) rotation.

By rotating the substrate by -37 degrees the CuCl (200)/(111) intensity ratio changed from 0.78 to 18.6. The ϕ dependence of the Si (200) multiple diffraction peaks was investigated by fixing the θ and 2θ angular positions to that of the theoretical Si (200) peak at 33.0° and rotating a Si (100) substrate by 360°.

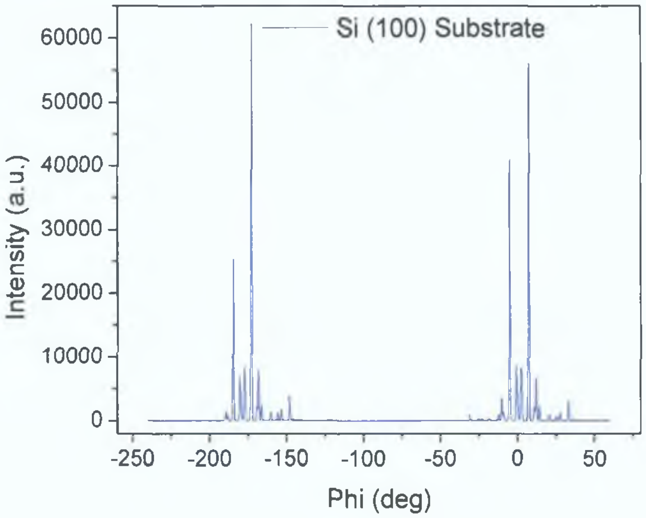

Fig. 3.11 ϕ scan of Si (200) Reflection

Two sets of multiple diffraction peaks occur centred around 0° and -180° consistent with the expected twofold symmetry of a Si (100) oriented substrate. Depending on the precise rotational angle of the substrate, a Si (200) reflection of varying intensity will appear in the diffraction pattern acquired in Bragg-Brentano geometry explaining the difference in the CuCl (200)/(111) intensity ratio shown in fig. 3.10. Evidently the Si (200) multiple diffraction peak can be eliminated from the spectra of CuCl on Si by careful choice of the ϕ rotational angle. However this would also result in the removal of any peaks resulting from lattice planes aligned in the same direction, such as the intense Si (400) reflection at ~69°, but also the CuCl (200) reflection at ~33°. Fig. 3.12 below shows the ϕ scan of a CuCl on Si (100) substrate with the 2θ angle fixed at 33.00°, resulting in multiple reflections, superimposed on the very intense diffraction pattern of a ϕ scan of the Si (400) reflection with 2θ angle fixed at 69.14°.

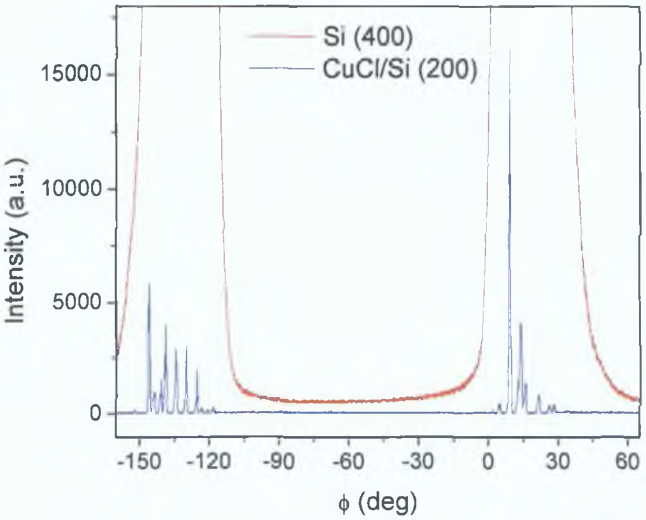

Fig. 3.12 ϕ scan of the Si (400) reflection and the CuCl/Si (200) reflection

Therefore, it is very difficult to confidently separate the CuCl and Si contributions to the diffraction peak occurring at 33°. At best we can suggest that the peak at $2\theta \approx 33°$

results from a combination of a CuCl (200) reflection indicating that there may be some epitaxial growth in the <100> direction on (100) Si, and a multiple diffraction peak from the Si substrate.

A glancing angle of 5°, which limits the penetration depth of the x-rays into the sample, was used to investigate the surface layers of the CuCl thin film. As can be seen in fig. 3.13 the surface layer of the CuCl thin film on a Si (100) substrate is a mixture of crystalline orientations.

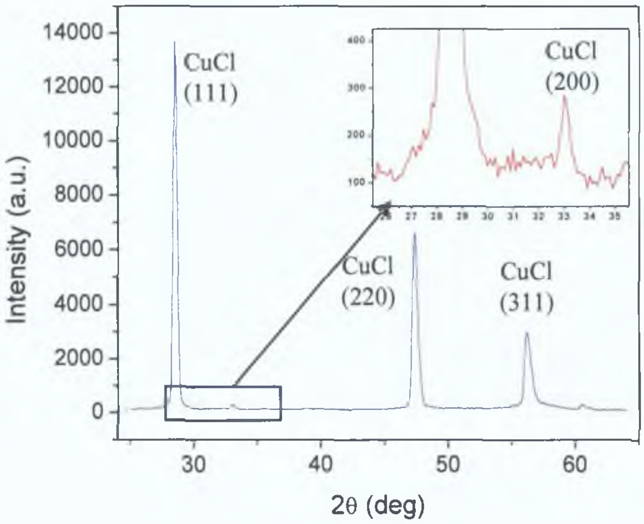

Fig. 3.13 Glancing Angle diffraction pattern (θ = 5°) of evaporated CuCl thin film on a Si (100) substrate. Inset: Low intensity region showing weak CuCl (200) reflection

The main reflection is CuCl (111) but CuCl (220) and (311) reflections are now clearly visible and much more intense than in the Bragg geometry (fig.3.9). The x-ray penetration depths calculated at the Bragg angle of the main CuCl reflections and at a glancing angle of 5° (table 3.2) is shown schematically below.

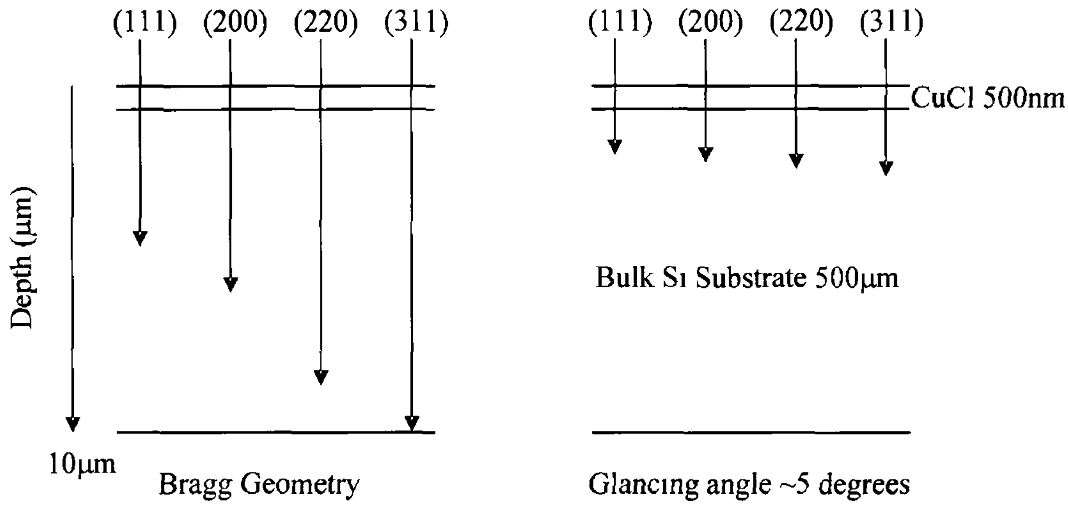

Fig 3 14 A schematic diagram comparing the x-ray penetration depth at the Bragg angle of the main CuCl reflections and at a glancing angle of five degrees

At a glancing angle of 5°, the x-ray penetration depth is reduced by a factor of ~ 3 at the angle corresponding to the (220) and (311) crystalline planes, respectively As there is a much smaller volume of the bulk Si being probed, the relative contribution of CuCl (220) and (311) crystalline planes to the total diffraction pattern is much increased

There is only a very small CuCl (200) reflection which is shown in the inset of fig 3 13 Comparing the glancing angle scan to the diffraction pattern of compressed CuCl powder (fig 3 1) we see a close similarity between the relaxed surface layers of the CuCl thin film on Si (100) and that of the starting CuCl powder As only polycrystalline grains contribute to the diffraction pattern in the glancing angle scan, this is consistent with a CuCl growth process, which tends to relax to a polycrystalline (111) preferential orientation as the growth proceeds away from the (100) Si surface The GAXRD scan of CuCl on Si (111) was dominated by a CuCl (111) diffraction peak and revealed only very weak signals from CuCl (220) and (311) crystals (fig 3 7) It thus appears that less structural relaxation occurs near the surface for CuCl on Si (111) as compared to Si (100), as the film is growing in its preferred orientation

The crystallite size can be estimated from the broadening of the diffraction peak using the Scherrer formula [169]

$$L = (0\ 9)\lambda / (\Delta\theta * \cos\theta_0)$$

where L is the crystallite size (in nm), λ is the wavelength of the x-rays, $\Delta\theta$ is the adjusted FWHM of the diffraction peak (in radians) and θ_0 is the diffraction angle A geometrical correction factor of 0 9 is introduced to account for particle shapes Any additional instrumental broadening arising from the slit width and penetration depth is accounted by $\Delta\theta$, given by $\Delta\theta = (FWHM^2_{sample} - FWHM^2_{standard})^{1/2}$ The crystallite size of the standard sample should be large enough to eliminate all particle-size broadening, thus a measurement of the instrumental broadening is obtained A single crystal Si (111) wafer analysed under the same experimental conditions was used for this purpose The average crystallite size estimated by applying this formula was 58nm, 55nm and 73nm for the CuCl (111) oriented crystallites on glass, Si (111) and Si (100) substrates, respectively

3.2 Micro-Raman Spectroscopy Results

Micro-Raman spectroscopy is used to gain information on the vibrational modes of CuCl thin films on silicon substrates The measurements were performed by a Jobin Yvon LabRam HR800 μRS system in backscattering geometry using a 488 nm Ar^+

laser excitation at room temperature. A 100× objective was used to focus the laser source to a diameter of about 1 μm on the sample surface. The Raman signal from the sample was collected by the same objective and detected by a liquid nitrogen cooled charge coupled device (CCD) detector. A confocal hole of 300 μm and a grating of 1800 g/mm were chosen for the experiments. Before measurement the equipment was calibrated carefully with a strain free silicon Raman peak position. For a 500nm CuCl thin film, the penetration depth of the laser light is at least as far as the silicon substrate. The zincblende structure contains two atoms in the primitive cell. Group theory predicts that there is only one triply degenerate fundamental optic mode, which is both Raman and infrared active. This mode is split into a transverse (TO) and longitudinal (LO) phonon mode [170,171].

The spectrum of CuCl on Si (100) is compared to that of a bare Si wafer below.

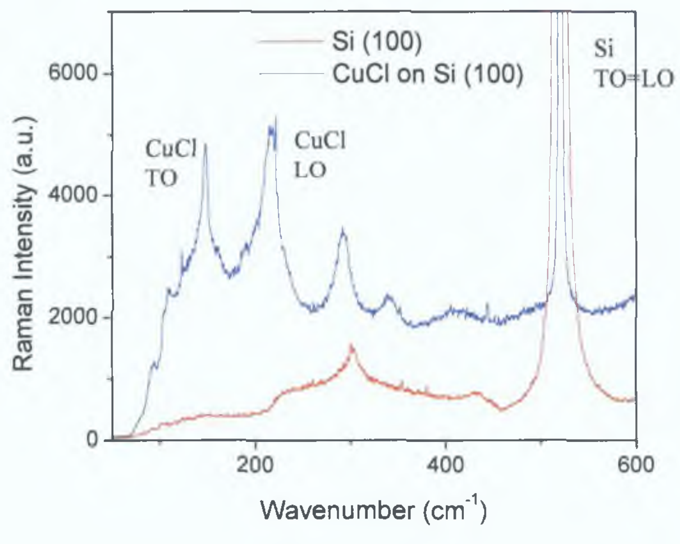

Fig. 3.15 Micro-Raman spectra of CuCl thin film on a Si (100) substrate compared to the spectrum of a Si (100) substrate

The degenerate Si-Si mode at a Raman shift of ~ 520 relative wavenumbers (520 Rcm ^{1}, or conventionally, 520cm ^{1}) is seen for both the Si substrate and for the CuCl thin film on Si confirming that the laser penetrates into the Si substrate The Si peak is considerably weaker for the CuCl sample, which indicates that CuCl has absorbed some of the laser light before it reaches the substrate The Raman peak positions were extracted by performing a baseline correction and applying a Gauss/Lorentz band-fitting function provided by the manufacturer The accuracy is approximately 0 04 cm ^{1}

Five main peaks are identified in the spectrum of CuCl on (100) Si at 148 03cm ^{1}, 216 23cm ^{1}, 292 38cm ^{1}, 341 68cm ^{1} and 521 17cm ^{1} A broad band is also present centred at 411 34 cm ^{1} The peak at 521 17cm ^{1} is the main Si-Si mode of the underlying Si substrate Much of the Raman data for CuCl available in the literature is measured at low temperatures (2-40K) and on bulk CuCl single crystals The LO phonon of CuCl is reported to appear at a phonon frequency of ~ 205cm ^{1}- 209cm ^{1}, and the TO phonon in the range of 140cm ^{1}-180cm ^{1} [172,173,174] It is therefore reasonable to assign the peak at ~148cm ^{1} to a TO CuCl mode and the peak at ~216cm ^{1} (although slightly blue-shifted compared to literature values) to a LO CuCl mode The slight difference in position of the modes is probably due to the broadening of Raman features at room temperature compared to low –temperature measurements The polycrystalline nature of our CuCl thin films as determined by X-ray diffraction also leads itself to the broadening of peaks in the Raman spectrum The peak at 292 3cm ^{1}, although close to a Si mode at ~302cm ^{1}, is probably not attributable to Si, because the intensity of this peak is much greater for the CuCl film on Si than for the Si substrate, while the main Si mode at ~520cm ^{1} is seen to decrease in intensity due to the absorption of some of the laser light by CuCl. The peaks at 292.3cm^{-1}and 338.4cm^{-1} have not been definitely identified. They may result from a Si-Cl or Si-Cu vibration, one possibility being a trichlorosilyl (Cl_3Si) vibration which would appear at ~ 282cm^{-1} [58]. For comparison, the Raman spectra of CuCl on a Si (111) substrate were also measured.

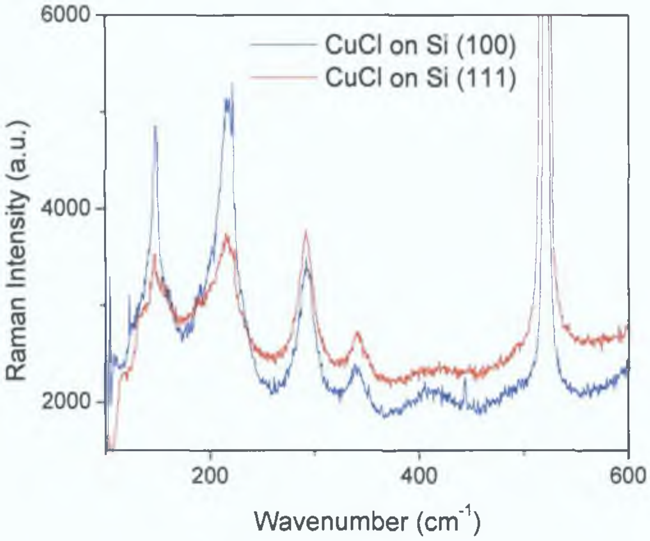

Fig. 3.16 Micro-Raman spectra of CuCl on Si (100) and Si (111) substrates

The spectra are similar for CuCl on (100) and (111) silicon although for these samples the CuCl TO and LO peaks are better defined for CuCl on (100) substrate.

3.3 Effect of Heat Treatment on CuCl

The melting point of CuCl is 430°C while that of silicon is 1414°C; therefore heating of CuCl to temperatures above its melting point can be carried out while Si remains in the solid phase. As discussed above, vacuum deposition of CuCl on Si at room temperature results in a polycrystalline thin film. In an attempt to improve the crystalline structure of CuCl on Si and encourage epitaxial growth, CuCl was deposited on a (100) Si substrate at room temperature, and then annealed in nitrogen gas in the temperature range of 50°C - 430°C. Fig. 3.17 shows the XRD patterns taken immediately after evaporation and again after solid phase re-growth.

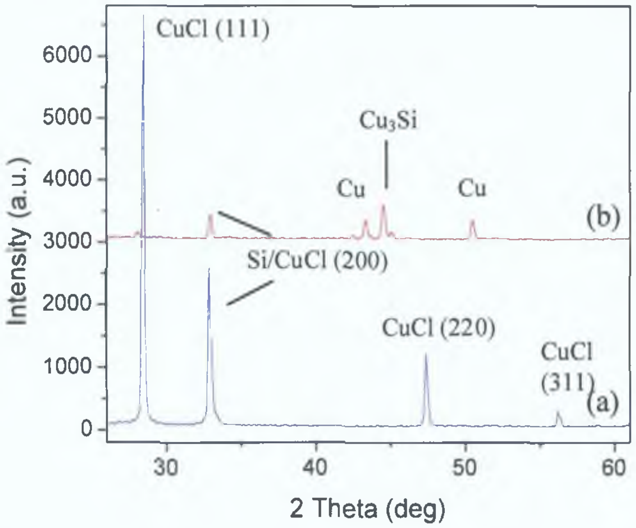

Fig. 3.17 X-ray diffraction patterns of CuCl deposited on (100) Silicon (a) As deposited (b) After heating above the melting point of CuCl for 5 minutes and cooling slowly to room temperature.

A drastic change in the XRD pattern of CuCl on Si occurs following the re-growth. The characteristic CuCl cubic zincblende diffraction pattern has vanished and several new peaks have been introduced into the spectrum. These are attributed to Cu metal and η-Cu_3Si, which are formed by a reaction between CuCl and Si. The complete reaction taking place is $Si + 4CuCl \rightarrow SiCl_4 + 4Cu$. However studies on the reaction mechanisms of Si and CuCl [175,176,177] have reported that the reaction takes place through a series of simultaneous and successive reactions,

$$7Si + 12CuCl \rightarrow 3SiCl_4 + 4Cu_3Si$$

$$31Cu_3Si + 12CuCl \rightarrow 3SiCl_4 + 7Cu_{15}Si_4$$

$$9Cu_{15}Si_4 + 20CuCl \rightarrow 5SiCl_4 + 31Cu_5Si$$

$$Cu_5Si + 4CuCl \rightarrow SiCl_4 + 9Cu$$

In such a scheme Cu and $SiCl_4$ are the final products of the reaction, while Cu_3Si, Cu_5Si and $Cu_{15}Si_4$ are unstable intermediate products. A detailed identification of the XRD peaks is shown below.

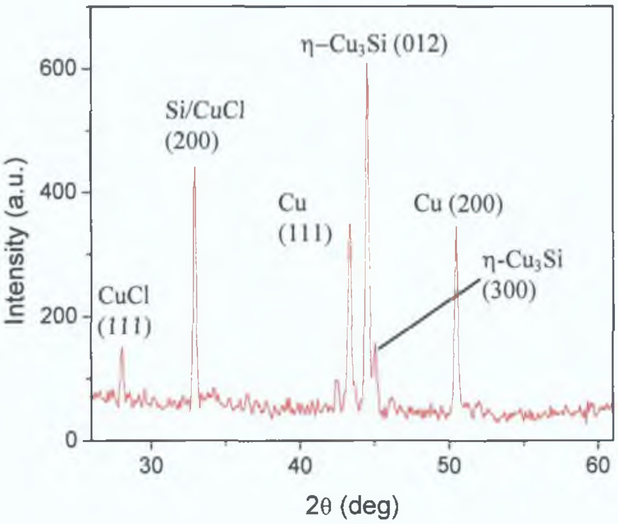

Fig. 3.18 XRD pattern of CuCl deposited on (100) Silicon after heating above the melting point of CuCl and cooling slowly to room temperature.

There is no definite evidence of Cu_5Si or $Cu_{15}Si_4$ in our XRD pattern but it seems reasonable to attribute the peaks around 44.5° to the orthorhombic η-Cu_3Si compound as the peak positions are in close agreement with the values found in the powder diffraction files [162]. $SiCl_4$ forms in the gaseous state, so is not evident in the XRD pattern. The small, unidentified peaks around 43° and 46° are probably copper oxide peaks (CuO_x), as we know that Cu metal is present and it has a very strong affinity for oxygen.

The reaction observed between Si and CuCl can be predicted by examining the thermodynamics of the balanced reaction equation. By examining the heats of formation of reactants and products it is found that a reaction will only take place if the total value of the Gibbs Free Energy of Formation (ΔG_f) of the products is more negative (and therefore more stable) than the total ΔG_f of the reactants [178]

$Si(s) + 4CuCl(s) \rightarrow SiCl_4(g) + 4Cu(s)$

The ΔG_f values of Si, CuCl, $SiCl_4$ and Cu are 0, -119 9, -617 0 and 0kJmol^{1}, respectively

$$\Rightarrow \Delta G_f \text{ (L H S)} = -479\ 6 \text{ kJmol}^{1}$$

$$\Delta G_f \text{ (R H S)} = -617\ 0 \text{ kJmol}^{1}$$

Using the above values from [179], it is calculated that the products of $SiCl_4$ gas and Cu are more stable than Si and CuCl and this explains why the reaction occurs upon heating of a CuCl thin film on a Si substrate A series of experiments were performed to determine the temperature at which this reaction occurs It was found that a reaction occurs between Si and CuCl on heating above 250°C resulting in the formation of metallic Cu, which was evident in the XRD pattern shown in fig 3 19

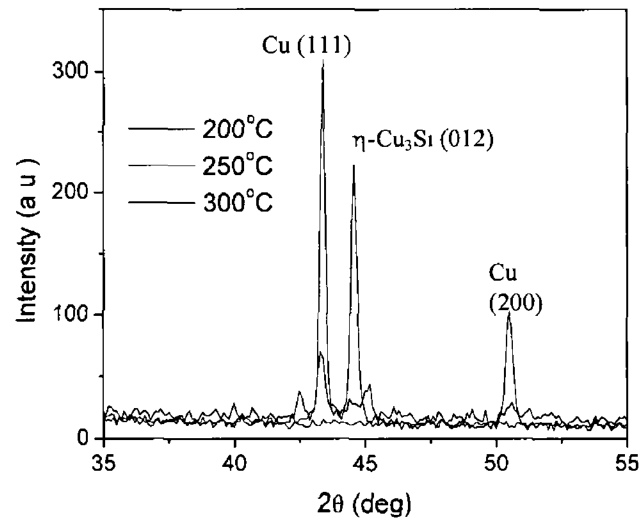

Fig 3 19 XRD for CuCl on Si samples annealed at 200°C, 250°C and 300°C

We see no Cu peaks in the samples annealed at 200°C; however Cu peaks were evident in XRD for samples annealed at or above 250°C. These Cu peaks increase in intensity as the annealing temperature and/or annealing time is increased. Solid phase re-growth of γ-CuCl on silicon substrates will therefore not be possible in a nitrogen atmosphere and annealing above 200°C results in a decomposition of the CuCl film. Sasai *et al.* [180] detected metallic Cu peaks in the X-ray diffraction pattern of CuCl nanocrystal-doped glass films annealed at 250°C, indicating that a decomposition of CuCl may also occur without reaction with Si.

Energy dispersive x-ray microanalysis was used to confirm the above conclusion. For an unannealed sample, the characteristic x-ray lines of Cu and Cl are clearly identified in the typical spectrum shown in fig. 3.20.

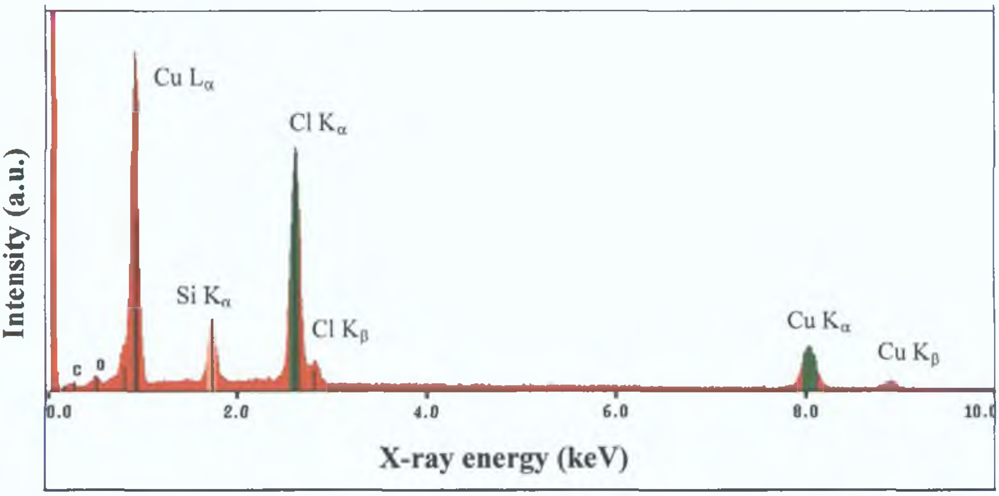

Fig 3.20 EDX spectrum of a CuCl thin film on Si. (Accelerating voltage= 15keV, Probe Current = 600pA)

There is also evidence of a Si K_α x-ray signal from the Si substrate. Two small peaks occur indicating the presence of carbon and oxygen. The carbon is most likely due to surface contamination of the sample. Oxygen may also come from a surface contamination or it is possible that a small amount of water has already been absorbed by the sample. X-ray microanalysis was then performed on a similar sample that had been annealed at 350°C for 10 seconds in nitrogen gas.

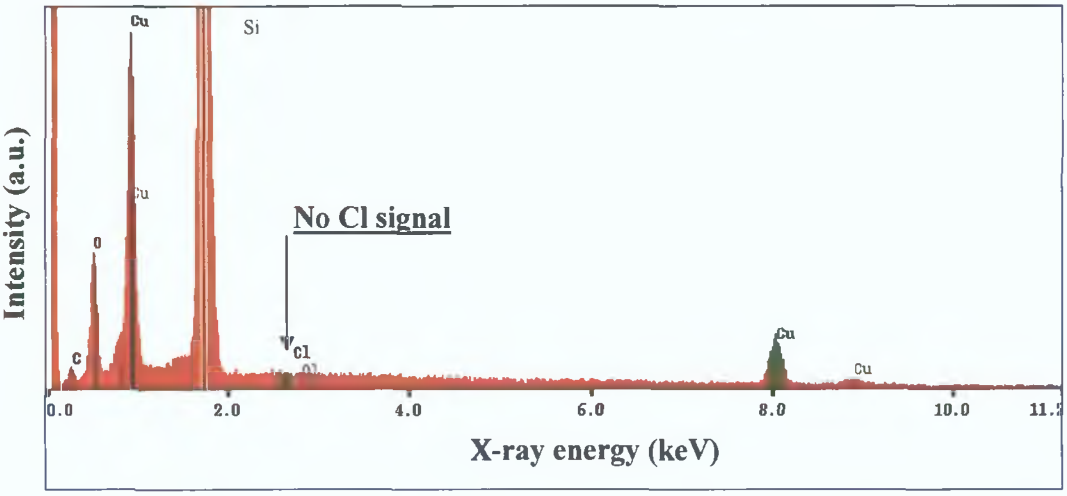

Fig. 3.21 EDX spectrum of a CuCl thin film on Si after anneal to 350°C (Accelerating voltage= 15keV, Probe Current = 600pA)

As expected there is no characteristic Cl x-ray signal for this sample as the Cl has escaped in the form of $SiCl_4$ gas formed by the reaction of Si and CuCl. The Cu signal remains reasonably strong, but the Si signal is relatively larger than before, most likely due to the creation of pinholes in the film during the reaction. There is a noticeable increase in the oxygen signal. This is consistent with the assumed presence of CuO_x peaks in the XRD pattern.

Micro-Raman spectroscopy was used to examine the changes in CuCl thin films as a function of anneal temperature.

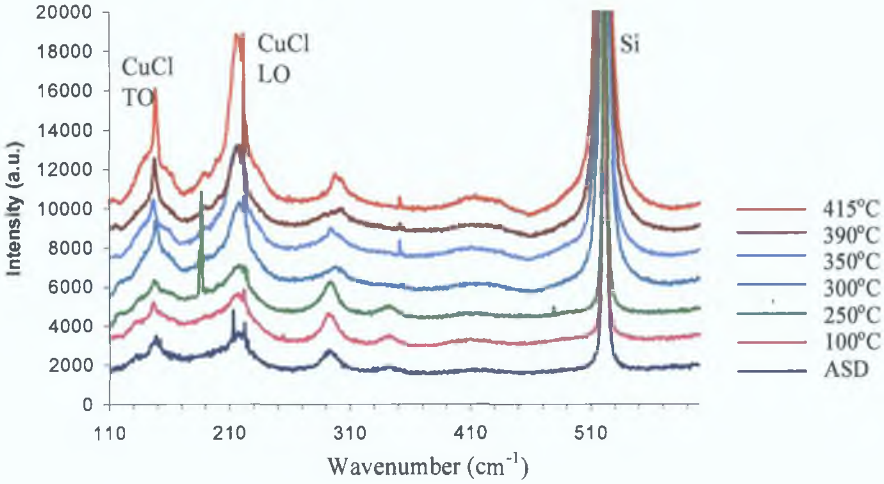

Fig. 3.22 Micro-Raman Spectra of CuCl on p-Si (100) as deposited and annealed at various temperatures

As the annealing temperature is increased we see a narrowing of the CuCl TO and LO modes. The reduced FWHM indicates an improving CuCl crystallinity. However we have seen from other techniques that the CuCl film is being degraded at higher temperature (~250°C) due to a reaction with Si so this is unlikely. As the annealing temperature is increased, the peak at ~ 294cm^{-1} shifts to higher wavenumbers. For the sample annealed at 415°C this peak appears at ~ 303cm^{-1} and is therefore most likely due to the Si-Si mode occurring at this position and not from the CuCl. The broad peak at ~ 338cm^{-1} vanishes completely for the samples annealed at 300°C and above and a new broad band centred at ~ 420cm^{-1} appears. The reaction of CuCl and Si results in the release of $SiCl_4$ gas. The disappearance of the modes at 294cm^{-1} and 338cm^{-1} indicates that these vibrations may result from a Si-Cl bond at the interface, which is broken by annealing above 250°C. The CuCl on Si sample annealed to 415°C is compared to the spectrum of a single-crystal Cu metal sample in fig. 3.23 below.

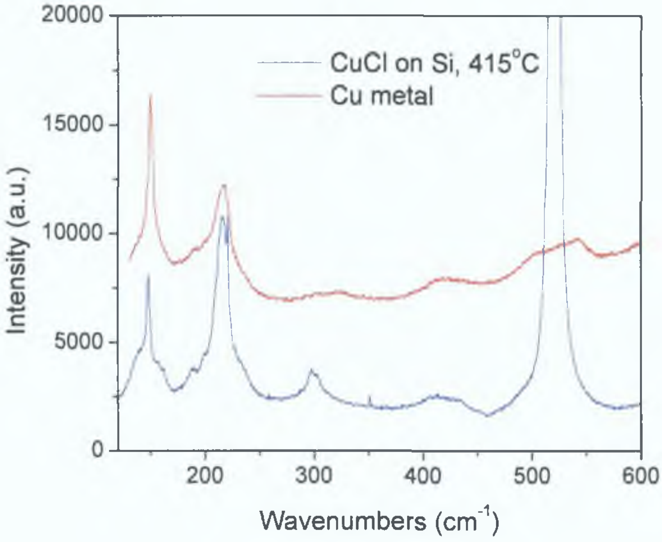

Fig. 3.23 Micro-Raman Spectra of CuCl on p-Si (100) annealed to 415°C, compared to a spectra of Cu metal

The CuCl TO and LO modes occur in the same position as the modes of a Cu sample. It is clearly seen that the sharpening of the CuCl modes after anneal is in fact due to the presence of Cu in the sample. The broad band appearing at ~ 420cm^{-1} may also be attributed to a Cu vibrational mode. Thus the micro-Raman data are consistent with the XRD and EDX results.

3.4 Degradation of CuCl

One challenge associated with the use of CuCl is that it is sensitive to moist air. Under the influence of light and moisture, hydrated oxyhalides of Cu^{++} are formed. This reaction can be easily recognised by a colour change in CuCl associated with the presence of the greenish colour Cu^{++} ions. In fig. 3.2 a small peak in the diffraction pattern of CuCl powder at a Bragg angle of ~ 16^0 was attributed to the presence of Cu(OH)Cl formed by the reaction of CuCl with moist air. If a CuCl thin film (on glass or Si substrate) is exposed to normal laboratory air conditions it is observed that the film changes from transparent to a greenish colour and a complete change occurs in the XRD pattern. The XRD diffraction pattern of a CuCl thin film on glass was measured immediately after deposition and again two weeks later. The resulting XRD spectrum is shown if fig. 3.24. It can be clearly seen that a complete recrystallisation of the CuCl thin film has taken place. The spectrum is dominated by an intense peak at 2θ ≈16.28°, which is attributed to the (100) reflection of Cu(OH)Cl formed by the reaction of CuCl with moist air. This is consistent with reports by other authors [163].

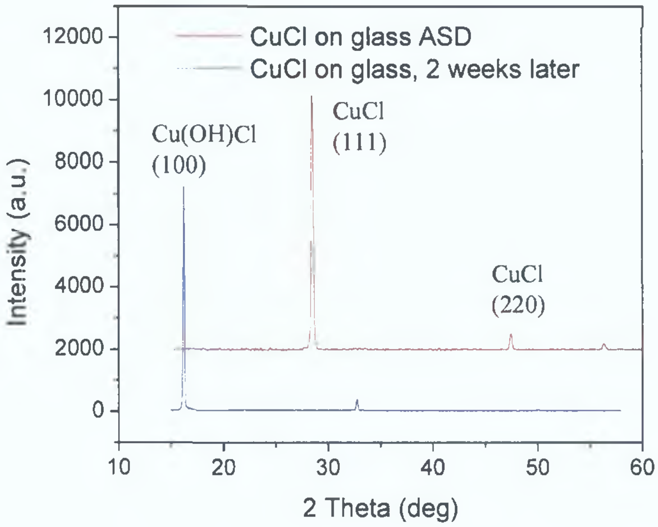

Fig. 3.24 XRD pattern of CuCl on a glass substrate as deposited (ASD) and after being exposed to air for two weeks

Suitable storage conditions are therefore necessary to prolong the lifetime of uncapped CuCl samples and a protective layer is needed to prevent this reaction. The rate of degradation of the film was not constant on all samples or substrates, but appears to occur most rapidly for samples deposited on glass. The surface structure of the sample also changes. The appearance of a series of small fractal growths on the sample coincides with the appearance of the Cu(OH)Cl peak in the XRD scan.

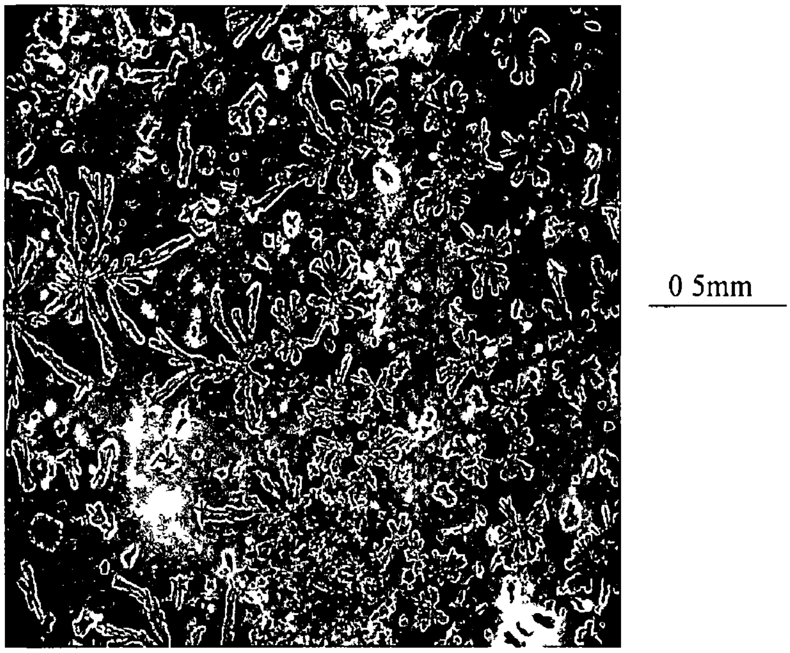

Fig 3 25 Optical micrograph of CuCl thin film on glass one day after evaporation (magnification x 50)

In one case the water intake seems to have been accelerated by the presence of pinholes in the sample and large fractal growth spread across the entire sample within a few days of evaporation

Fig 3 26 Optical micrograph of CuCl thin film on glass two days after evaporation (magnification x 50)

An EDX spectrum was taken of a ~ 500nm CuCl thin film on Si after exposure to air for one month and a large signal due to the presence of oxygen can be clearly detected.

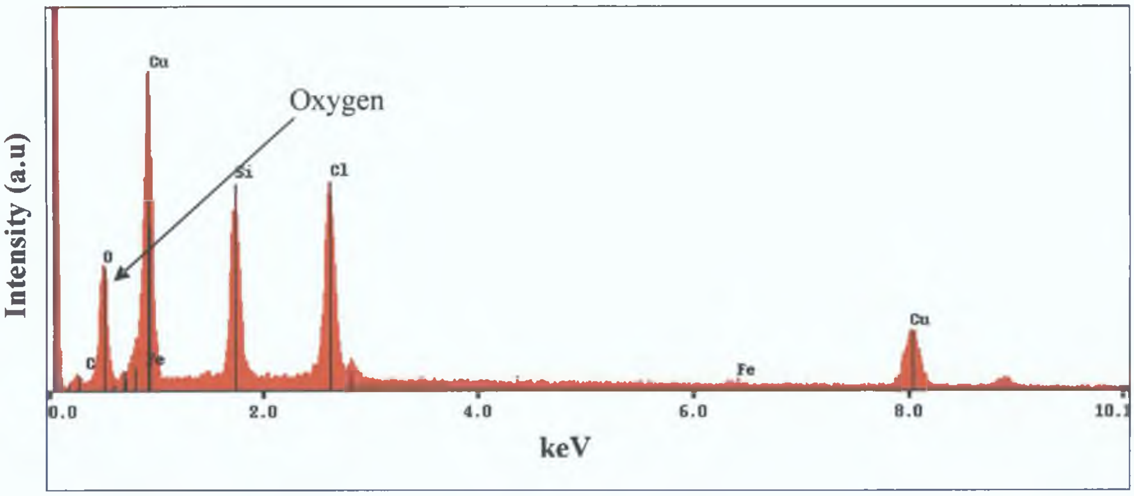

Fig. 3.27 EDX spectrum of a CuCl thin film on Si after exposure to air for one month (Accelerating voltage= 15keV, Probe Current = 800pA)

If compared to the EDX spectrum of a typical fresh sample (fig. 3.20) it is seen that the relative intensity of the oxygen peak compared to the Cu and Cl signals is much increased. It is also worth noting that unlike the spectrum of the overheated sample (fig. 3.21) the Cl signal remains strong after exposure to air. This is consistent with the conclusion that the peak seen in XRD after reaction with moist air is due to the presence of Cu(OH)Cl.

On a temporary basis, this problem is avoided by storing the samples in a vacuum desiccator using silica gel desiccant. This prolongs the sample lifetime sufficiently to take the desired measurements. The long-term solution is to deposit a capping layer over the CuCl creating a hermetic seal This is essential for demonstrating the feasibility of CuCl as a working light-emitting device material

3.5 CuCl Capping Layer

There are a number of requirements for a CuCl capping layer which include,

- It must create a barrier between CuCl and the air to prevent the intake of moisture
- It must be transparent in the region of light emission of CuCl (~ 387nm)
- It should not react with CuCl
- It must be an insulator
- The deposition/curing temperature has to be below 250°C to prevent a reaction between CuCl and Si
- Ideally it should be depositable as a thin film (<500nm)

Three main insulators were investigated in our laboratory by Francis Olabanji Lucas, (1) SiO_2 deposited by plasma enhanced chemical vapour deposition (PECVD), (2) Organic polysilsesquioxane (PSSQ) spin-on glass-based dielectric and (3) Cyclo olefin copolymer (COC) -based dielectric Fourier Transform Infra-Red (FTIR) and UV-Visible analysis has shown that both PSSQ and COC spin-coated (or dip coated) liquid glass layers are an effective means of sealing the CuCl system for at least one month PECVD SiO_2, slowed the degradation rate but did not eliminate oxidation Details of this encapsulation study can be found in reference [181]

Chapter 4

Optical Properties of CuCl

4.1 UV-Visible Spectroscopy

The optical properties of the polycrystalline CuCl thin films on glass were investigated by using UV- Visible (UV-VIS) spectroscopy The spectra were first recorded for a standard glass substrate, which was then subtracted from the result for the CuCl thin film deposited on glass, in order to show only the contribution resulting from the CuCl There was no difference in the spectra of films grown from CuCl powders of 97% and 99 999% purity, respectively In fig 4 1, the room temperature UV-VIS absorption spectrum of a CuCl thin film on a glass substrate is shown

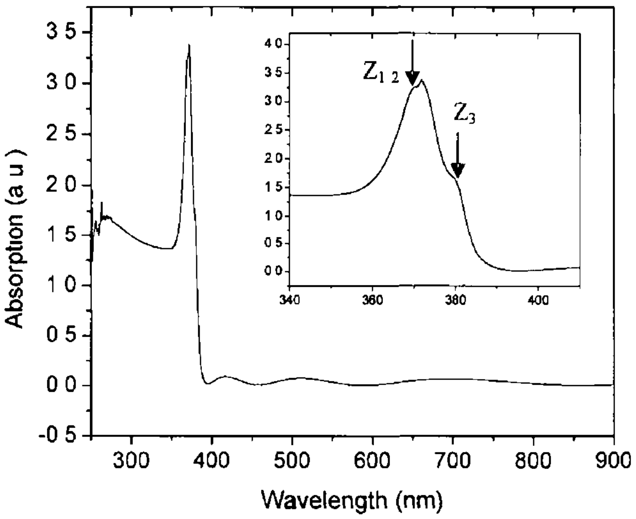

Fig 4 1 UV-VIS absorption spectrum of CuCl on glass

The spectrum is dominated by a strong absorption peak at ~ 372nm (3 34eV) followed by a rather flat absorption from 400-900nm As can be clearly seen in the inset, the main peak results from the contribution of both high and low energy excitonic bands, historically called the $Z_{1,2}$ and Z_3 excitons, respectively. The $Z_{1,2}$ and Z_3 excitons originate from the coupling of the lowest conduction band state Γ_6 to both the uppermost valence band holes in Γ_8 ($Z_{1,2}$) and Γ_7 (Z_3), respectively [79,90]. The energy values of 3.34eV (λ ~ 372nm) for the $Z_{1,2}$ exciton, and a small shoulder at 3.27eV (λ ~ 380nm) corresponding to the Z_3 exciton, are in close agreement with values reported by other authors for room temperature CuCl absorption measurements [79,84]. These peak assignments were also confirmed experimentally by performing a low temperature reflectance measurement[1] with a resolution ~ 0.1meV, shown in fig 4.2 below. Details of the experimental set-up of the reflectivity system can be found in references [182,183].

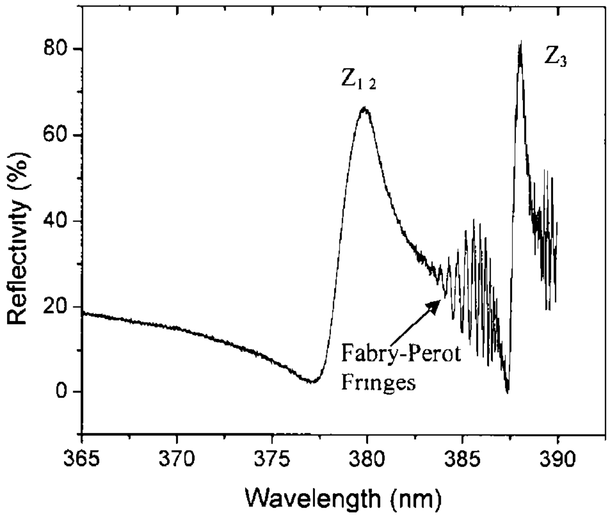

Fig. 4.2 Reflectance of CuCl on Si (100) at 20K

In the reflectance spectrum we see a clear separation of the $Z_{1,2}$ and Z_3 exciton peaks. To a good approximation, the transverse energies are at the maxima of the reflectance anomalies, and the longitudinal energies at the minima. The transverse energies of the

---

[1] The reflectance measurement was performed by James Fryar in the School of Physical Sciences in Dublin City University

$Z_{1,2}$ and Z_3 excitons are 3.2726eV (379.85nm) and 3.2024eV (388.19nm), respectively. The oscillations occurring on the low energy side of the $Z_{1,2}$ exciton peak, labeled as Fabry-Perot fringes on the plot are due to multiple reflections from the CuCl thin film which has non-uniform thickness. These results are consistent with published data on single crystal CuCl [184] although the single crystal CuCl spectra have no Fabry-Perot fringes.

The optical transmittance versus wavelength spectrum of a CuCl thin film on glass in the range of 250nm – 900nm is shown in fig. 4.3.

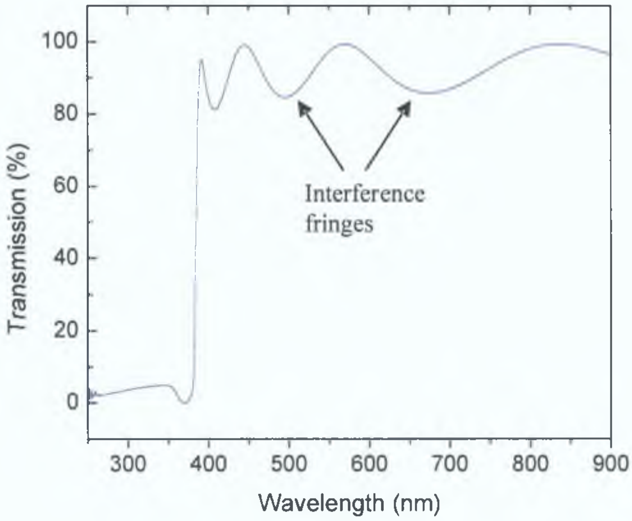

Fig. 4.3 Transmission spectrum of CuCl on glass

The transmission of CuCl is greater than 80% in the wavelength range of 400nm – 900nm, and as high as 99.0% at the peak of the interference fringe at 446nm. The interference fringe pattern in the transmission spectrum indicates that the film surface was highly reflecting and there was not much scattering or absorption loss in the film [185]. Beyond the absorption edge in the UV region, transmittance was reduced to approximately zero.

To assess the rate of optical degradation of the uncapped CuCl thin film, UV-VIS spectra were recorded over a period of one month from the day of vacuum deposition. In fig. 4.4 four spectra which illustrate the trend seen are plotted.

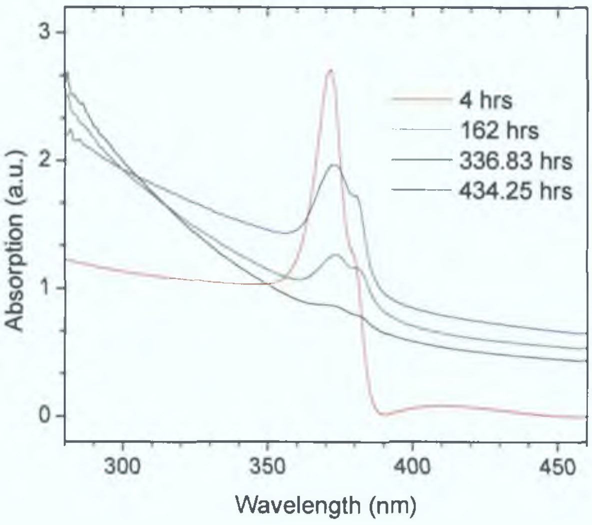

Fig. 4.4 UV-VIS absorption spectra of CuCl on glass as a function of time

Initially, a sharp $Z_{1,2}$ and the broad shoulder of the Z_3 exciton peaks are clearly seen. After approximately one week (162 hours), the intensity of the main $Z_{1,2}$ absorption peak has nearly halved while the intensity of the Z_3 exciton peak is only slightly reduced relative to the background absorption level at 450nm. This is clearly illustrated in fig. 4.5 below in which the intensity ratio of the $Z_{1,2}$ to Z_3 exciton absorption peaks is plotted as a function of time on a log scale. Following exposure to atmospheric conditions for approximately two weeks (337 hours) the absorption intensities of both the $Z_{1,2}$ and Z_3 exciton peaks have dramatically decreased indicating that the optical quality of the CuCl thin film has been severely compromised by exposure to the atmosphere. Eventually the only evidence remaining of the CuCl excitonic behaviour is a slight increase in the absorption at the energy of the exciton peaks.

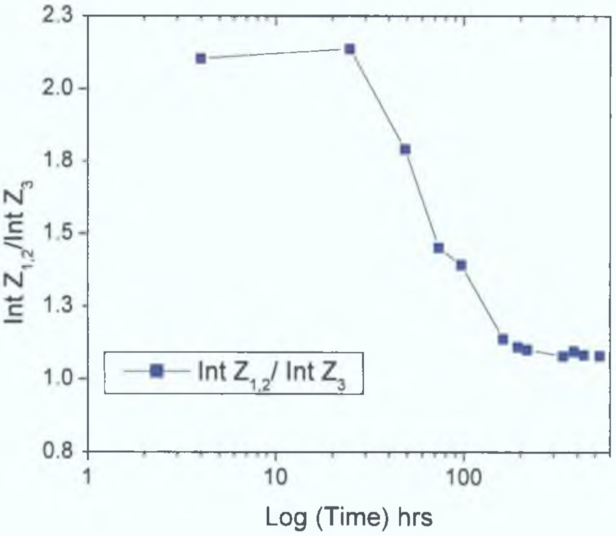

Fig. 4.5 Intensity ratio of the $Z_{1,2}$ and Z_3 CuCl absorption peaks as a function of time

By examining the intensity ratio of the $Z_{1,2}$ and Z_3 exciton peaks, we see that initially the $Z_{1,2}$ absorption peak is more than twice as intense as the Z_3 absorption peak but after approximately one day the intensity ratio begins to fall indicating that the $Z_{1,2}$ exciton degrades at a faster rate than the Z_3 exciton on exposure to atmospheric conditions. After approximately one week has passed, the intensity ratio begins to level out and then remains approximately constant for the remainder of the time studied.

The transmission spectra of the CuCl on glass thin films were also monitored over the same period of time as the absorption spectra. A significant drop in the transmission is detected from 89% at 500nm for the fresh film to 68% at 500nm for the same film two days later. The interference fringes have also vanished by this time indicating that the quality of the film surface is poorer due to degradation. It is interesting to note that the minimum transmission value of 27% at 500nm was recorded after 162 hours (~one week). After this point the transmission began to slowly increase again to a value of 41% at 500nm after 434 hours (~18 days).

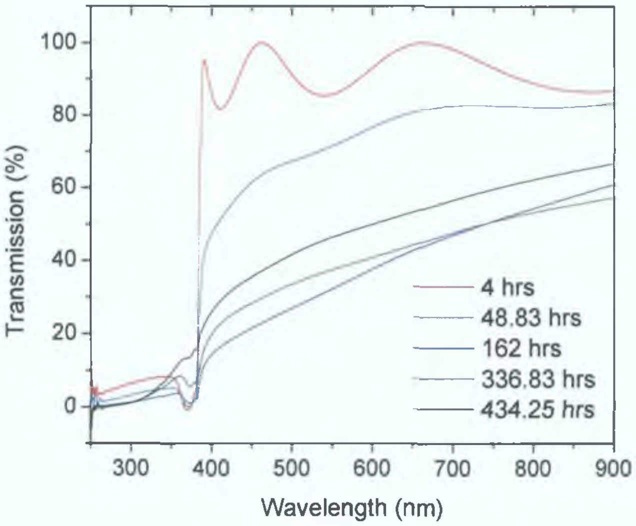

Fig. 4.6 UV-VIS transmission spectrum of CuCl on glass as a function of time

It is known that the degradation of CuCl is a process involving the formation of a number of compounds such as $CuCl_2$ and Cu(OH)Cl [163]. A degradation study of CuCl performed in our laboratory by Gomathi Natarajan using Fourier transform infra-red spectroscopy (FTIR) showed that the first indication of CuCl oxidation is the presence of a new peak in the FTIR spectrum which is attributed to an OH bond. Therefore, one possible explanation for this behaviour is that the formation of Cu(OH)Cl proceeds first, followed by the formation of the $CuCl_2$ and therefore the ratio of each compound in the probed volume varies with time leading to a change in the transmission properties of the film. A more detailed study of this phenomenon was not pursued as it was not directly related to the key aims of this research.

4.2 Photoluminescence[1]

We have optically characterised the CuCl on Si thin films using power and temperature dependent photoluminescence The XRD results presented in chapter 3 show that the crystalline orientation of the CuCl thin film is somewhat dependent on the orientation of the Si substrate Therefore in order to assess if this difference in microstructure impacts on the optical properties of CuCl, PL measurements were performed on CuCl samples deposited on both Si (111) and Si (100) substrates Samples which are directly compared were prepared in the same evaporation run In fig 4 7, the room temperature PL emission of a 500nm CuCl thin film, deposited from CuCl powder of 97% purity is shown for Si (100) and Si (111) oriented substrates, respectively

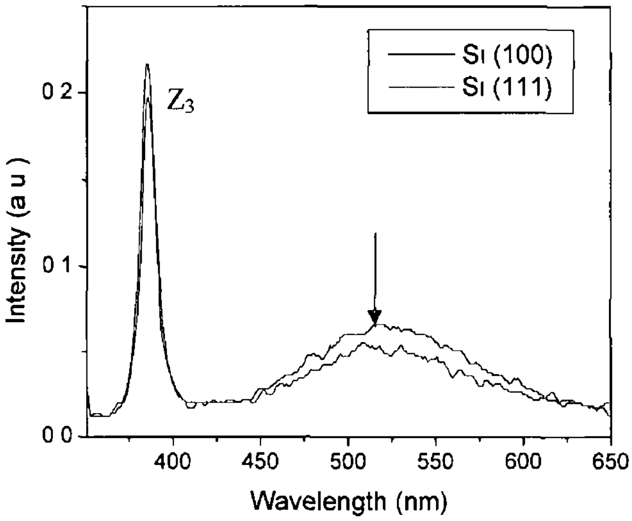

Fig 4 7 Room temperature PL spectra of CuCl (97%) on Si (100) and Si (111) substrates

---

[1] Photoluminescence measurements were performed in the Semiconductor Photonics Group at Trinity College, Dublin The work was started by Dr Miguel Martinez-Rosas but mainly performed by Dr Anirban Mitra Further details can be found in reference [189]

The main peak at 386.4nm is assigned to the Z_3 free exciton emission in agreement with reports by other authors [87,90]. There is no significant difference in the room temperature PL of CuCl deposited on Si substrates of (111) and (100) surface orientations, respectively. Another feature of the PL spectra is a broad band centred at ~ 520nm. To investigate the source of this emission, the PL spectrum of a bare Si substrate was also measured under the same excitation conditions and compared to the PL spectra of CuCl (fig. 4.8)

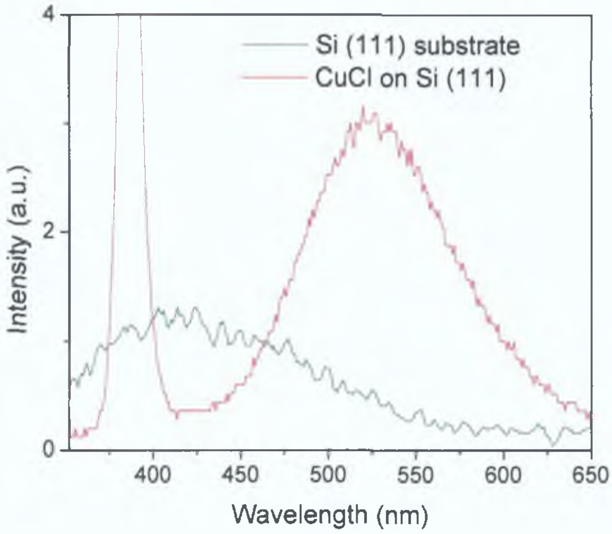

Fig. 4.8 Room temperature PL spectra of CuCl (97%) on Si (111) and uncoated Si (111) substrate, respectively.

A broad peak from the Si substrate is found at ~ 420nm. By comparing the two plots in fig.4.8, we see that this is clearly a different emission to that of the CuCl film, detected at ~520nm. The source of this broad CuCl band was further investigated using cathodoluminescence and will be discussed in the next section.

PL spectra for a CuCl on Si (111) sample, deposited from CuCl powder of 97% purity, measured in the temperature range of 10K to 240K are shown in fig. 4.9.

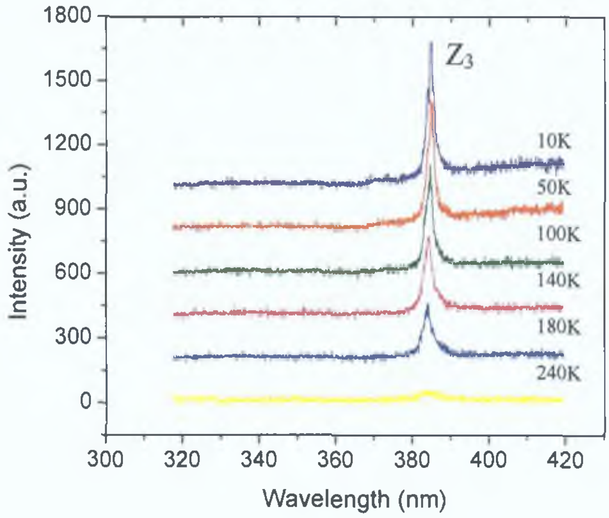

Fig. 4.9 PL spectra of CuCl (97%) on Si (111) as a function of temperature. (An intensity offset has been applied for clarity.)

The spectrum is dominated by one main peak which occurs at ~ 3.23eV (385.8 nm) at 10K. This is the Z_3 free exciton peak. As expected due to thermal broadening, the intensity of the peak decreases as the temperature is increased and the FWHM of the Z_3 peak increases from a minimum value of 2.17 nm at 10K to 3.40 nm at 180K. This line-width broadening as a function of increasing temperature is due to the interaction between the excitons and the optical and acoustic phonons [189].

The temperature dependent PL spectra of a CuCl on Si (100) sample, deposited from CuCl powder of 97% purity, are shown in fig. 4.10.

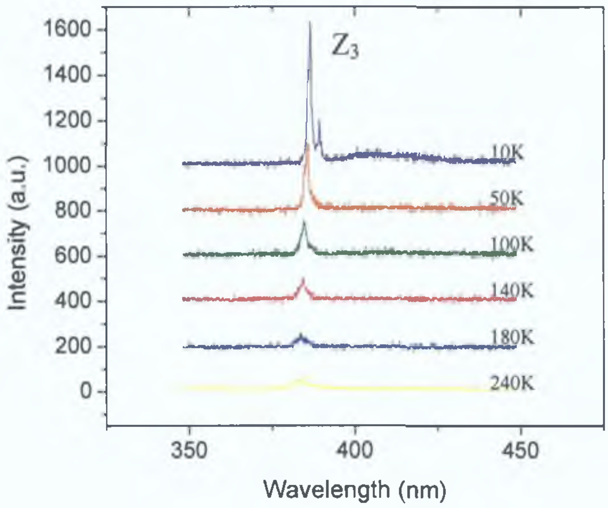

Fig. 4.10 PL spectra of CuCl (97%) on Si (100) as a function of temperature

The behaviour of the Z_3 exciton is similar to the sample grown on Si (111). However in this case, two peaks are evident in the spectrum taken at 10K. This is clearly seen in fig. 4.11 below.

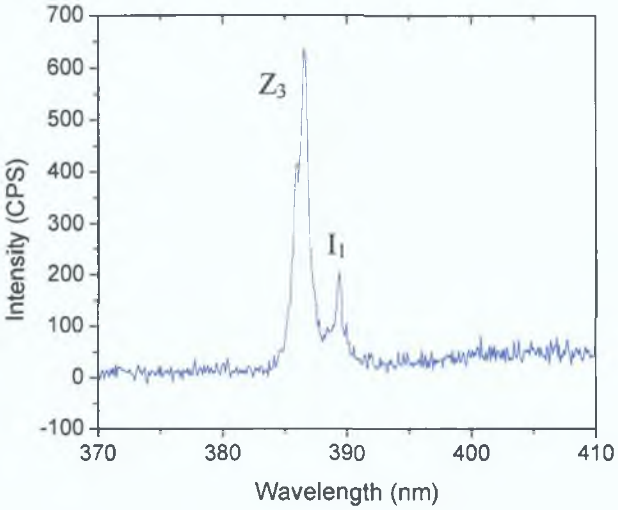

Fig. 4.11 PL spectra of CuCl (97%) on Si (100) at 10K

The main peak which occurs at ~ 3 208eV (387 51 nm) is the Z_3 free exciton peak On the low energy side of the free exciton peak a second peak occurs at ~ 3 184eV (390 43 nm) This is attributed to an emission from an exciton bound to an impurity [90,186], which has been called the I_1 bound exciton The impurity has previously been identified as a neutral acceptor, possibly a Cu vacancy [187] At 50K only the Z_3 exciton peak is visible and has shifted slightly to an energy of ~3 221eV The disappearance of the I_1 bound exciton at 50K is considered to be due to the thermal dissociation of the bound state as the binding energy of the bound exciton has been reported to be ~22meV [90] At 240K we see a broad Z_3 exciton peak centred at ~3 238eV The observed shift in position of the Z_3 exciton with increasing temperature agrees quite well with the values reported by other authors [88]

Although exciton states represent the lowest-energy states for electron-hole pairs, excitons are formed easily only in the purest materials and at low temperatures In less pure or less perfect crystals, local fields tend to break up the exciton into free carriers [188] The presence of excitonic emissions in the CuCl thin films indicates that the crystals are at least of a reasonable quality In an attempt to further improve the films, CuCl samples were also grown from high purity (99 999%) CuCl powder This powder was shipped under Argon in a sealed quartz ampoule and stored in a vacuum desiccator after breaking the ampoule In this way the degradation of the powder due to Cu oxidation forming $CuCl_2$ and Cu(OH)Cl was minimised

A PL spectrum measured at 10K for a CuCl on Si (100) sample, grown from CuCl powder of 99 999% purity, is shown in fig 4 10 A similar spectrum was obtained for CuCl on Si (111) as shown in the inset Four peaks are evident in the spectrum The peak which occurs at ~ 3.212 eV (λ ~ 387nm) is the Z_3 free exciton peak. Due to the large binding energy of the free exciton (~ 190 meV), this peak was also clearly evident in room temperature PL measurements at an energy E = 3.236 eV (λ ~ 384nm) shown in fig.4.13.

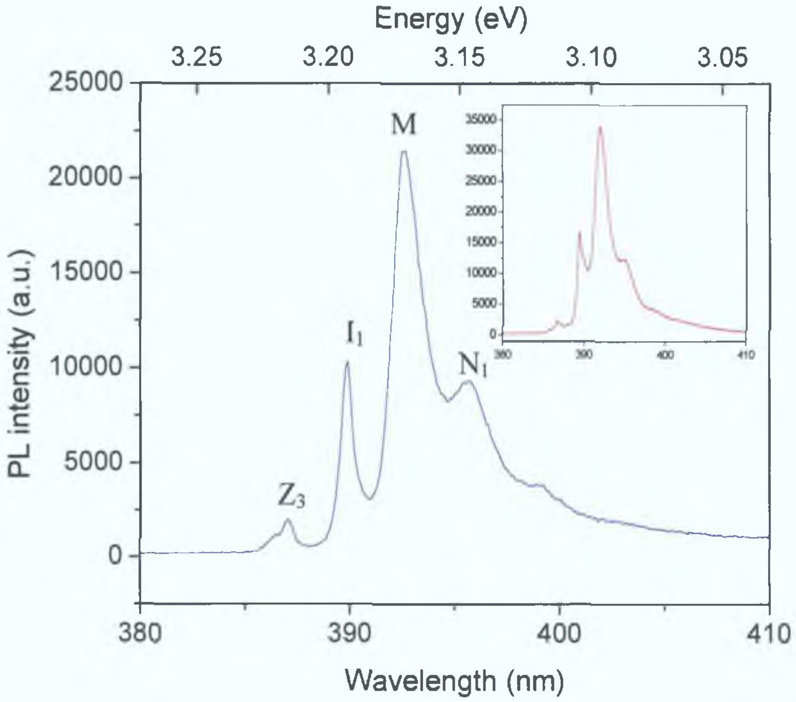

Fig. 4.12 Photoluminescence spectrum of CuCl on Si (100) at 10K. Inset PL spectrum of CuCl on Si (111)

On the low energy side of the free exciton, the I_1 bound exciton peak occurs at ~ 3.189 eV (λ ~ 389.8nm). The energies for the free and bound exciton peaks agree exactly with previous reported measurements for CuCl bulk crystal at 8 K [87] and thin films on Al_2O_3 [90]. A third peak, which appears at 3.166eV (λ ~ 392.7nm) is identified as a free biexciton M. The free biexciton results from exciton-exciton collisions resulting in the formation of an excitonic molecule (so called biexciton). It is known that emission from both the transverse, M_T, and longitudinal, M_L, biexcitons occur at 3.171 and 3.165 eV, respectively [186]. However as the experimental resolution was 0.3nm, we were unable to resolve two peaks. It should be noted that high energy excitation such as at 244 nm (5.09 eV) enhances the bi-excitonic features in the spectrum. At 3.141 eV (λ ~ 395.8 nm) a fourth peak labelled N_1 is evident, and likely originates from a biexciton bound to an impurity. Similar to the I_1 bound exciton, the most probable candidate for the impurity is considered to be a neutral acceptor [90]. These peak assignments were further confirmed by performing power dependent PL measurements, undertaken at 10K [189]

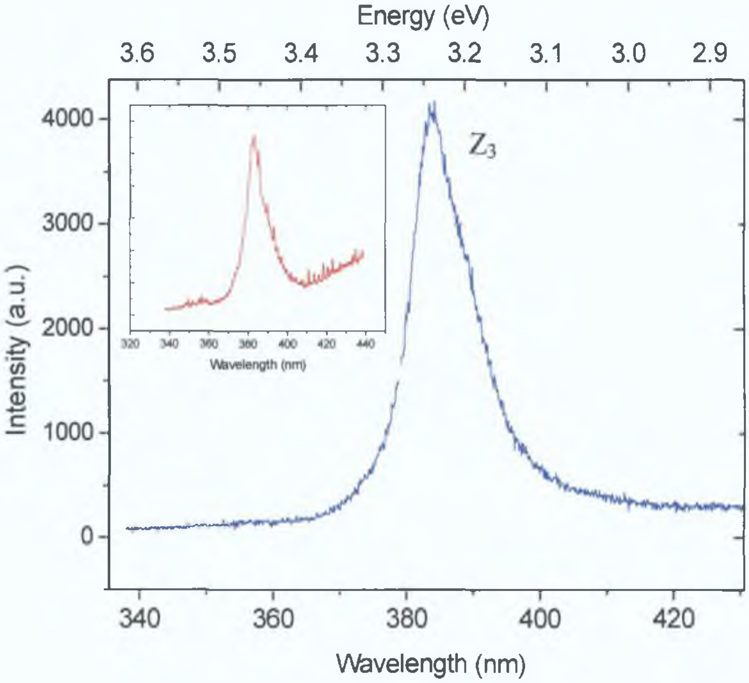

Fig. 4.13 Room temperature PL spectra of CuCl on Si (100). Inset PL spectrum of CuCl on Si (111)

The room temperature spectra (shown above) are dominated by the Z_3 free exciton peak. The FWHM determined by fitting with a Gaussian curve was 10.37nm (87meV) for CuCl on Si (100) and 10.64nm (93meV) for CuCl on Si (111). This compares well to the value of 86meV reported for room temperature PL emission in ZnO [190], indicating the high optical quality of the CuCl thin films. It is slightly broader than typical values reported for room temperature UV emission in GaN e.g. 70meV for GaN on Si (111) [191].

A small shoulder appearing on the high energy side of the Z_3 peak at 10K is identified as the $Z_{1,2}$ free exciton peak. In a spectrum taken at 240K the two peaks are clearly defined at 3.238 eV (Z_3) and 3.318 eV ($Z_{1,2}$) as shown in fig. 4.14.

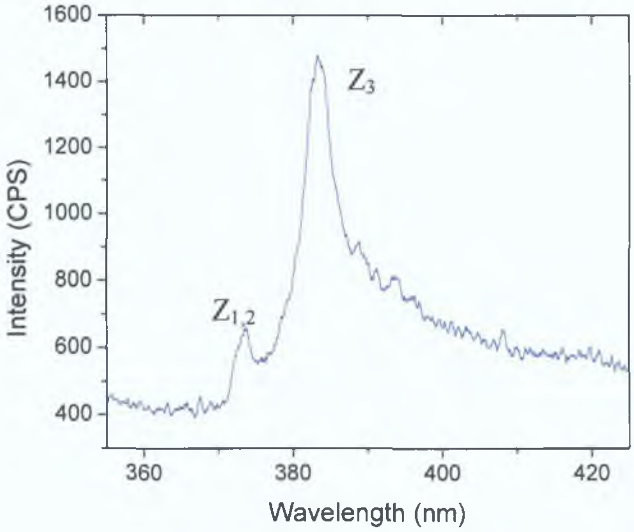

Fig. 4.14 PL spectrum of 500nm CuCl film on Si (100) at 240 K showing $Z_{1,2}$ exciton peak.

It is considered that the bound biexciton PL results from the optical transition from the bound biexciton state to the bound exciton state. Therefore the binding energy of the bound biexciton (E_{bX}^{b}) can be estimated from the measured PL energies according to $E_{bX}^{b} = E_X - E_{bX}$, where E_X and E_{bX} are free exciton and bound exciton energies. This scheme, developed by Nakayama *et al.* [90] is illustrated in fig. 4.13. Based on this principle, it is also possible to estimate the binding energies of the free biexciton (E^b_{XX}) and the bound biexciton (E^b_{bXX}) from the following equations [90,92,109]

$$E^b_{XX} = E_X - E_{XX}$$

$$E^b_{bXX} = 2E_X - E_{bXX} - E_{bX} - E^b_{XX}$$

where E_X (3 203 eV), E_{XX} (3 159 eV), E_{bX} (3 181 eV) and E_{bXX} (3 134 eV) are free exciton, biexciton, bound exciton and bound biexciton energies respectively taken from the PL spectrum at 10 K, as shown in fig 4 12

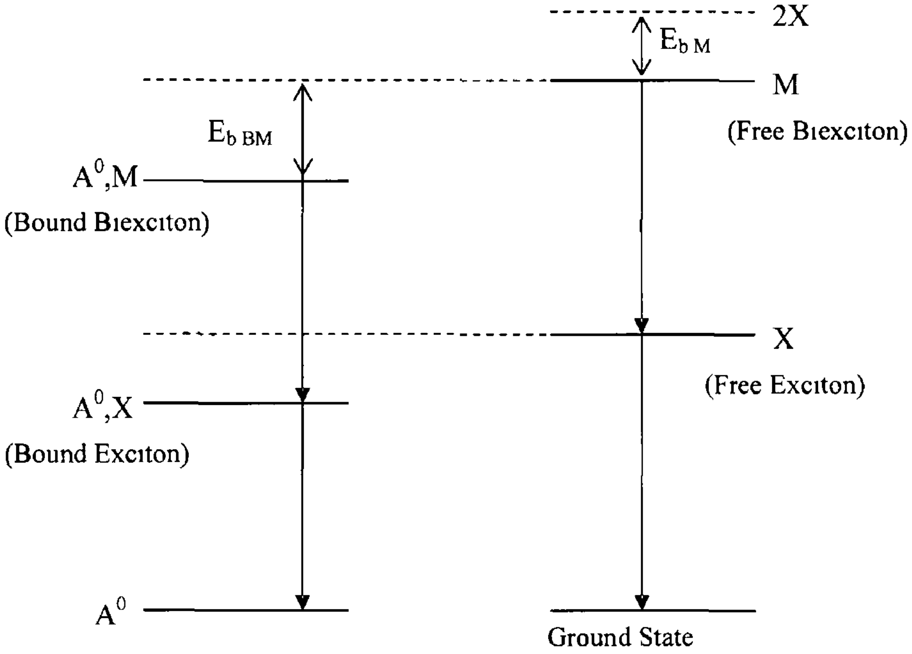

Fig 4 15 Nakayama energy scheme [86] for calculation of excitonic binding energies of free states (right-hand side) and bound states (left-hand side) M, X and A^0 denote the free biexciton, Z_3 free exciton and neutral acceptor, respectively

The estimated binding energies are 22±2 meV for the bound exciton, 44±2 meV for the free biexciton and 47±2 meV for the bound biexciton [189] Values for the bound exciton and bound biexciton are in exact agreement with previously reported values for vacuum deposited CuCl thin film on Al_2O_3 [90]. However the free biexciton binding energy for the CuCl on Si system is found to be approximately 10 meV higher than that reported for the CuCl thin film on Al_2O_3. The extracted values are also in good agreement with the earlier literature reports for single crystal CuCl [192].

We have also studied the temperature dependence of the PL spectra of CuCl thin films on Si substrates grown from CuCl powder of 99.999% purity over the temperature range 10 K to room temperature. Again similar behavior is observed for both the Si (100) and Si (111) substrates.

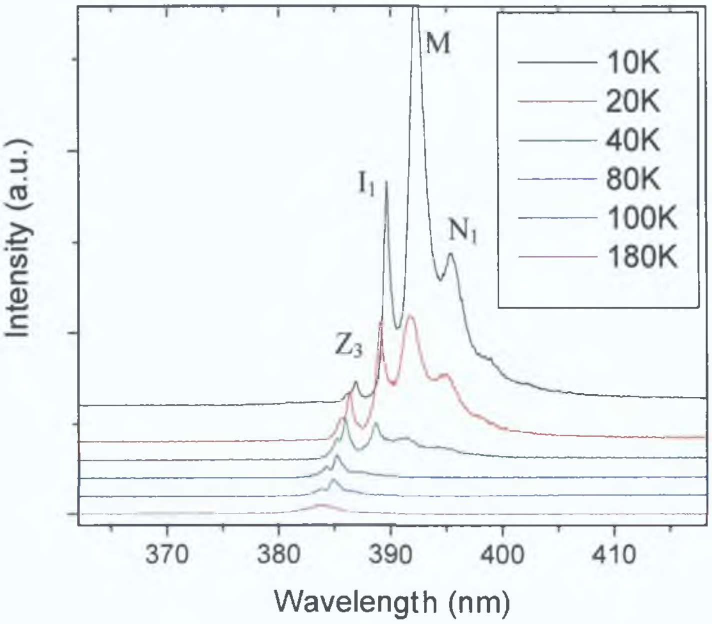

Fig. 4.16 PL spectra of CuCl (99.999%) on Si (100) as a function of temperature. (An intensity offset has been applied for clarity.)

Fig. 4.16 shows the temperature dependence of the PL spectra for high purity CuCl thin films on Si (100). For this sample, the peak intensities of the free biexciton (M) and bound bi-exciton (N_1) decrease more rapidly with increasing temperature in comparison to the free exciton (Z_3) and bound exciton (I_1). At temperatures above 80 K only the free exciton (Z_3) peak is evident. A broad feature centred at ~ 413 *nm* appears at approximately 128K, reaches a maximum intensity at 117K and disappears again below 100K as shown in fig. 4.17.

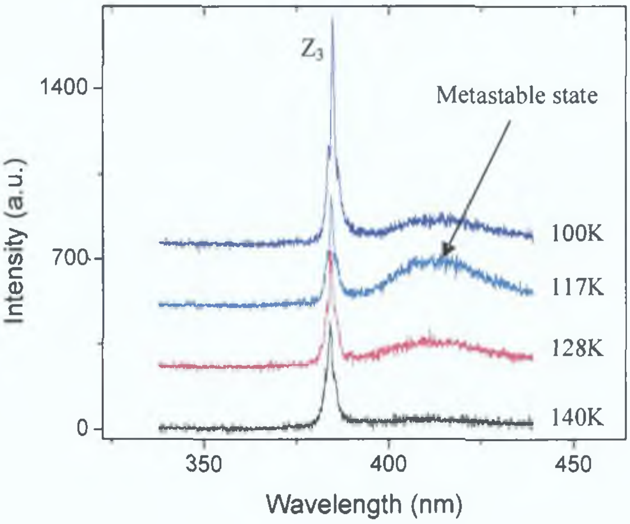

Fig. 4.17 Temperature dependent PL spectra of CuCl (99.999%) on Si (100) showing the appearance of a metastable state

Such a metastable transition has not been previously reported and may be due to the thermal dissociation of the bound states. The thermal stability of the films was investigated by Dr. Anirban Mitra through analysis of the temperature dependence of the peak intensities. The temperature dependence of the Z_3, free exciton, and M, free bi-exciton, peak intensities are presented in reference [189]. In the higher temperature region the PL intensity decreases exponentially mainly due to thermally activated non-radiative recombination mechanisms. The temperature dependence of the PL intensity can be expressed by the Arrhenius equation:

$$I_{ex}^{peak} = I_0(T = 0K)/[1 + A\exp(-E_t / kT)]$$

where A is a constant, E_i is the thermal activation energy, k is the Boltzmann constant, and T is the ambient temperature in Kelvin The thermal activation energies for the free exciton and free bi-exciton are determined to be 120±10 meV and 24 3±0 5 meV, respectively The free exciton thermal activation energy in our CuCl on silicon system is found to be less than previously reported for single crystal CuCl (150 meV) and evaporated thin film CuCl (250 meV) [87] It is also noted that the thermal activation energies for both free exciton and bi-exciton are less than their binding energies

We have clearly seen a difference in the optical properties depending on the purity of the powder which was used to deposit the CuCl film Although the film grown from 97% CuCl powder was of reasonable quality, in order to realise the formation of biexcitons, the crystal quality needs to be high enough to avoid excessive scattering by impurities and crystalline defects before association of excitons [193] As biexcitons are evident in PL measurements on films grown from CuCl powder of 99 999% purity, this indicates that they were higher quality thin films The optical properties of the CuCl films on Si substrates are similar to those previously reported for single crystal CuCl and thin films on other substrates Therefore we can conclude that the optical quality of CuCl thin films on Si substrates is not compromised in comparison with single crystal CuCl

4.3 Cathodoluminescence

The optical properties of CuCl thin films grown on p-Si (100) and p-Si (111) substrates were further investigated by using cathodoluminescence (CL) Fig 4 18 shows a room temperature CL spectrum of CuCl on p-Si (100) excited with an electron beam of 10keV and probe current of 15nA

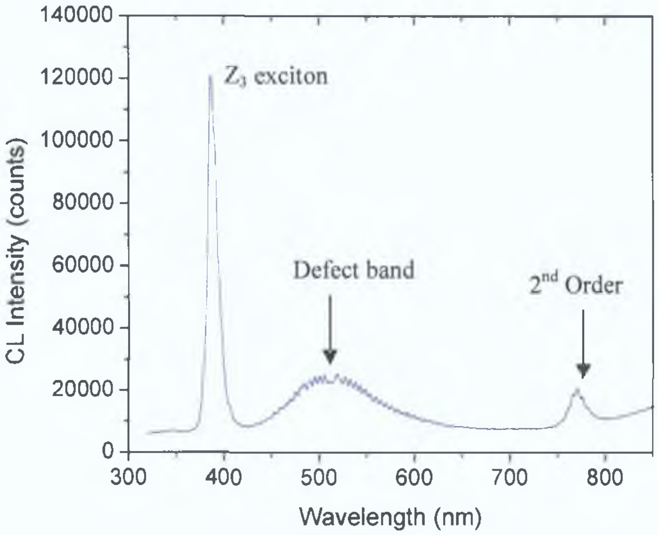

Fig. 4.18 CL spectrum of a 500nm CuCl film on p-Si (100)

The main features of the CL spectrum include a strong emission at ~387nm (3.21eV), and a broad blue-green emission band centred at ~511nm (2.43eV).The emission at 3.21eV agrees reasonably well with the values reported in the literature for the Z_3 free exciton emission [87,90]. As for the PL, room temperature excitonic emission is possible due to the large binding energy of the free exciton (~ 190 meV) in CuCl. The narrower red emission band at ~772 nm is simply the 2nd order of the excitonic peak due to the diffraction grating. Therefore the CL data will normally be displayed over a range of 300 nm – 700 nm to avoid the reproduction of 2nd order artefacts.

When performing the CL measurements it is possible to vary both the accelerating voltage and the probe current of the beam. Both parameters were investigated to find the optimum values for investigating the CL properties of CuCl thin films on Si.

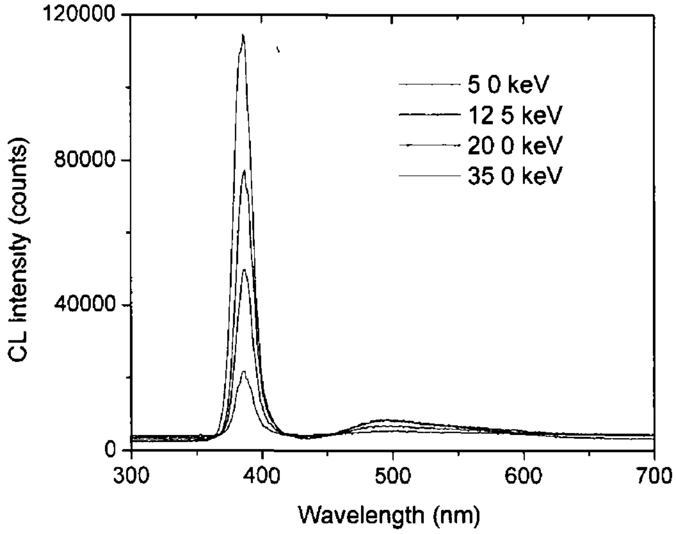

Fig 4 19 CL spectra of a 500nm CuCl film on Si as a function of higher accelerating voltage

The optimum accelerating energy depends on the thickness and density of the film being investigated as discussed in section 2 7 A selection of accelerating voltages has been chosen in fig 4 19 above to illustrate the general trend in CL intensity The interaction of the primary electron beam with the sample occurs in an excitation volume which is related to the density of the sample under investigation and the accelerating voltage For low density samples the beam penetration is approximately pear shaped It was shown in the Monte Carlo simulation in fig 2 9 that with an accelerating voltage of 5 0 keV the electron beam excited the CuCl to a penetration depth of ~ 400nm A strong CuCl excitonic peak was detected at this value A schematic diagram showing the excitation volume of the electron beam for 500nm CuCl thin film on a Si substrate is shown in fig 4 20 below for accelerating voltages of 5 keV, 12 5 keV and 2 keV, respectively

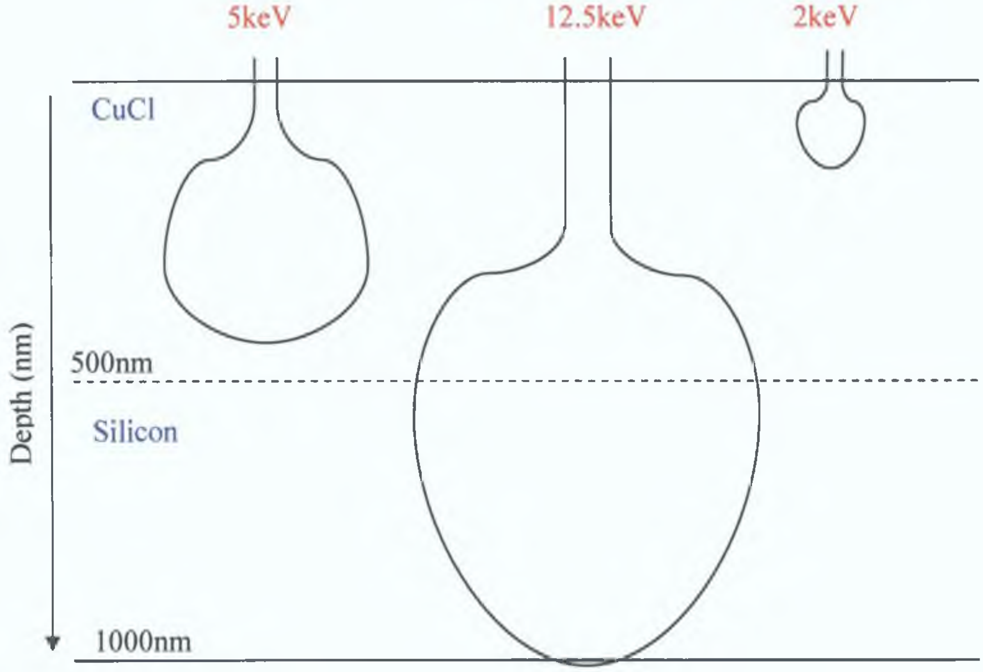

Fig. 4.20 Schematic diagram showing the penetration depth of the electron beam in CuCl as a function of accelerating voltage

Increasing the accelerating voltage above 5 keV resulted in a decrease in the excitonic peak intensity, as an increasingly larger fraction of the electrons were penetrating into the Si substrate and therefore not of use in exciting the CuCl thin film as illustrated above.

The effect of decreasing the accelerating voltage below 5 keV was also investigated. The resulting CL spectra are shown in fig. 4.21. Decreasing the accelerating voltage also resulted in a decrease in the excitonic peak intensity from 5 keV to 3.5 keV due to the slight decrease in the volume of CuCl being excited by the electron beam.

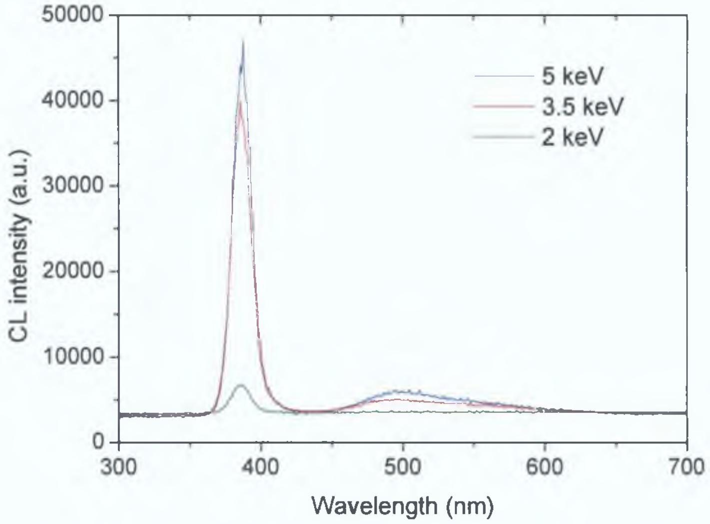

Fig. 4.21 CL spectra of a 500nm CuCl film on Si as a function of lower accelerating voltage

A further decrease in the accelerating voltage to 2 keV caused a dramatic decrease in the excitonic emission intensity as only a very small portion of the CuCl thin film (to a depth of ~ 100nm as indicated by the Monte Carlo simulation package) is being excited, as shown schematically in fig 4.20.

The probe current of the electron beam was varied in the range of 1nA to 15nA.

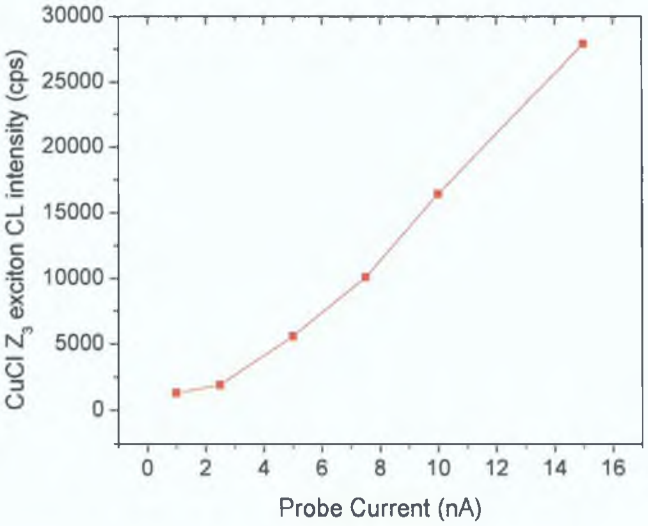

Fig. 4.22 CuCl Z_3 free exciton CL intensity as a function of Probe Current with an accelerating voltage of 5 keV

It can clearly be seen in figure 4.22, that as the probe current is increased the intensity of the CL emission also increases. This is true for both the main free exciton emission and the broad band centred at ~ 500 nm. In fig. 4.22 the value of the CL intensity at each probe current has been corrected by subtracting the background count level at 300 nm. For probe currents ranging in value from 2.5nA to 15nA an approximately linear relationship exists for the change in the CL intensity of the CuCl Z_3 free exciton as a function of probe current. The probe current was not further increased beyond 15 nA because at this relatively high value some sample damage is likely due to surface charging as CuCl is a poor semiconductor in its undoped state.

In the CL data plotted in fig.4.18, the purity of the evaporated CuCl powder was 97%. To investigate the source of the broad defect band, a sample prepared with CuCl powder of 99.999% was also examined and compared to that of the CuCl 97%.

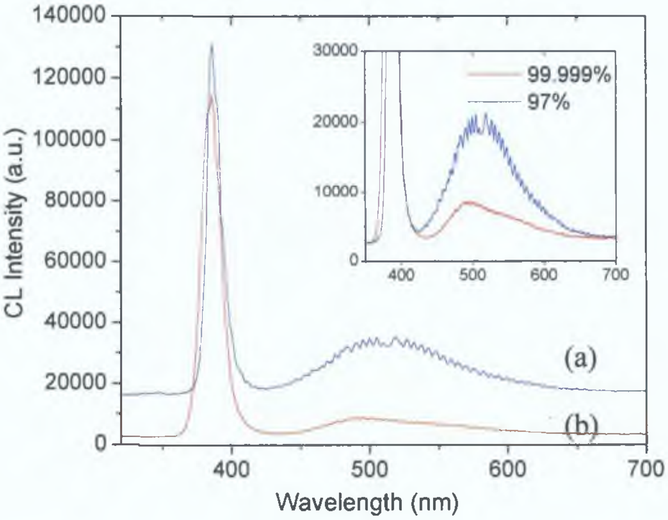

Fig. 4.23 CL spectra of CuCl on Si (a) CuCl powder purity = 97% (b) CuCl powder purity = 99.999%

Comparing spectra labeled (a) and (b) of fig.4.23 it is noted that the broad band feature was common to samples with starting CuCl powders of both 97% and 99.999% purity, respectively, suggesting that they are perhaps intrinsic features. It is however seen in the inset that the relative intensity of the Z_3 excitonic emission to the intensity of the broad band is greater for the high purity sample. An obvious candidate which could be producing the broad defect band is the presence of small amounts of oxidised CuCl (either in the form of Cu(OH)Cl or possibly $CuCl_2$) which we know to be present. The CL emission of a 500nm CuCl film on Si grown from powder of 99.999% purity was measured over a period of ~ 1.5 months. A selection of plots showing the trend is shown below.

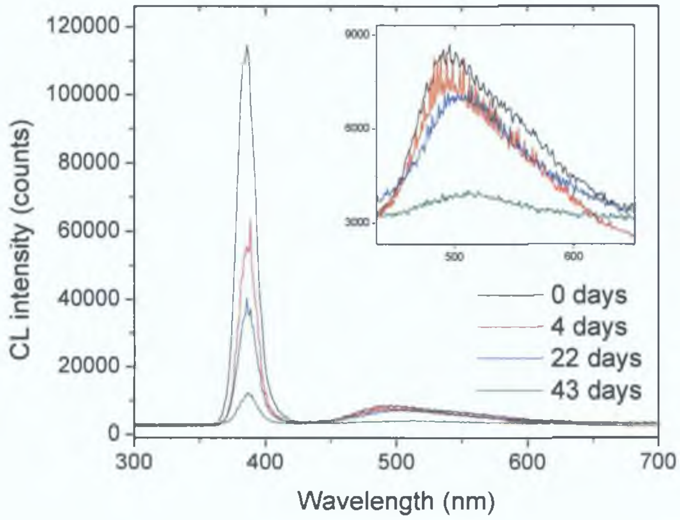

Fig. 4.24 CL spectra of a 500nm CuCl film on Si as a function of time since deposition

A reduction in the intensity of the Z_3 free exciton emission is evident 4 days after the film has been deposited. After this time the intensity of the excitonic emission continues to slowly decrease. 43 days after deposition a weak exciton peak is still present in the CL spectra. This indicates that a slower degradation may occur for CuCl deposited on Si than for CuCl deposited on glass as the UV-Vis absorption spectra showed the complete removal of the excitonic peak 18 days after deposition (fig 4 4) However, it is also likely that CL is a more efficient way of probing the luminescence as the electrons will penetrate through the upper layers of degraded material to excite the underlying CuCl

To analyse the change in the broad band as a function of time, the ratio of the intensity of the Z_3 exciton to that of the broadband (corrected for the background count level) is plotted as a function of time (fig 4 25)

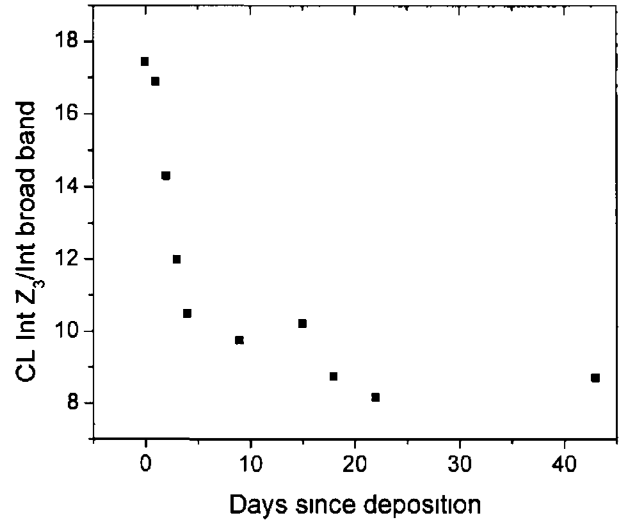

Fig 4 25 Intensity ratio of Z_3 free exciton to broad band emission as a function of time since deposition

Initially the intensity of the excitonic peak is decreasing much more quickly than the intensity of the defect band and a sharp drop is seen in the Z_3 to broad band peak intensity ratio (Int Z_3/Int broad band) This can also be seen by examining the inset of fig 4 24 However, after approximately 9 days the Int Z_3/Int broad band begins to slowly level out We do not see any increase in the intensity of the broad band as a function of time and therefore it seems unlikely that it can be assigned to one of the compounds associated with the degradation of CuCl

In an attempt to further understand the exact nature of this defect and determine its origin, CL was also investigated as a function of CuCl thickness Fig 4 26 shows an example of CL spectra for a 1000nm and 100nm CuCl film on Si (100), respectively, both samples were prepared from CuCl powder of 97% purity The broadening of the free exciton peak of the 100nm film relative to that of the 1000nm film is due to using a wider slit to acquire the spectra in order to have a comparable intensity of the Z_3 peak despite the smaller excitation volume

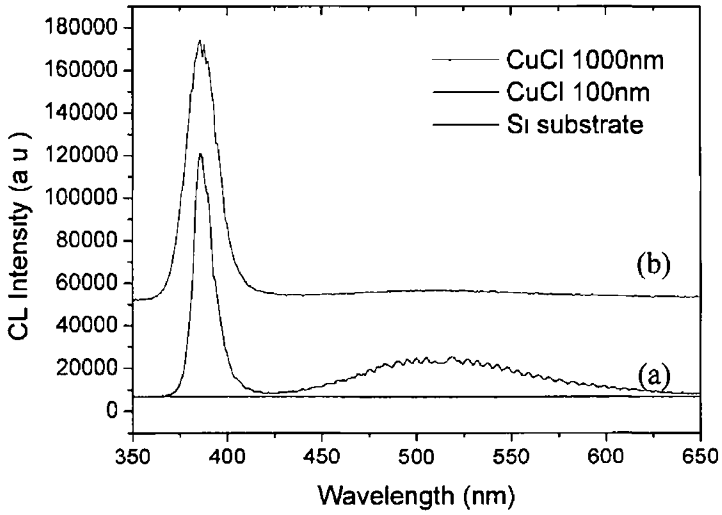

Fig 4 26 CL spectra of CuCl on Si (100) (a) Thickness ~1000nm (b) Thickness ~ 100nm The spectrum of a Si substrate is shown for comparison

It is clearly seen that the intensity ratio of the Z_3 excitonic emission to the broad defect band emission (Int Z_3/Int broad band) decreases dramatically with film thickness from ~23 0 for the 100nm film to ~7 2 for the 1000nm film This suggests that this blue-green emission originates in the bulk of the CuCl crystal, not at the

CuCl/Si interface It could therefore be related to grain boundaries as we know from the XRD measurements that the CuCl thin film is polycrystalline Further evidence supporting this explanation was uncovered in studies of CuCl powder dissolved in PMMA (polymethyl-methacrylate) matrices and deposited on a silicon substrate using a spin-on technique followed by curing at 100°C for 30 minutes[k] An example CL spectrum of one such sample excited with an electron beam of 7keV and probe current of 15nA is shown in fig 4 27 below

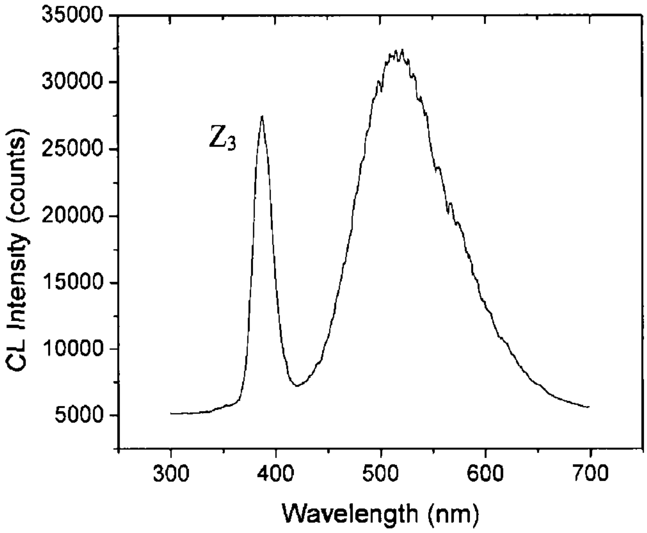

Fig 4 27 CL spectrum of CuCl dissolved in PMMA glass matrices on Si

Although a strong free exciton peak at 389nm is still present, this spectrum is dominated by a broad band centred at 522nm The nature of the deposition method results in microcrystallites of CuCl dispersed throughout the PMMA matrices There is therefore a greater volume of grain boundaries compared to a thin film of CuCl deposited on Si by the vacuum deposition technique

---

[k] These samples were prepared by Sandra Jouan during a Masters research project at Dublin City University

Similar to the studies on the PL properties, CL was also performed on CuCl thin films grown on both p-Si (100) and p-Si (111) substrates in order to determine whether the difference in crystallinity observed by XRD will have any impact on the CL emission An example is shown in fig 4 28 below for the 100nm thin film with low broad band intensity

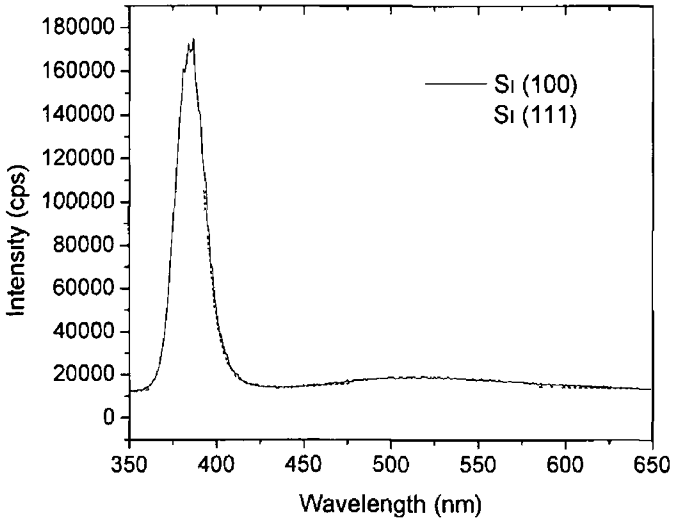

Fig 4 28 CL spectra of 100nm CuCl thin film on Si (100) and Si (111) respectively

The CL intensity of the CuCl thin film on the Si (111) substrate is slightly less than that of the Si (100) substrate but there is no significant difference between the spectra This is consistent with the PL spectra which do not appear to be significantly dependent on the substrate orientation Any variations in the CL emission caused by a microstructural difference from growth on substrates of different orientations would be more likely to be detected at low temperature Temperature dependent measurements were not possible with this CL system In addition to being a potential cause of the broad blue-green emission band, the grain boundaries of the microcrystallites would also be expected to act as sources of non-radiative de-excitation As the CL intensity is strong in all samples, it indicates that the recombination length of the electron-hole pair is shorter than the distance between grain boundaries This distance is estimated at ~ 70nm from the Scherrer crystal size calculation extracted from the XRD data (section 3 1)

Chapter 5

Electrical Properties and Doping of CuCl

5.1 Electrical characteristics of Undoped CuCl

The resistivity of CuCl thin films on glass was measured using a conventional four-point probe instrument from Veeco as described in section 2 10 All measurements were performed on the same day as the evaporation to avoid degradation effects Evaporations were performed at rates varying from 0 1 – 2 5nm/sec using CuCl powders of both 97% and 99 999% purity

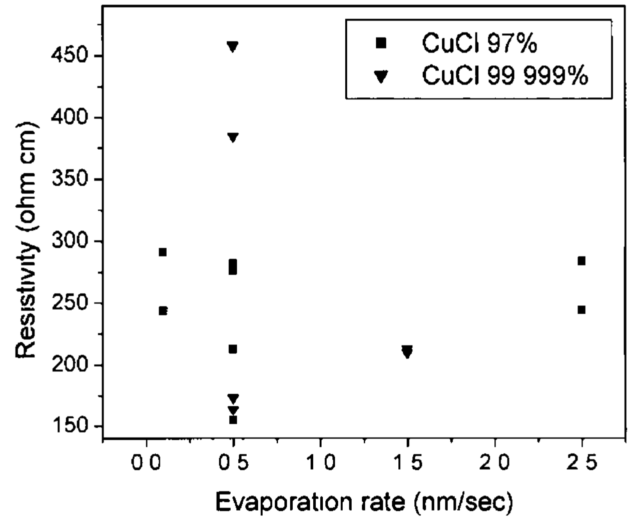

Fig 5 1 Resistivity of a CuCl thin film on glass as a function of evaporation rate

The resistivity data for each point shown if fig 5 1 comprises of average measurements of ten positions on the sample using the four-point probe For each point, a typical error value of ± 20Ωcm is calculated from the standard deviation of the ten measurements Error bars are not shown, as in this scatter plot representation it obscured the data. The thickness of each sample was measured by atomic force microscopy (AFM) in order to ensure an accurate calculation of the resistivity. There is no clear correlation between the evaporation rate and the resistivity of the resulting sample. All other evaporation conditions were the same. There is a large spread in the calculated resistivity of the CuCl films particularly in the case of the high purity films. An average resistivity value of 249 ± 46Ωcm and 295 ± 130Ωcm was measured for CuCl of nominally 97% and 99.999% purity, respectively.

To determine the conductivity type of the thin films the rectification technique (section 2.11) is used whereby the sign of the conductivity is determined by the polarity of a rectified ac signal at a point contact to the semiconductor [154]. For the samples grown from CuCl powder of 97% purity, a small positive voltage was measured indicating that the conductivity of the samples was weakly n-type. The main impurities in this powder (as listed by the supplier) include SO_4 ($\leq$ 0.5%) and Fe ($\leq$ 0.01%), which may cause a doping effect. Applying the rectification technique to the samples grown from CuCl powder of 99.999% purity resulted in a very small voltage which fluctuated from negative to positive, indicating a highly resistive or compensated material. All the electrical measurements described in the rest of this chapter were performed on samples with a typical thickness of ~ 500nm, evaporated from CuCl powder of 99.999% purity onto a glass substrate using a standard evaporation rate of 0.5nm/sec.

5.2 Metal contacts on undoped CuCl

The choice of metal used to make electrical contacts on a semiconductor depends on the conductivity type and work function of the semiconductor (section 2 13) For an n-type semiconductor an Ohmic contact is made when the work function of the metal is less than the work function of the semiconductor, $\phi_m < \phi_s$ and for a p-type semiconductor the metal work function should be greater than that of the semiconductor, $\phi_m > \phi s$ According to this Schottky-Mott theory [158], the barrier height therefore depends only on the metal work function and on the semiconductor electron affinity This describes an ideal semiconductor-metal contact However, in reality the situation can be much more complicated For example, the Fermi level pinning in GaAs has been widely investigated and it was found that the same pinning energies are observed for many metals e g Au, Ag and Cu, on n-type and p-type GaAs [159] An Ohmic metal contact to n-type GaAs is commonly attained by using an AuGe-Ni-Au alloy deposited by evaporation, followed by thermal anneal [194] During the alloying process, Ge diffuses into the GaAs creating a highly conductive n^+- type layer below the contact Ni improves the contact adherence Au enhances the out-diffusion of Ga, resulting in Ge substituting Ga sites, producing a highly doped n^+- GaAs layer [194] This enables electron tunnelling through the surface barrier resulting in an Ohmic contact

The main aim in investigating metal contacts on CuCl was to enable electrical characterisation using techniques such as the Hall effect which requires Ohmic contacts The values of the work functions of some metals commonly used to make electrical contacts are listed in table 5 1

Metal	Work Function (eV)
Al	4.28
Au	5.1
Cu	4.65
Ga	4.2
In	4.12
Ti	4.33
Ni	5.15

Table 5.1 Work function values for some common metals [195]

As there are no reported values of the work function of CuCl and the conductivity type could not be determined using the rectification technique, I tried a number of metals of varying work functions, namely Au, Cu and Al (work functions of 5.1 eV, 4.65 eV and 4.28 eV, respectively) as a first test in an attempt to make Ohmic contacts to CuCl. Metal contacts with thickness of ~ 150 - 200nm were deposited by thermal evaporation onto the CuCl film. Fig. 5.2 below shows the current-voltage (IV) characteristics of evaporated Au and Cu contacts on a nominally undoped CuCl film on glass.

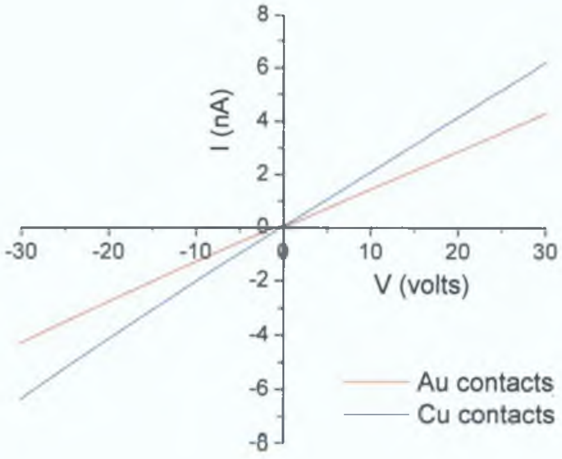

Fig. 5.2. IV curve of undoped CuCl with Au and Cu contacts

In both cases, approximately linear IV characteristics are measured in the range of ±30V However, the current flowing through the sample is very low with a maximum value of ~5nA for Au contacts and ~7nA for Cu contacts An improvement in the current flow by a factor of 10 was achieved by using Al contacts (fig 5 3), but considerable variation in IV characteristics was detected both within the same sample, and from different samples

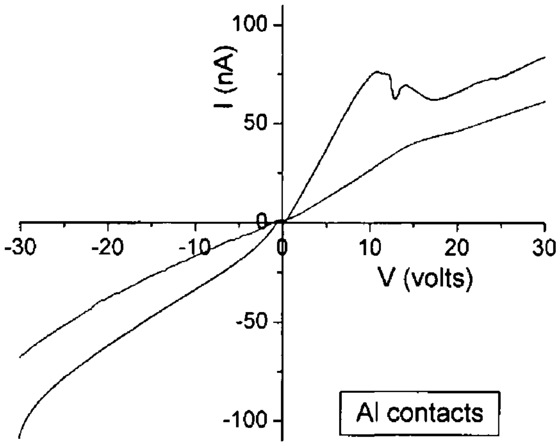

Fig 5 3 IV curve of undoped CuCl with Al contacts, two positions on the same sample

At best, the IV curve of Al contacts was approximately linear in the range of ± 10V but this was not consistently reproducible The optical micrograph below illustrates what seem to be numerous grain boundaries on the surface of the Al contact

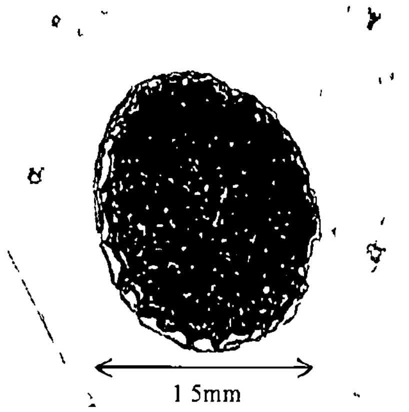

Fig 5 4 Optical micrograph of evaporated Al contact on CuCl showing grain boundaries

The Al evaporated on CuCl has a rough appearance and is a dull rusty brown colour while the Al on glass is silver and shiny as expected This suggests that a reaction occurs between CuCl and Al It is known that Al reacts vigorously with chlorine to form aluminium trichloride ($AlCl_3$) [48] The following reaction can occur between CuCl and Al

$$Al(s) + 3CuCl(s) \rightarrow AlCl_3(s) + 3Cu(s)$$

Heats of formation can be used to predict if a reaction is likely to occur [178] In this case, the large Gibbs energy of formation value for $AlCl_3$ of -628 8kJ [179] means that it is thermodynamically favourable to break the CuCl bond to form $AlCl_3$ It appears likely that a reaction between the Al contact and CuCl film is the cause of the unpredictable IV behaviour of the Al contacts Similar reactions are expected to occur between CuCl and Ti and Ni contacts forming $TiCl_4$ and $NiCl_2$, respectively Conversely, the chlorides of Au (AuCl and $[AuCl_3]_2$) are both unstable compounds which decompose below 300°C [48] The formation energies of these compounds are therefore low compared to that of CuCl [179], so no reaction occurs with CuCl To investigate whether the combination of a reactive metal, followed by a stable metal contact such as Cu or Au may allow for the enhanced current injection observed by using Al, while making a more reliable contact, combinations of reactive and stable contacts were examined Some example IV plots are shown below

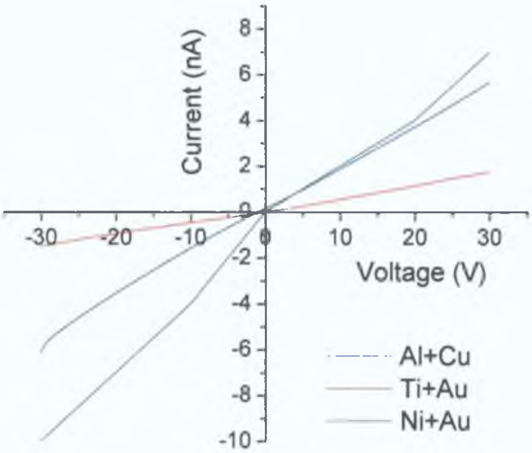

Fig. 5.5 IV curve of undoped CuCl with metal contacts of Al-Cu, Ti-Au and Ni-Au

Al-Cu, and Ti-Au evaporated contacts both resulted in approximately linear IV characteristics, however the current flowing through the CuCl sample was again very low with a maximum of ~6nA for an input voltage of 30V which does not represent any improvement compared to the deposited Au and Cu contacts. The Ni-Au contacts were not very linear and again the current flow was very low, ~10nA. We then attempted to improve the IV characteristics by annealing in the temperature range of 50-300°C for 5-30minutes in a N_2 or Ar ambient. No significant changes were detected following heat treatment and the IV curves were very similar to those shown above.

GaIn eutectic paste has been successfully used to make electrical contacts to wide bandgap semiconductors such as ZnO [128]. A GaIn eutectic paste was formed by dissolving indium powder in gallium by heating at 200°C in the ratio of 21 weight % indium to form a GaIn mixture with a eutectic temperature of ~15°C [196]. The paste was applied to the evaporated CuCl film in an inexact Van der Pauw contact geometry, and IV measurements performed as before.

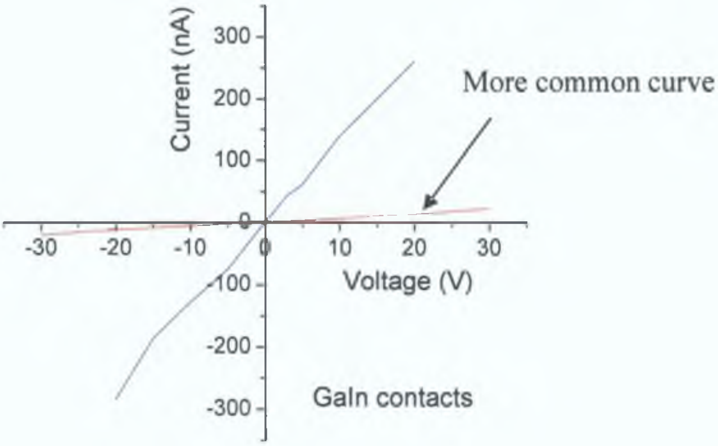

Fig. 5.6 IV curve of undoped CuCl with GaIn contacts

In some cases a promising result was obtained with approximately linear IV characteristics in the range of ±20V and a maximum current of ~280nA as shown by the blue curve in fig.5.6. However this result was not easy to reproduce and a more common result is represented by the red curve in the same figure. Placement of the contacts was not precise, often resulting in an asymmetry in the IV characteristics from different sets of contacts in the Van der Pauw geometry. Also, it was observed from a colour change of the GaIn contact from silver to brown that a chemical reaction took place with the CuCl. Similar to Al metal, examining the thermodynamics of the reaction, we found that due to the large Gibbs free energy of formation of $GaCl_3$ it was more energetically favourable to break the CuCl bond and form a Ga-Cl compound.

Hall effect measurements were attempted on the undoped CuCl films using metal contacts such as Au, Cu and GaIn. In each case it was impossible to extract any Hall voltage from the noise fluctuations of the voltmeter on placing the sample in a magnetic field of 0.75T. The voltage sensitivity of our Hall measurement system was limited to 0.01mV. Reported CuBr Hall effect measurements in a magnetic field of 0.32T, detecting p-type conduction with a carrier concentration ~ 10^{17}, quoted Hall voltage values as low as 0.2μV for an injection current of 0.1mA [120]. Therefore it seems that the very low current flow through the undoped CuCl films inhibits the Hall effect measurements using a conventional Hall effect set-up.

5.3 Electroluminescence

A test electroluminescent device (ELD) based on the growth of γ-CuCl on Si was designed in our laboratory. The aims in developing this structure were to confirm the compatibility of CuCl with Si, to confirm that no deleterious CuCl-Si interaction occurs during device fabrication, and to demonstrate UV light emission upon a lattice-matched Si substrate. A cross-sectional view of the ELD structure is shown in Fig. 5.7.

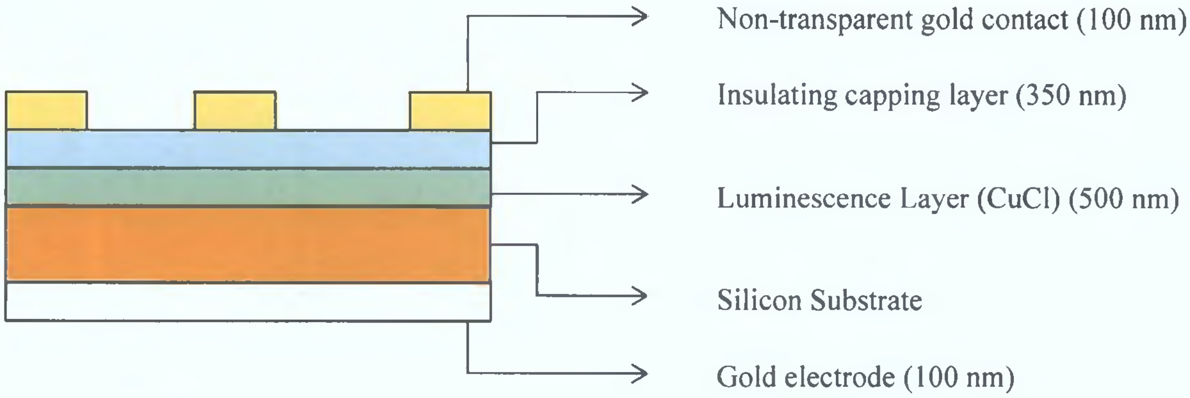

Fig. 5.7 Schematic diagram of the electroluminescent device structure. "A new γ-CuCl based electroluminescent device for the production of ultra-violet light on a silicon substrate" (Patrick J. McNally, David Cameron, Lisa O'Reilly, Gomathi Natarajan, Olabanji Francis Lucas, Alec Reader). Application No. : 2004/0442. Filing Date: 25 June 2004. International Application No. PCT/IE2005/000072.

A gold ohmic contact layer was deposited on the unpolished side of a p-type silicon substrate by sputtering followed by a thermal anneal at 300°C in Ar gas. The γ-CuCl was deposited on the polished side of the prepared silicon wafer by thermal evaporation, as already discussed. To maximise the active layer electric field, the insulator should have a high dielectric constant and sufficient electric field strength to avoid breakdown [146]. In our case the insulator also had the function of encapsulating CuCl to protect it from the ambient. As mentioned, three insulators were investigated in our laboratory by Francis Olabanji Lucas, (1) SiO_2 deposited by plasma enhanced chemical vapour deposition (PECVD), (2) Organic polysilsesquioxane (PSSQ) spin-on glass-based dielectric and (3) Cyclo olefin copolymer (COC) -based dielectric. The dielectric constants of the protective layers were determined from capacitance-frequency plots at 1MHz to be 2.3, 3.6 and 6.9 for COC, PECVD SiO_2 and PSSQ, respectively [181]. The commercially available PSSQ based solution made by the Emulsitone® Inc. (USA) was chosen as the insulator for the ELD device and was deposited using a dip-coating technique. The γ-CuCl/Si structure was immersed in PSSQ solution at room temperature for approximately 15 minutes. After withdrawing, it was dried in air for five minutes, and then baked in vacuo at a temperature of 150°C for 1 hour. The thickness of the capping layer was estimated to be ~ 350 nm using a stylus profilometer. Gold contacts were fabricated above this layer by sputtering. The electric field in the luminescent layer can be calculated according to the following equation [146,197],

$$E_{EL} = \frac{\varepsilon_i}{\varepsilon_i d_{EL} + \varepsilon_{EL} d_i} V_{tot}$$

where ε is the dielectric constant, d is the layer thickness, and the subscripts i and EL represent the insulator and the luminescent layer respectively. Using the reported value of 7.9 [198] for the low frequency dielectric constant of CuCl, the electric field in a 500nm CuCl luminescence layer is calculated as 1.1 - 1.7 MVcm^{-1} for applied voltages in the range of 100 - 150V. At these extremely high electric fields, the injected electrons quickly accelerate to high energies resulting in light emission through hot-electron impact excitation of electron-hole pairs. As the Au electrode was non-transparent, electroluminescence (EL) emission was observed principally from the edges of the electrode; hence the intensity of the spectrum is rather low.

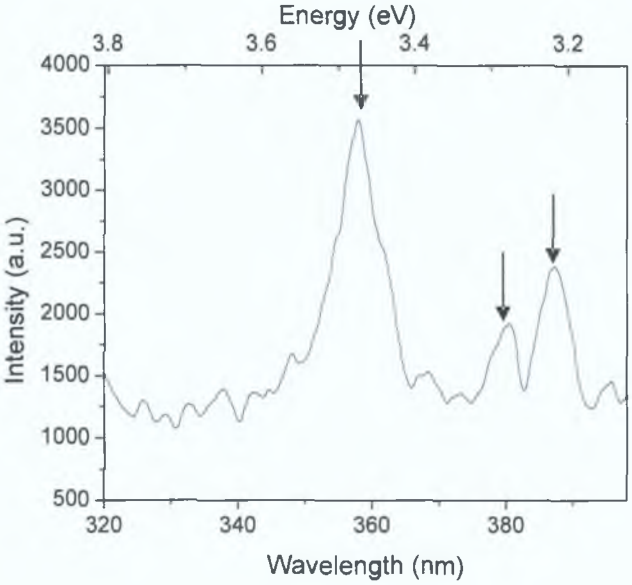

Fig. 5.8 A typical plot of electroluminescence output intensity as a function of wavelength at room temperature. The data was passed through a Savitzky-Golay smoothing filter.

The main feature of the spectrum (figure 5.8) is a broad band centred on 359nm (3.46eV). Assuming that the direct bandgap follows the same temperature dependence as that reported for the Z_3 free exciton [81] the bandgap emission should appear at ~361nm. Therefore the main band at 359nm is probably due to emission from the direct band-to-band transition. Two further peaks can be identified at ~ 380nm (3.27eV) and ~ 387nm (3.21eV). It is noted that in some spectra from a second sample prepared using the same procedure, these peaks were relatively more intense compared to the direct bandgap emission as shown by the red curve in fig 5.9.

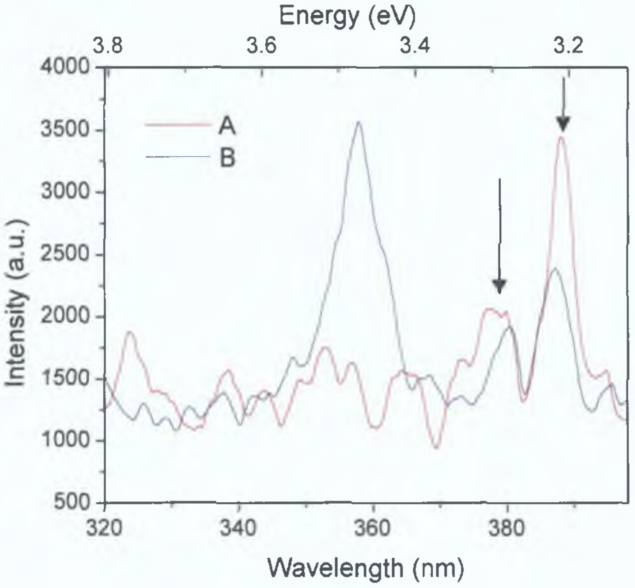

Fig. 5.9 Comparison of EL emission from samples A and B, prepared using the same procedure. The data was passed through a Savitzky-Golay smoothing filter.

The peak at ~ 387nm agrees with the Z_3 excitonic emission also seen in room temperature CL measurements as already discussed (section 4.3). The energy separation of the peaks of approximately 60meV is consistent with that of the $Z_{1,2}$ and Z_3 excitons observed in room-temperature UV-Vis absorption measurements. Therefore the emission at ~ 380nm can be tentatively assigned to a $Z_{1,2}$ excitonic emission.

5.4 Doping of CuCl

Both n-type and p-type CuCl will be required for development of homojunction light-emitting diodes (LEDs). The most efficient solid-state emitters are p-n junctions; therefore investigations of the possibility of doping CuCl are of great interest. To the best of our knowledge there are no reports on the n-type doping of copper halides Group II elements, substituting on the Cu site, should act as electron donors Zn was chosen as a dopant for vacuum deposited CuCl as co-evaporation of CuCl and $ZnCl_2$ is possible due to the similar vapour pressures (10Pa at 459°C and 356°C for CuCl and $ZnCl_2$, respectively [199]) Also, importantly, the ionic radii of the Cu (I) and Zn (II) ions in tetrahedral coordination are equivalent with a value of 74pm [48] and therefore direct substitutions of Cu atoms by Zn should be possible

CuCl powder of 99 999% purity was mixed thoroughly with $ZnCl_2$ powder of 98% purity (Merck) in proportions of one - four mole % $ZnCl_2$ as weighed on a micro-balance to an accuracy of 0 001g The CuCl/$ZnCl_2$ powder mixture was heated in a quartz crucible and the evaporation rate, which was controlled by monitoring the frequency of a crystal oscillator, was approximately 0 5 nms^{1}, similar to the undoped material

The rectification technique was used to determine the conductivity type of the doped material [154] Unlike the nominally undoped samples (99 999% purity) in which the measured voltage drop is very small and fluctuates from negative to positive, measurements on CuCl samples doped by the co-evaporation of $ZnCl_2$ have indicated by a stable positive voltage at several positions on the sample, that without exception the material is n-type The resistivity of the samples was investigated using a standard four point probe and is plotted as a function of mole % $ZnCl_2$ in fig 5 10

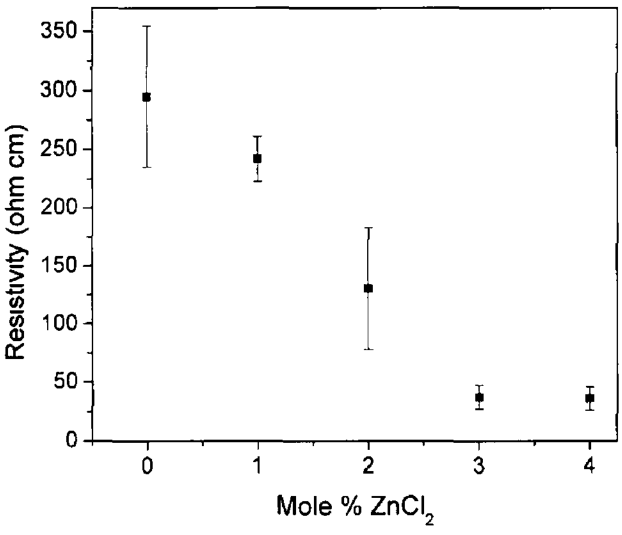

Fig 5 10 Resistivity of CuCl film as a function of mole % $ZnCl_2$

A clear decrease in the resistivity of the CuCl thin film was detected, with values decreasing from an average value of 295Ωcm for undoped material (99 999% powder) to 37Ωcm for a sample doped with a nominal 3 mole % $ZnCl_2$ Increasing the doping level to a nominal 4 mole % $ZnCl_2$ resulted in a similar resistivity value This suggests that a saturation level has been reached When performing the four-point probe measurements a standard value of 25V DC was applied to the outer probes on the sample Although we see only a small drop in resistivity (~18%) from the undoped film to that doped with a nominal 1 mole % $ZnCl_2$, there was a distinct increase (greater than two orders of magnitude), in the average current measured for the same applied voltage

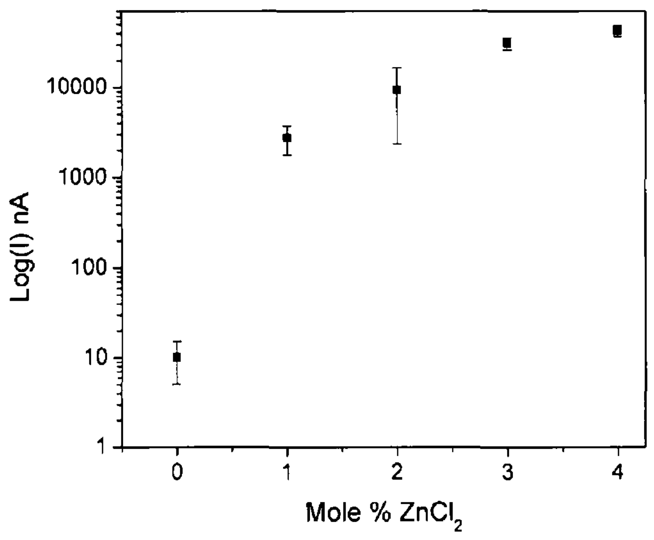

Fig 5 11 Average current measured for an applied voltage of 25V as a function of mole % $ZnCl_2$

This increase in current continued at higher doping levels as shown in fig 5 11, and begins to level out at 3-4 mole % doping in agreement with the resistivity results

It is clear that the doped films have a considerably greater current-carrying ability compared to the undoped CuCl films

5.5 Metal Contacts and Hall Effect

A number of combinations of metal contacts were investigated in an attempt to deposit high quality Ohmic contacts on Zn-doped CuCl to enable electrical characterisation using the Hall effect Some example IV curves are shown in fig 5 12 below for evaporated Au contacts and contacts prepared by evaporating first Al, followed by Au

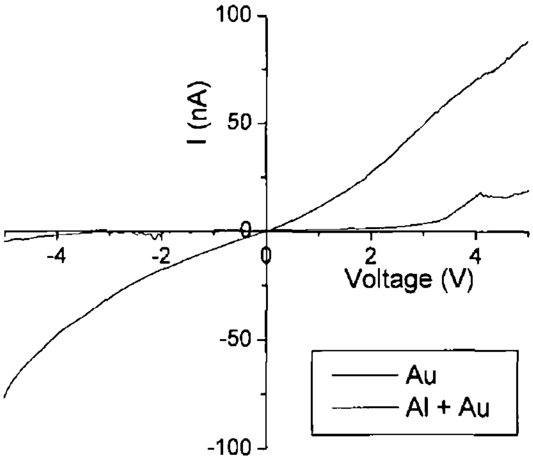

Fig 5 12 IV characteristics of CuCl doped with a nominal 3 mole % $ZnCl_2$ with Au and Al + Au metal contacts

For the Al-Au contacts, there is a marked increase in the current values (~90nA at 5V) compared to the values of undoped CuCl (~12nA at 5V) This is to be expected due to the improved current-carrying ability of the Zn-doped films However the IV curve is non-linear and therefore unsuitable for Hall effect measurements

Although the IV characteristics of the Au contacts are roughly linear in the voltage range of ±3V, it was found that on increasing the voltage input a rectified IV behaviour occurred as shown in fig 5 13 below

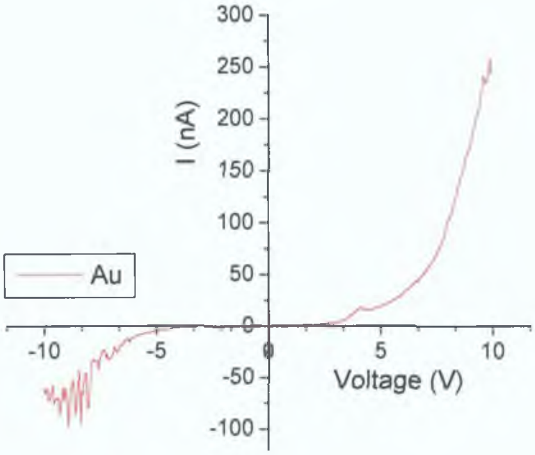

Fig. 5.13 Rectified IV characteristics of Zn-doped CuCl with Au metal contacts

In reported work on the electrical characterisation of CuBr, IV measurements were performed using both Au and Cu electrical contacts in a sandwich type structure (Au/CuBr/Au and Cu/CuBr/Cu) [122]. Non-linear IV responses were measured using Au electrodes while Cu electrodes resulted in an Ohmic behaviour. They attributed this result to the blocking of ionic current by the Au electrodes which is a purely electronic conductor while the Cu electrodes conduct both ionic and electronic current [122,123]. As Au contacts to undoped CuCl resulted in linear IV characteristics (fig. 5.2), this implies that doping CuCl with Zn may result in increased ionic current as well as an electronic doping effect. However there are other unknown factors affecting the contact mechanism such as barrier heights, Fermi level pinning and surface states [200].

Ohmic contacts to CuCl doped with a nominal 2-3 mole % Zn in the range of ±5V were achieved using Cu-Au co-evaporated metal contacts. A thermal anneal at 150°C for 5 minutes in Ar gas improved the uniformity of the contact pairs in the Van der

Pauw structure. The Cu will allow for ionic conduction but it reacts readily with oxygen to form CuO_x compounds. Combining it with Au appears to stabilise the contact.

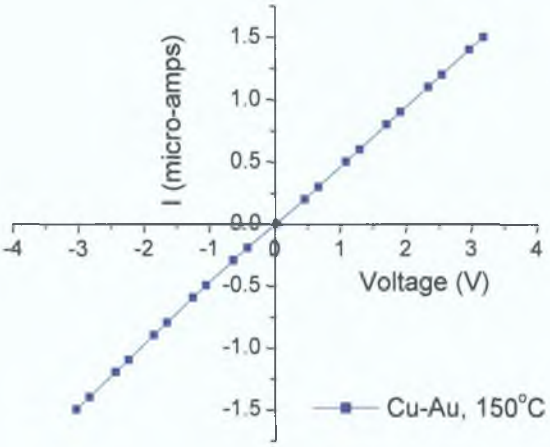

Fig. 5.14 Linear IV characteristics of CuCl doped with a nominal 3 mole % $ZnCl_2$ with Cu-Au metal contacts

The average measured current values at 5V ranged from 1-2μA for a CuCl sample doped with a nominal 3 mole % $ZnCl_2$. This is a distinct improvement compared to the undoped CuCl in which the maximum current was ~10nA for metal contacts with a linear IV response. Van der Pauw resistivity and Hall effect measurements were carried out on samples with doping levels of 1-3mole% $ZnCl_2$. In the case of the sample with nominally 1 mole % doping, Hall measurements were not possible using the HL5500PC Hall Effect apparatus from ACCENT due to contact problems. Results were obtained for CuCl samples doped with nominally 2-3 mole % $ZnCl_2$. N-type conductivity was detected in ~70% of the performed Hall measurements on each sample. This peculiar behaviour of observing both types of conductivity for the same sample may reflect an electrical instability in the Zn-doped CuCl samples. This may result from two competing conductivity mechanisms, namely electron conduction from the substitution of Cu by Zn and hole conduction due to the presence of Cu vacancies which are known to be present in undoped material [113,114] and may also be introduced due to excess chlorine from co-evaporation with $ZnCl_2$. D.C. Look *et al.* have reported that the seeming electrical instability for *p*-ZnO can often be traced to noisy Hall effect measurements [201]. When using the Van der Pauw method, two switching configurations must be used, so that altogether, eight different measurements must be taken to determine a single Hall voltage. If contact noise is high, as in our case, a noise spike during just one of the eight Van der Pauw measurements can greatly affect the final result. This contact noise is another factor leading to a variation in the results. Fig. 5.15 shows the spread in carrier concentration and mobilities of the n-type samples as a function of mole % $ZnCl_2$.

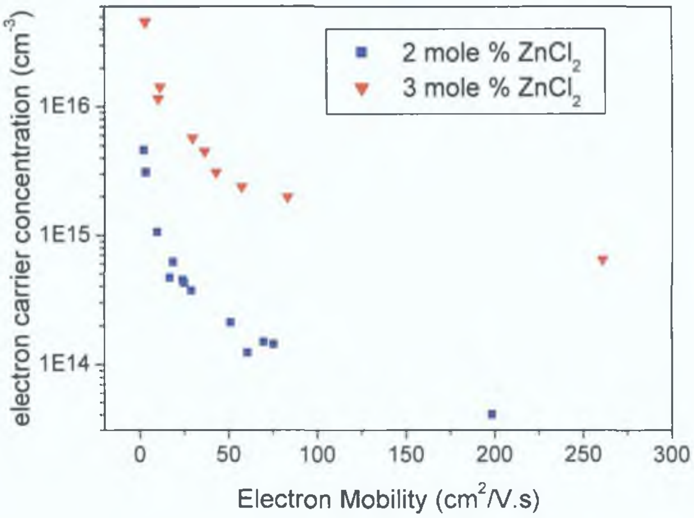

Fig. 5.15 Electron carrier concentration vs. mobility extracted from room temperature Hall effect measurements of CuCl samples doped with nominally 2 and 3 mole % $ZnCl_2$

For these CuCl samples doped with a nominal 2 mole % $ZnCl_2$ the average electron carrier concentration *n*~ 9 x $10^{14}cm^{-3}$ and Hall mobility μ~ 45 $cm^2v^{-1}s^{-1}$. For the sample doped with nominally 3 mole % $ZnCl_2$ the measured average concentration increased by approximately one order of magnitude to n~ 1 x 10^{16}cm^{3} and the average Hall mobility reduced slightly to μ~ 29 cm^{2}v^{1}s^{1} (Points in which the measured mobility was greater than 200cm^{2}v^{1}s^{1} were disregarded in the calculations of averages to present a clearer picture of the general trend) Contact problems prevented a temperature dependent Hall effect study

The measured carrier concentrations are rather low compared to typical values of 10^{18}-10^{20} for other doped semiconductors It is important to note that the doping efficiency of the CuCl/ZnCl$_2$ co-evaporation method is very low The maximum net donor concentration measured for 3 mole % ZnCl$_2$ ~10^{16} cm^{3} is much smaller than the theoretical maximum Zn concentration of 7x10^{20} cm^{3} Therefore the activation efficiency could be as small as 0 001% for this doping method, but it is also likely that the maximum concentration is not achieved through co-evaporation A higher doping efficiency would be expected from radio frequency (RF) sputtering or liquid phase epitaxy (LPE) growth techniques This will be pursued in future work

5.6 Impact of Zn-doping on Structural and Optical Properties

5 6 1 Structural Properties

A clear improvement in the electrical properties of CuCl was achieved by using the CuCl/ZnCl$_2$ co-evaporation doping method Therefore it was important to assess the impact (if any) of Zn-doping on the structural and optical properties of the CuCl films both on glass and on Si substrates Immediately following deposition of CuCl on substrates of glass, Si (111) and Si (100), respectively, XRD measurements were performed to monitor the crystallinity of the deposited CuCl thin films doped with

$ZnCl_2$. These XRD scans were then compared to the diffraction pattern of undoped CuCl thin films. Indexing of the interplanar spacing using the Bragg equation for the cubic unit cell, confirmed that, consistent with the undoped material, the Zn doped CuCl film was in the cubic zincblende form as expected at room temperature.

As glass is an amorphous substrate it should have no influence on the crystal orientation of a thin film grown upon it. Fig. 5.16, curve (a) shows a typical XRD pattern taken in the Bragg-Brentano geometry of undoped CuCl deposited on a glass substrate. In this case the intensity is multiplied by a factor of 5, and an offset applied so it can be clearly represented on the same scale as that of the more intense θ-2θ diffraction pattern of a CuCl film doped with a nominal 1 mole % $ZnCl_2$, shown in fig. 5.16, curve (b).

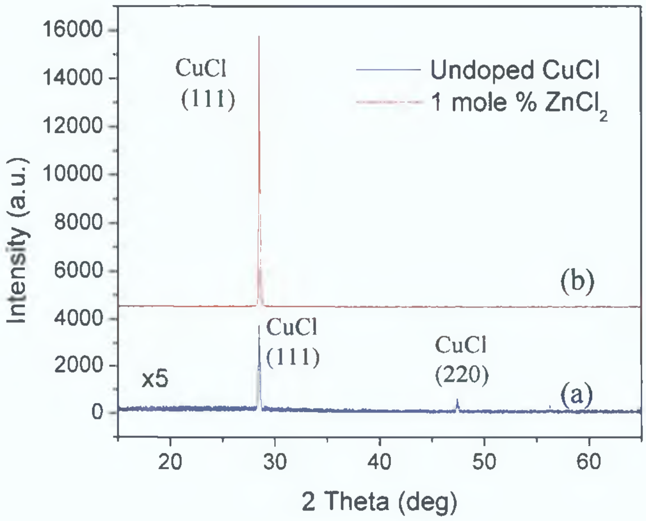

Fig. 5.16 X-ray θ-2θ diffraction pattern of (a) Undoped CuCl on glass (x 5) and (b) CuCl doped with a nominal 1 mole % $ZnCl_2$

The measurements were performed under identical conditions. The evaporated undoped CuCl film on glass is polycrystalline with a preferred <111> growth direction A small peak identified as a CuCl (220) reflection is also clearly evident The CuCl (111) and (220) peaks occur at 2θ = 28 532° and 2θ ~ 47 46° respectively corresponding to a lattice constant of 5 414Å When compared to curve (b), there is a noticeable improvement in the crystallinity of the CuCl thin film by addition of 1 mole % $ZnCl_2$ to the evaporation crucible For higher doping levels, there was also an increased (111) intensity although no definite trend emerges as shown in fig 5 17 below in which the ratio of the intensity of the CuCl (111) crystalline peak for doped and undoped CuCl is plotted as a function of mole % $ZnCl_2$

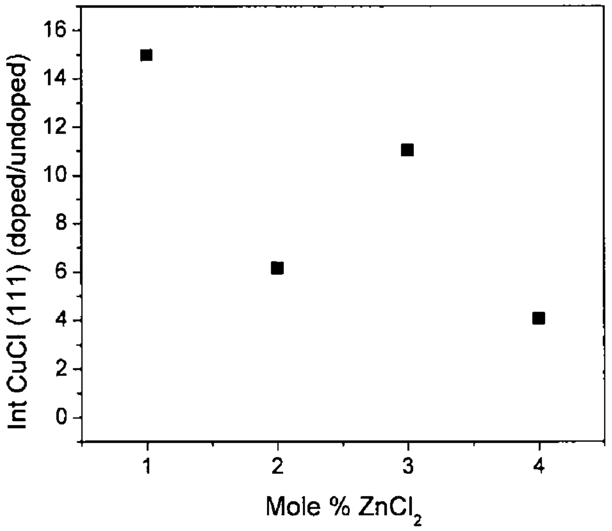

Fig 5 17 The intensity ratio of the CuCl (111) reflection for doped and undoped material as a function of mole % $ZnCl_2$

For all doping levels the intensity of the CuCl (111) reflection is at least four times greater than that of the undoped material and is as much as fifteen times greater in the case of doping with 1 mole % $ZnCl_2$ The diffraction pattern of the Zn-doped CuCl film is dominated by an intense (111) CuCl peak at 2θ = 28 537°, no other peaks are readily identifiable in this geometry although there was some evidence of CuCl (220) and (311) reflections when a glancing angle of 2° was used to probe the surface layers of the thin film.

A comparison of the rocking curve of the CuCl (111) peak for an undoped sample to that of the sample doped with a nominal 1 mole % $ZnCl_2$ is shown in fig. 5.18 below. No rocking curve peak is detected in the case of the undoped CuCl film. This indicates that the (111) oriented crystallites do not lie in an ordered array; rather they are positioned randomly with respect to the surface.

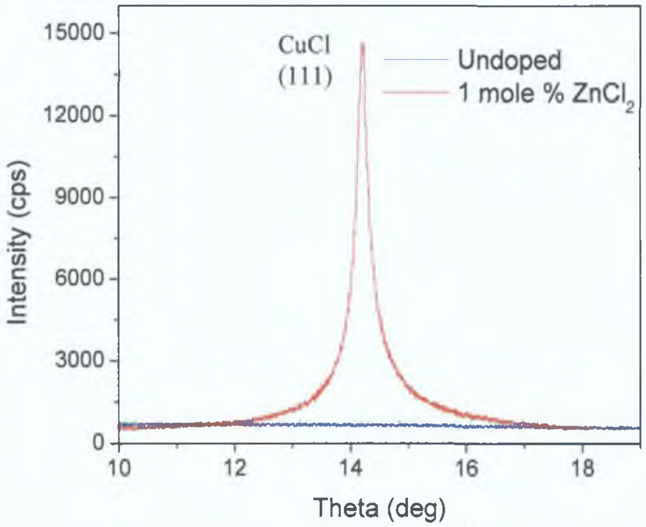

Fig. 5.18 Rocking curve of CuCl (111) reflection of undoped CuCl on glass compared to CuCl doped with a nominal 1 mole % $ZnCl_2$

An intense rocking curve peak with a FWHM of 0.38° is measured for the Zn-doped film. This indicates that the (111) crystallites of the polycrystalline Zn-doped CuCl film, are growing in a well aligned geometry. The improvement in the crystalline quality of the doped material may be related to the interaction of CuCl with $ZnCl_2$ in the evaporation crucible. CuCl forms eutectics with numerous halides. This has been utilised for flux growth using the Bridgeman technique [65,73] to lower the melting point of CuCl below the wurtzite- zincblende solid state phase transition at 407°C It is possible that the addition of $ZnCl_2$ to the CuCl helps to lower the temperature at which the powder evaporates resulting in deposited films with improved crystallinity The Scherrer formula [169] was used to estimate the crystallite size from the X-ray diffraction data of the undoped and doped CuCl on glass The average crystallite size of the undoped CuCl was calculated as ~58nm This increased by approximately 10-15nm for the Zn-doped samples No particular trend was established with respect to the Zn-doping concentration

Due to the small difference in the lattice constants of γ-CuCl and Si, the Bragg peaks occur at very similar 2θ values in the XRD spectra CuCl thin films grown on Si (100) substrates are polycrystalline in nature with no clear epitaxial alignment with the substrate (section 3 1) No significant difference was seen in the structural properties of the CuCl films doped with Zn and the undoped samples on a Si (100) substrate The only peak seen in the Bragg-Brentano geometry for undoped CuCl grown on a Si (111) substrate is an intense (111) reflection at 2θ ≈28 50° Rocking curves are therefore used to investigate the alignment of the (111) CuCl grains with the underlying Si (111) substrate Fig 5 19, curve (a) shows a rocking curve of a CuCl thin film on Si (111) substrate (blue line) superimposed on a rocking curve of a Si (111) wafer (red line)

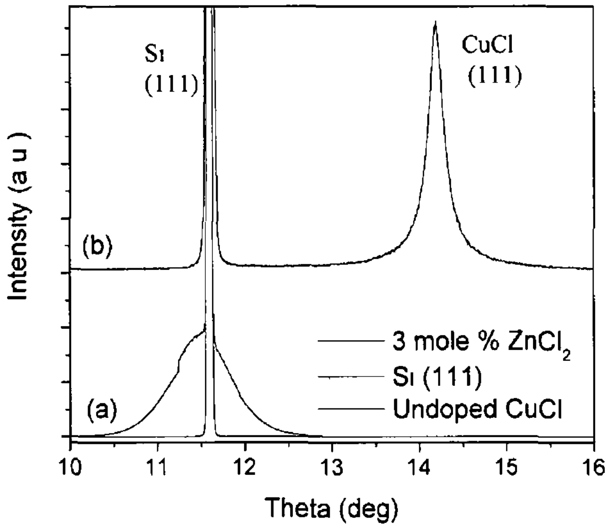

Fig 5 19 Rocking curve of Si (111) is compared to (a) Rocking curve of undoped CuCl on Si (111) and (b) Rocking curve of CuCl doped with a nominal 3 mole % $ZnCl_2$ on Si (111)

A distinct broadening at the base of the rocking curve is seen in the case of the CuCl thin film This suggests that the CuCl film consists of polycrystalline grains of (111) orientation, which are not in perfect alignment with the Si substrate as discussed in section 3 1 For Zn-doped CuCl samples, doped with a nominal 2 mole % CuCl and greater, a separation of the CuCl (111) and Si (111) reflections is seen in the rocking curve This is particularly pronounced in the case of samples doped with a nominal 3-4 mole % $ZnCl_2$ A rocking curve of a CuCl film doped with a nominal 3 mole % $ZnCl_2$ grown on Si (111) is shown in fig 5 19, curve (b) A distinct peak due to the CuCl epitaxial layer occurs at 14 19°, while a second peak from the Si (111) substrate is seen at 11 6° This separation is not only due to the small lattice mismatch between the Si and CuCl, but mainly caused by a tilt angle between the substrate layer and the epitaxial layer [202,203] The Si (111) substrates used have been cut off-axis by ~ 2-3° in the <110> direction by the manufacturer The CuCl (111) crystal planes do not grow parallel to the Si (111) planes, rather the CuCl growth appears to proceed in a manner similar to the preferentially oriented (111) growth on the glass substrate (fig 5 18) Therefore a tilt of ~ 2 6° exists between the Si substrate and CuCl epilayer The measured FWHM of 0 09° for the CuCl (111) rocking curve peak compared to 0 03° for the Si (111) peak is indicative of the reasonable crystalline quality of the material

The upward shift in the (111) 2θ peak position on both glass and Si substrates indicates a decrease in the lattice constant for the doped samples The diffraction patterns of CuCl on glass were used to calculate the lattice constant A minimum lattice constant of 5 411Å was found for a CuCl sample doped with a nominal 4 mole % $ZnCl_2$ A small spread in the average values of the lattice constant was found over the doping range investigated using a number of samples at each doping concentration

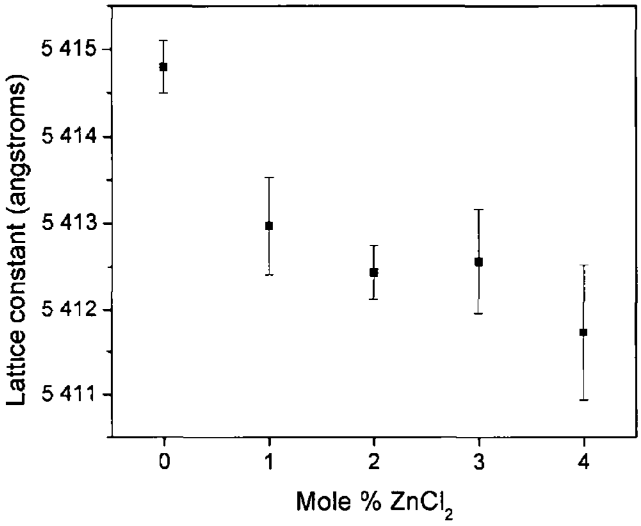

Fig 5 20 Lattice constant calculated from X-ray diffraction of doped CuCl on glass as a function of mole % $ZnCl_2$

Although there was some variation in the measured values as indicated by the error bars in fig 5 20 there is a clear difference in the lattice constant of the undoped and doped CuCl, which tends to further decrease as the Zn doping level increases. The electronegativity of Cl is 3.0, while those of Cu and Zn are 1.9 and 1.6, respectively. An increased electronegativity difference should result in a tighter bonding structure causing a slight decrease in the lattice constant. This is consistent with substitution of some Cu sites by Zn and therefore in agreement with the electrical data.

5.6.2 Optical Properties

In fig. 5.21, the room temperature UV-VIS absorption spectrum of undoped CuCl is compared to that of Zn-doped CuCl on glass substrates. The sample doped with a nominal 2 mole % $ZnCl_2$ is shown both immediately after deposition and one day later.

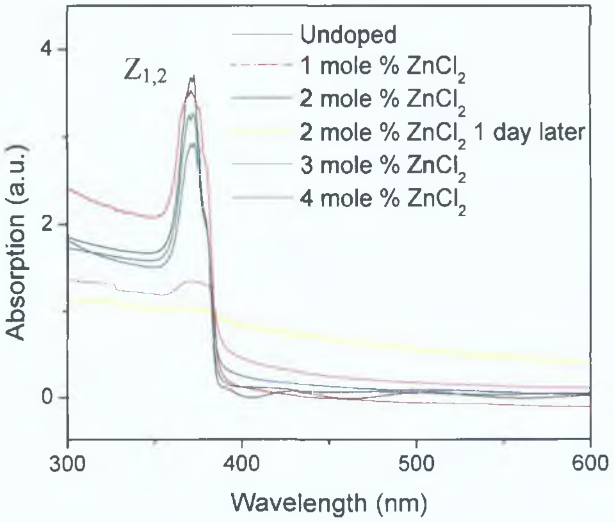

Fig. 5.21 UV-VIS absorption spectrum of undoped CuCl on glass, compared to that of CuCl doped with a nominal 1-4 mole % $ZnCl_2$; measurement taken immediately after deposition, and repeated one day after deposition of the CuCl doped with nominally 2 mole % $ZnCl_2$.

The main peak results from the contribution of both high and low energy excitonic bands, known as the $Z_{1,2}$ and Z_3 excitons, respectively. This peak (although slightly reduced in intensity compared to the undoped sample) is evident for CuCl samples doped with a nominal 1-3 mole % $ZnCl_2$ measured immediately after deposition The main peak at 372 nm (3 34eV) for the $Z_{1 2}$ exciton and a slight shoulder at 379 nm (3 28eV) corresponding to the Z_3 exciton, agree within the resolution of the instrument with the energy values of the undoped CuCl thin film and are in close agreement with values reported by other authors for room temperature CuCl absorption measurements [79,84] However doping of CuCl with nominally 4 mole % $ZnCl_2$ has severely damped the exciton and only a small bump appears at the wavelength of the excitonic emission For the sample doped with a nominal 2 mole % $ZnCl_2$, the excitonic emission has been completely quenched after just one day This is explained by the fact that CuCl is sensitive to moist air Under the influence of light and moisture, hydrated oxyhalides of Cu^{++} are formed [49] This reaction can be easily recognised by a colour change in CuCl associated with the presence of the greenish colour Cu^{++} ions and appears to be accelerated by the incorporation of Zn into the CuCl crystal This is probably because $ZnCl_2$ is also known to be hygroscopic [204] A protective layer is needed to prevent this process as it causes the optical degradation of the films We have previously shown that the excitonic emission of the UV/VIS spectrum of an undoped CuCl sample is maintained at the same intensity for at least three weeks by capping with liquid glass [205] Testing the effectiveness of this system to seal the Zn-doped CuCl thin films is currently underway

In fig 5 22 the transmittance spectrum of the undoped CuCl thin film is compared to the transmittance spectrum of Zn-doped CuCl The spectrum of the sample doped with a nominal 2 mole % $ZnCl_2$ is again shown both measured immediately and one day after deposition

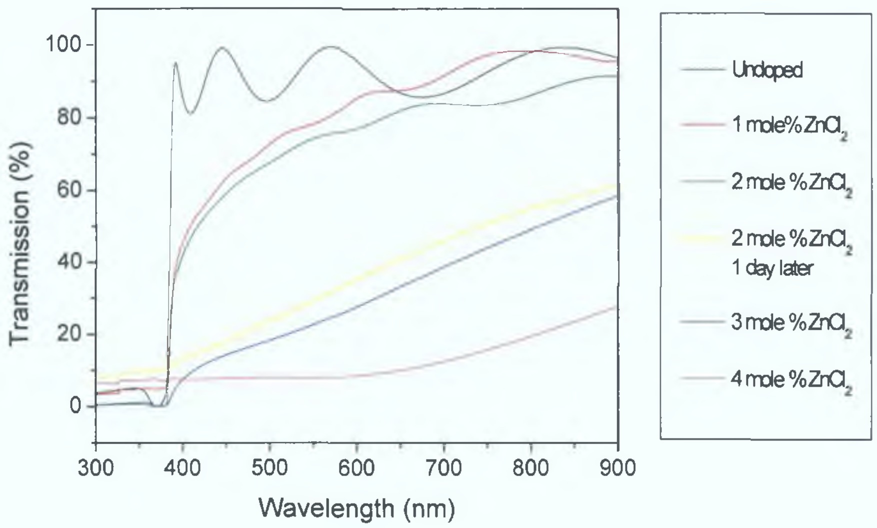

Fig. 5.22 Transmission spectrum of undoped CuCl on glass, compared to that of CuCl doped with a nominal 1-4 mole % $ZnCl_2$; measurement taken immediately after deposition, and repeated one day after deposition of the CuCl doped with nominally 2 mole % $ZnCl_2$.

The slight reduction in the transmission for the freshly prepared Zn-doped sample is not unexpected as it has been previously reported that addition of $ZnCl_2$ to the flux, in experiments on the growth of CuCl single crystals from the melt, resulted in crystals that were slightly opaque in appearance [65]. By comparing figures 5.21 and 5.22 we see that the quenching of the excitonic emission one day after deposition is accompanied by a decrease in the transmittance of the Zn-doped films. At higher doping levels (nominally 3-4 mole % $ZnCl_2$) the transmittance of the films (measured within 30 minutes after removing from the vacuum chamber) was less than 60% at all wavelengths investigated and below 20% at wavelengths shorter than 450nm. This is very similar to the transmittance spectrum shown for the sample doped with a nominal 2 mole % $ZnCl_2$ one day after deposition indicating that some degradation occurs immediately for the higher doping levels investigated. For optoelectronic device applications both the electrical conductivity and the optical transmission should be as high as possible [206]. Therefore it is important to ensure that the transmissivity is not compromised by doping. The drop in transmission as the doping level is increased can be overcome by using a suitable capping layer evaporated *in situ* to seal the Zn-doped CuCl from the atmosphere before opening the vacuum chamber. CaF_2 has previously been used as a confining/protective layer in the growth of CuCl quantum well structures [207]. A transparent CaF_2 capping layer was evaporated over a Zn-doped CuCl film without breaking the vacuum.

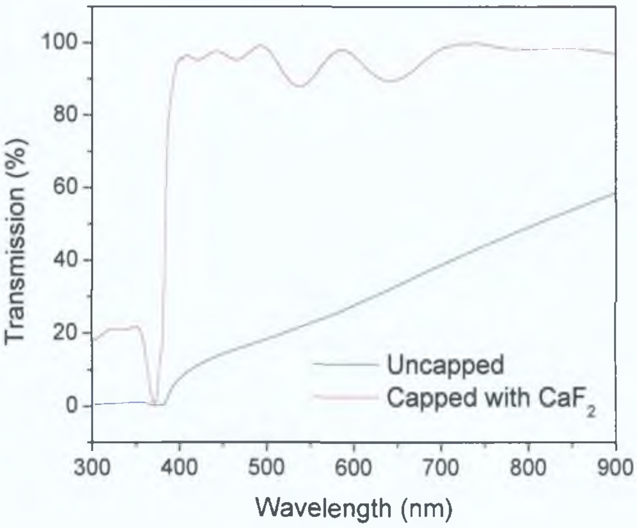

Fig. 5.23 Transmission spectrum of CuCl doped with a nominal 3 mole % $ZnCl_2$, as deposited uncapped and with an *in situ* CaF_2 capping layer

The transmission of the CuCl film doped with nominally 3 mole % $ZnCl_2$ and capped by evaporating CaF_2 is greater than 90% in the range of 400-900nm. This confirms that the low transmission of the uncapped sample is due to a fast reaction with the air resulting in an opaque film surface. The CaF_2 capping layer did not prevent the degradation of the film which still occurred within 2-3 days.

The optical emission of the Zn-doped samples grown on silicon substrates of (111) and (100) orientation were investigated using PL[1] and CL. The films doped with nominally 1-3 mole % $ZnCl_2$ have strong room temperature photoluminescence properties as shown in fig 5.24.

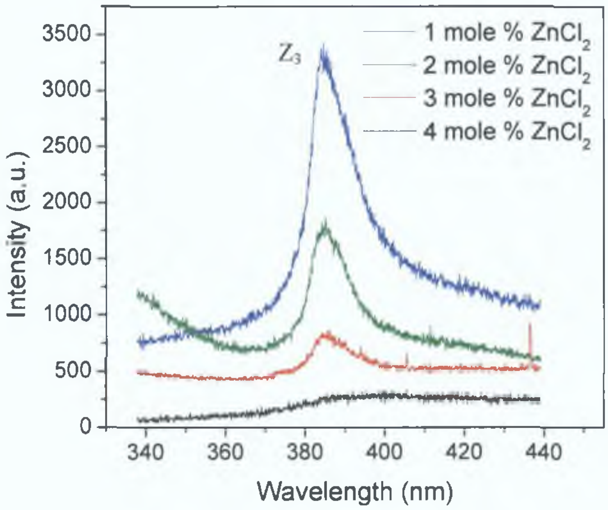

Fig. 5.24 Room temperature PL of CuCl doped with 1-4 mole% $ZnCl_2$ grown on a Si (100) substrate

For the Zn-doped films deposited on a Si (100) substrate, there appears to be a decrease in the intensity of the Z_3 free exciton emission as the doping concentration is increased. In agreement with the UV-VIS data, the excitonic emission has been quenched for the sample doped with a nominal 4 mole % $ZnCl_2$. For the samples deposited under the same conditions on a Si (111) substrate, the room temperature PL intensity is approximately the same for samples with a doping level of 1-3 mole % $ZnCl_2$ as shown if fig. 5.25. Again no excitonic emission is detected at room temperature for the sample nominally doped with 4 mole % $ZnCl_2$

---

[1] The PL measurements on Zn-doped CuCl films were also performed by Dr. Anirban Mitra in the Semiconductor Photonics Group at Trinity College, Dublin

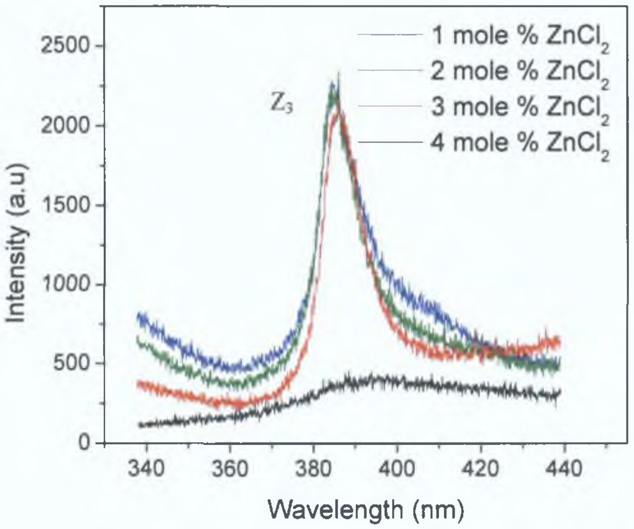

Fig. 5.25 Room temperature PL of CuCl doped with 1-4 mole% $ZnCl_2$ grown on a Si (111) substrate

The FWHM of the room temperature Z_3 exciton peak on Si (100) and Si (111) are plotted as a function of doping concentration in fig. 5.26.

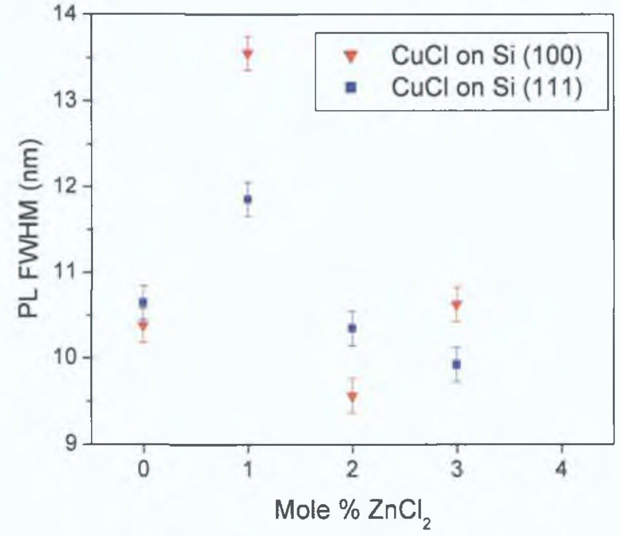

Fig. 5.26 PL FWHM at room temperature for CuCl doped with 1-4 mole% $ZnCl_2$ grown on a Si (111) and Si (100) substrate

Although the width has increased slightly for samples doped with a nominal 1 mole% $ZnCl_2$ compared to the undoped CuCl, in general the FWHM values of the doped films, (up to 3 mole % $ZnCl_2$) are equivalent or even slightly smaller than the values obtained from measurements on the undoped films This suggests that at these doping levels the PL emission is not compromised

The PL characteristics of the Zn-doped films were also investigated at low temperature A PL spectrum measured at 10K for a CuCl film doped with a nominal 3 mole % $ZnCl_2$ on Si (100) is shown in fig 5 27

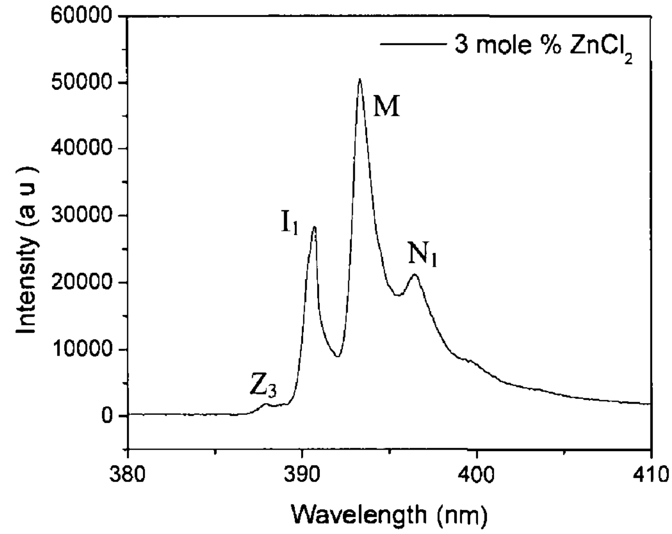

Fig 5 27 PL spectrum of CuCl doped with a nominal 3mole % $ZnCl_2$ on Si (100) at 10K

Similar to the undoped samples, four peaks are evident in the spectrum The small peak which occurs at λ ~ 387 9nm (3 204 eV) is the Z_3 free exciton peak On the low energy side of the free exciton, the peak occurring at λ ~ 390 6nm (3 183 eV) is attributed to an emission from an exciton bound to an impurity [90,186], which has been called the I_1 bound exciton In undoped material, this impurity has previously been identified as a neutral acceptor, possibly a Cu vacancy [187] A third peak, which appears at λ ~ 393 3nm (3 161eV) is identified as a free biexciton M At λ ~ 396 5nm (3 135 eV) a fourth peak labelled N_1 is evident, and likely originates from a biexciton bound to an impurity Similar to the I_1 bound exciton, the most probable candidate for the impurity is considered to be a neutral acceptor [90] The main differences between this PL spectrum and that of the undoped material at 10K is a slight shift in the peak position towards lower energies and an increase in the intensity of the free and bound biexcitons relative to the free and bound excitons The relatively low intensity signal of the Z_3 free exciton at 10K is to be expected due to the high level of biexcitons being formed For the formation of biexcitons, a very high quality film is needed to avoid excess scattering by impurities and crystalline defects before association of excitons [193] The continued detection of the excitons and biexcitons suggested to be bound to a neutral acceptor indicates that Cu vacancies may remain after the addition of $ZnCl_2$ This is not unexpected as excess chlorine could be incorporated into the CuCl crystal structure resulting in a Cu deficiency This would introduce some acceptor levels resulting in p-type conduction as mentioned in the discussion of the Hall effect measurements

The PL emission at 10K for the full set of Zn-doping levels is shown below For the samples doped with a nominal 1% and 4% $ZnCl_2$, the intensity is considerably lower and was therefore multiplied by a factor of 10 in order to clearly represent it on the same scale

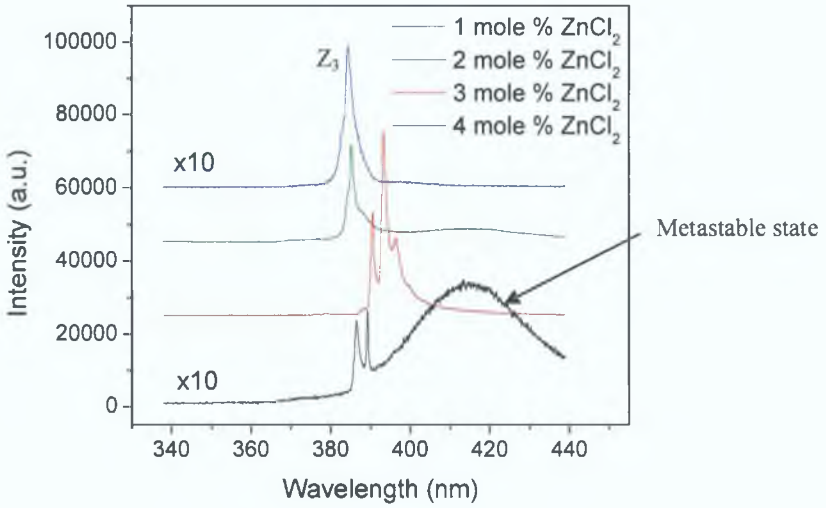

Fig. 5.28 PL at 10K of CuCl doped with a nominal 1-4 mole% $ZnCl_2$ grown on a Si (100) substrate

In all cases, the Z_3 free exciton emission can be detected at 10K but only the CuCl sample doped with a nominal 3 mole% $ZnCl_2$ exhibits four excitonic peaks as discussed above. Two excitonic peaks – the free and bound excitons are evident in the spectrum of the sample doped with a nominal 4 mole% $ZnCl_2$. The broad band centred at ~ 415nm also appeared in some spectra for the undoped CuCl film (fig. 4.17) and was labelled a metastable state as it vanishes again at higher temperatures, in this case above 72K.

Fig. 5.29 shows the room temperature CL spectra of CuCl thin film doped with a nominal 1-4 mole % $ZnCl_2$. Importantly, even at the highest Zn-doping level; the light emission resulting from the electron beam excitation is not quenched although there is a reduction in the intensity. The continued detection of the excitonic emission by CL, despite its absence in room temperature UV-VIS and PL studies at a doping concentration of nominally 4 mole % $ZnCl_2$ probably results from the reduced CL sensitivity to surface degradation compared to the other techniques as the electron beam will penetrate as far as the Si substrate creating a larger excitation volume

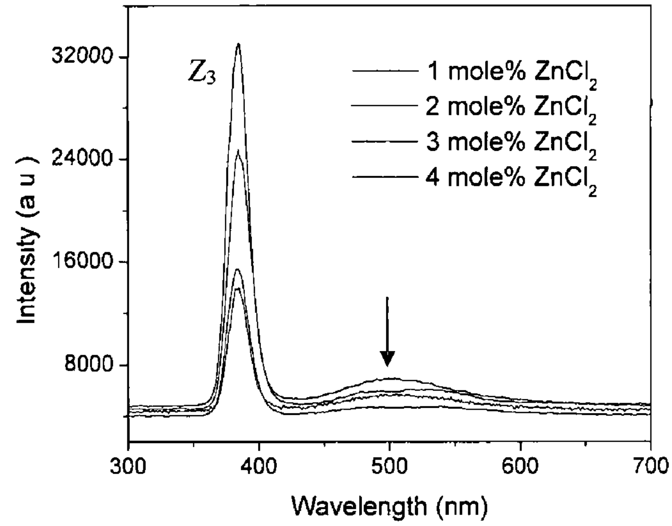

Fig 5 29 CL spectrum of CuCl doped with a nominal 1-4 mole % $ZnCl_2$ on Si (100) at room temperature

The main features include a strong emission at λ ~ 384 7 nm (3 23 eV) assigned to the Z_3 free exciton emission in agreement with the PL spectra, and a broad blue-green emission band centred at ~ 510 nm (2 43eV) This broad band also occurred in nominally undoped samples grown from CuCl powders of both 97% and 99 999% purity as discussed in section 4 3 but its exact origin has yet to be confirmed

Chapter 6

Conclusions and Future Work

We have grown textured polycrystalline closely lattice-matched γ-CuCl on Si (111) and Si (100) substrates using a simple room-temperature physical vapour deposition technique X-ray diffraction studies show that CuCl crystallises with a cubic zincblende structure and grows preferentially in the <111> direction On heating above 250°C a reaction occurs between Si and CuCl forming $SiCl_4$ gas and metallic Cu As most devices operate at temperatures below 100°C, this should not limit greatly the potential applications of the CuCl-Si material system CuCl could also be of interest for applications where low-temperature processing is required such as flexible electronics

CuCl thin films (~ 500nm thick) grown on Si (111) and Si (100) substrates have been optically characterised We found no significant differences in the optical properties of the CuCl films on the Si (111) and Si (100) oriented substrates, respectively Exciton and bi-exciton features have been identified at low temperature using photoluminescence Photoluminescence and cathodoluminescence reveal a strong room temperature Z_3 free exciton emission at ~ 387nm The optical properties of the CuCl films on Si substrates are similar to those previously reported for single crystal CuCl and thin films on other substrates Therefore we can conclude that the optical quality of CuCl thin films on Si substrates is not compromised in comparison with single crystal CuCl

CuCl is sensitive to moist air and the degradation of the film has been monitored over a number of weeks revealing the presence of oxidised Cu compounds such as Cu(OH)Cl The structural changes were examined using x-ray diffraction and x-ray microanalysis, and optical degradation detected using UV- Visible absorption and transmission measurements and cathodoluminescence To date, work in our laboratory has indicated that an organic polysilsesquioxane (PSSQ) spin-on glass or cyclo olefin copolymer (COC)-based dielectrics are successful methods of encapsulating CuCl

The application of an electrical potential difference across a metal-insulator-semiconductor structured CuCl on Si based electroluminescent device results in UV light emission Since the excitonic binding energy in this direct bandgap material is of the order of 190 meV at room temperature, the electron-hole recombination and subsequent light emission at ~ 380 nm and ~ 387 nm is mediated by excitonic effects This opens up possibilities for UV optoelectronics on lattice-matched silicon substrates

Working towards our ultimate goal of developing CuCl p-n homojunction UV light-emitting devices on Si substrates, we have grown n-type CuCl thin films with a strong (111) crystalline orientation by co-evaporation of CuCl and $ZnCl_2$ powders Both excitonic and biexcitonic emissions are detected by low temperature photoluminescence measurements A strong room temperature Z_3 free exciton emission occurs at ~ 385nm for both photoluminescence and cathodoluminescence for doping levels up to a nominal 3 mole % $ZnCl_2$ co-evaporation indicating that at these doping levels, optical properties are not adversely affected A minimum resistivity of 34Ωcm was recorded using a four-point probe, which represents a reduction in resistivity by a factor of ~10 compared to the undoped samples The choice of metal contacts to CuCl is limited by the reactivity of CuCl with many metals such as Al, Ti, Ni and Ga Using Cu-Au evaporated metal contacts, annealed at 150°C for 5 minutes, linear IV characteristics have been measured in the range of ±4V for Zn-doped CuCl samples This enabled room-temperature Hall effect measurement on samples doped with a nominal 2-3 mole % $ZnCl_2$ The average net donor concentration was measured as ~9 x 10^{14}cm^{3} and ~1 x 10^{16}cm^{3} for samples doped with a nominal 2 and 3 mole % $ZnCl_2$, respectively As the electron carrier concentration increased, the mobility decreased For samples nominally doped with 2 and 3 mole % $ZnCl_2$, we measured average mobilities of 45 cm^{2}v^{1}s^{1} and 29 cm^{2}v^{1}s^{1}, respectively

This work has proven that γ–CuCl on Si is a promising novel material system for future wide-band gap photonic devices compatible with current electronic technology In the next stage of the project a number of key areas need to be addressed including the growth, doping, electrical characterisation and development of light-emitting devices

The simple evaporation growth process used in this work resulted in polycrystalline CuCl films on Si substrates Single crystal CuCl films on Si and GaAs have been reported by using a molecular beam epitaxy growth technique [56] Liquid phase epitaxy (LPE) can also be used to grow a layer of single crystal semiconductor material on a substrate as follows (1) heat a charge composed of a semiconductor material and a solvent to melt the charge and form a solution of the semiconductor material in the solvent, (2) heat the substrate to a lower temperature than the solution where the temperature difference is quite small, (3) bring the substrate into contact with the solution, (4) cool the solution and substrate at the same rate to deposit a layer of semiconductor material onto the substrate, (5) remove the substrate from contact with the solution after a predetermined interval A new LPE growth system has been recently acquired by DCU In this work, we have learned that the growth temperature must be kept below 250°C to prevent a CuCl-Si reaction Therefore addition of a second salt to the melt will be used to depress the melting point of CuCl Candidate growth melts include KCl, $SrCl_2$ and $BaCl_2$ (e g a 60-80% CuCl – 40-20% KCl solution has a $T_m < 200^{\circ}C$)

Our simple test electroluminescence device structure was used to demonstrate UV light emission from the CuCl-Si material system However, as the top Au electrode was not transparent, the intensity of the output was rather low The efficiency of this device could be improved by using a transparent electrode such as indium tin oxide (ITO) or ZnO Al An improved optical output could allow for further characterisation such as time- and voltage-dependent electroluminescent measurements

We have shown that the n-type doping of CuCl is possible by co-evaporation with $ZnCl_2$ Hall effect measurements were performed at room temperature, however a temperature dependent Hall study was prevented due to problems with the electrical contacts Although linear IV characteristics were achieved with Cu-Au contacts, the specific contact resistance which is commonly used as an indication of the quality of Ohmic contacts [208] was not measured A more detailed study of electrical contacts will be pursued in the future

The ability to dope CuCl p-type would enable us to fabricate CuCl p-n homojunctions Radio frequency (RF) magnetron sputtering is a plasma based PVD technique that is readily integratable into a manufacturing process, is robust and well defined, and offers a high degree of process flexibility enabling a significant degree of control over material fluxes to the substrate surface and overall film growth kinetics Recent work in our research group on the use of substrate biasing in RF sputtering of CuCl indicates that the copper content in γ-CuCl can be controlled by the substrate bias It is well known that the Cu halides tend to develop Cu vacancies [113,120] These Cu vacancies are associated with acceptors and the Cu halides tends to be p-type By controlling the Cu vacancy content, via substrate biasing, we may be able to control the p-type doping of CuCl Additionally, the use of $CuCl_2$ and Cu powder mixtures for novel sputter targets could vary the Cu vacancy density, thus impacting on p-type doping

N-type doping of CuCl may also be achieved by RF sputtering using reactive sputter procedures From the information gained by $CuCl/ZnCl_2$ co-evaporation, the use of Zn is one obvious choice with other possibilities including Fe, Co and Ni Finally, a co-sputtering chamber configuration could enable uninterrupted and *in situ* capping of the CuCl layers by depositing films with SiN_x content in order to eliminate air/moisture degradation of the CuCl layer This will facilitate the final aim of growing and testing an integrated p-n junction structure

References

1 K Itaya, M Onomura, J Nishino, L Sugiura, S Saito, M Suzuki, J Rennie, S Numoue, M Yamomoto, H Fujimoto, Y Kokubun, Y Ohna, G Hatakoshi and M Ishikawa, *Jpn J Appl Phys Part 2*, **35**, L1315 (1996)

2 E Monroy, F Calle, J L Pau, E Muñoz, F Omnès, B Beaumont and P Gibart, *J Cryst Growth*, **230**, 537 (2001)

3 X-L Guo, H Tabata, T Kawai, *J Crystal Growth* **223**, 135 (2001)

4 D C Look, B Claflin, *phys stat sol (b)* **241**, 624 (2004)

5 B Metzger, *Compound Semiconductor*, **57**, (2001)

6 O Ambacher, “Growth and applications of III-Nitrides”, *J Phys D Appl Phys* **31** 2653 (1998)

7 Usui, H Sunakawa, A Sakai and A A Yamaguchi, *Jpn J Appl Phys Part 2*, **36**, L899 (1997)

8 Marchand, X U Wu, J P Ibbetson, P T Fini, P Kozodoy, S Keller, J S Speck, S P DenBaars and U K Mishra, *Appl Phys Lett*, **73**, 747 (1998)

9 T Mukai, K Tadekawa and S Nakamura, *Jpn J Appl Phys* **37**, L839 (1998)

10 S Nakamura, M Senoh, N Iwasa, S -I Nagahama, T Yamada and T Mukai, *Jpn J Appl Phys* **34**, L1332 (1995)

11 S Nakamura, *Mater Res Soc Internet J Nitride Semicond Res* **2**, 5, (1997)

12 G E Bulman, K Doverspike, S T Sheppard, T W Weeks, H S Kong, H M Dieringer, J A Edmond, J D Brown, J T Swindell and J F Schetzena, *Electron Lett* **33**, 1556 (1997)

13 S Nakamura, M Senoh, S Nagahama, N Iwasa, T Yamada, T Matsushita, H Kiyoku, Y Sugimoto, T Kozaki, H Umemoto, M Sano and K Chocho, *Appl Phys Lett*, **72**, 211 (1998)

14 T Zheleva, O -H Nam, M D Bremser and R F Davis, *Appl Phys Lett* **71**, 2472 (1997)

15 J A Freitas, O -H Nam, R F Davis, G V Saparin and S K Obyden, *Appl Phys Lett*, **72**, 2990 (1998)

16 X Li, S G Bishop and J J Coleman, *Appl Phys Lett*, **73**, 1179 (1998)

17 Kozodoy, J P Ibbetson, H Marchand, P T Fini, S Keller, S P Den Baars, J S Speck and U K Mishra, *Appl Phys Lett*, **73**, 975 (1998)

18 C Sasaoka, H Sumakawa, A Kimura, M Nido, A Usui and A Sakai, *J Cryst Growth*, **189/190**, 61 (1998)

19 H Marchand, N Zhang, L Zhao, Y Golan, S J Rosner, G Girolami, P T Fini, J P Ibbetson, S Keller, S DenBaars, J S Speck and U K Mishra, *MRS Internet J Nitride Semicond Res*, **4**,2 (1999)

20 S J Chang, Y C Lin, Y K Su, C S Chang, T C Wen, S C Shei, J C Ke, C W Kuo, S C Chen, C H Liu, *Solid State Elec* **47**, 1539 (2003)

21 K Tadatomo, H Okagawa, Y Ohuchi, T Tsunekawa, T Jyiuichi, Y Imada, M Kato, H Kudo, T Taguchi, *phys stat sol (a)* **188**, 121 (2001)

22 T S Zheleva, S A Smith, D B Thomson, K J Linthicum, P Rajagopal and R F Davis, *J Electron Mater*, **28**, L5 (1999)

23 Gehrke, K J Linthicum, D B Thomson, P Rajagopal, A D Batchelor and R F Davis, *MRS Internet J Semicond Res*, **4S1**, G3 2 (1999)

24 S -I Nagahama, N Iwasa, M Senoh, T Matsushita, Y Sugimoto, H Kiyoku, T Kozaki, M Sano, H Matsumura, H Umemoto, K Chocho and T Maki, *Jpn J Appl Phys* **39**, L647 (2000)

25 S Guha and N A Bojarczuk, *Appl Phys Lett*, **72**, 415 (1998)

26 K S Stevens, M Kinniburgh and R Beresford, *Appl Phys Lett* **66**, 3518 (1995)

27 J L Pau, E Monroy, M A Sanchez-Garcia, E Calleja, E Muñoz, *Mater Sci Eng* **B93**, 159 (2002)

28 M Cervantes-Contreras, M Lopez-López, , M Melendez-Lira, M Tamura, M A Vidal, *Thin Solid Films*, **433**, 68 (2003)

29 J-R Gong, M-F Yeh, Y-L Tsai, *Optical Materials* **24**, 615 (2004)

30 Yamamoto, T Yamauchi, T Tanikawa, M Sasase, B K Ghosh, A Hashimoto and Y Ito, *J Cryst Growth*, **261**, 266 (2004)

31 S Tanaka, Y Honda, N Kameshiro, R Iwasaki, N Sawaki, T Tanji, M Ichihashi, *J Cryst Growth*, **260**, 360 (2004)

32 Osinsky, S Gangopadhyay, J W Wang, R Gaska, D Kuksenkov, H Temkin, I K Shmagin, Y C Chang, J F Muth and R M Kolbas, *Appl Phys Lett* **72**, 551 (1998)

33 Watanabe, T Takeuchi, K Hirosawa, H Amano, K Hiramatsu and I Akasaki, *J Cryst Growth*, **128**, 391 (1993)

34 T L Chu, *J Electrochem Soc*, **118**, 1200 (1971)

35 H M Manasevit, F M Erdmann and W I Simpson, *J Electrochem Soc*, **118**, 1864 (1971)

36 T Takeiuchi, H Amano, K Hiramatsu, N Sawaki and I Akasaki, *J Cryst Growth* **115**, 634 (1991)

37 A J Steckl, J Devrajan, C Tran and R A Stall, *Appl Phys Lett* **69**, 2264 (1996)

38 T Lei, M Fanciulli, R J Molnar and T D Moustakas, *Appl Phys Lett* **59**, 944 (1991)

39 P Kung, A Saxler, X Zhang, D Walker, T C Wang, I Ferguson and M Razeghi, *Appl Phys Lett*, **66**, 2958 (1995)

40 M Godlewski, J P Bergman, B Monemar, U Rossner and A Barski, *Appl Phys Lett*, **69**, 2089 (1996)

41 J W Wang, C J Sun, Q Chen, M Z Anwar, M A Khan, S A Nikishin, G A Seryogin, A V Osinsky, L Chernyak, H Temkin, C Hu and S Mahajan, *Appl Phys Lett* **69**, 3566 (1996)

42 N P Kobayashi, P D Dapkus, W J Choi, A E Bond, X Zhang and D H Rich, *Appl Phys Lett*, **71**, 3569 (1997)

43 Y Nakada, I Aksenov and H Okumura, *Appl Phys Lett*, **73**, 827 (1998)

44 Y Honda, N Kameshiro, M Yamaguchi, N Sawaki, *J Cryst Growth*, **242**, 82 (2002)

45 F Schulze, A Dadgar, J Blasing, T Hempel, A Diez, J Christen and A Krost, *J Cryst Growth* **289**, 485 (2006)

46 A Mills, *III-Vs Review* **19**, 25 (2006)

47 Wyncke and F Brehat, *J Phys Condens Matter*, **12**, 3461 (2000)

48 WebElements Periodic Table, [online] Available from <webelements com>[accessed 12 August 2005]

49 C Schwab and A Goltzené, *Prog Crystal Growth Charact*, **5**, pp 233-276 (1982)

50 P N Butcher and D Cotter, "The elements of nonlinear optics", Cambridge University Press, pp 7-8 (1990)

51 Landolt-Bornstein, "Intrinsic properties of group IV elements and III-V, II-VI and I-VII compounds," –Berlin, New York Springer-Verlag, (1987)

52 S Tanaka, M Kamada, *J Electron Spectroscopy & Related Phenomena* **88-91**, pp 689-693 (1998)

53 T H K Barron, J A Birch and G K White, *J Phys C Solid State Phys* **10**, 1617 (1977)

54 J C Phillips, *Rev Mod Phys*, **42**, 317 (1970)

55 S Hull and D A Keen, *Phys Rev B* **50**, 5868 (1994)

56 N Nishida, K Saiki and A Koma, *Surf Sci* **324**, 149 (1995)

57 I P Kaminow and E H Turner, *Physical Review B* **5**, pp 1564-1577 (1972)

58 NIST Chemistry Webbook, [online] Available from < webbook nist gov> (accessed 24 April 2006)

59 D C Reynolds, R J Almassy, C W Litton, G L Koos, A B Kunz and T C Collins, *Phys Rev Lett* **44**, 204 (1980)

60 J J O'Connor, M A DiPietro, A F Armington, B Rubin, *Nature*, **212**, 68 (1966)

61 F Armington and J J O'Connor, *Mat Res Bull*, **2**, 907 (1967)

62 J J O'Connor and A F Armington, *J Cryst Growth*, **1**, 327(1967)

63 F Armington and J J O Connor, *J Cryst Growth*, **3,4**, 367 (1968)

64 D S Robertson, O Jones, *Brit J Appl Phys* **17**, 1043 (1966)

65 M Soga, R Imaizumi, Y Kondo, T Okabe, *J Electrochem Soc* **114**, 388 (1967)

66 J Rivera, L A Murray, P A Hoss, *J Cryst Growth* **1**, 171 (1967)

67 Y Kaifu, Y Kawate, S Nakanishi, I Niwa, K Nakazawa and M Koba, *J Phys Soc Japan*, **22,** 517 (1967)

68 W R Wilcox, R A Corley, *Mat Res Bull* **2,** 571 (1967)

69 B Chase, W R Wilcox and J R Teviotdale, *J Appl Phys* , **39,** 3577 (1968)

70 Perner, *J Cryst Growth*, **6,** 86 (1969)

71 J Kvapil and B Perner, *J Cryst Growth*, **8,** 162 (1971)

72 F Sterzer, D Blattner and S Miniter, *J Opt Soc Amer* , **54,** 62 (1964)

73 S G Parker, J E Pinnell, *J Electrochem Soc* , **117,** 107 (1970)

74 T Inoue, M Kuriyama and H Komatsu, *J Cryst Growth* **112,** 531 (1991)

75 Yanase and Y Segawa, *Surf Sci* **329,** 219 (1995)

76 Yanase and Y Segawa, *Surf Sci* , **367,** L1 (1996)

77 Yanase and Y Segawa, *Surf Sci* **357-358,** 885 (1996)

78 Q Guo, L Gui and N Wu, *Appl Surf Sci* , **99,** 229 (1996)

79 A Goldmann, *phys stat sol (b)*, **81,** 9 (1977)

80 Gobel, T Ruf, M Cardona, C T Lin, J Wrzesinski, M Steube, K Reimann, J C Merle and M Joucla, *Phys Rev B* **57,** 15183 (1998)

81 M Cardona, *Phys Rev* **129,** 69 (1963)

82 Goldmann, J Tejeda, N J Shevchik and M Cardona, *Phys Rev B* **10,** 4388 (1974)

83 M Nakayama, A Soumura, K Hamasaki, H Takeuchi and H Nishimura, *Phys Rev B*, **55,** 10099 (1997)

84 G Suyal, M Mennig and H Schmidt, *J Mater Chem* **12,** 3136 (2002)

85 S D Kramer and N Bloembergen, *Phys Rev B* **14,** 4654 (1976)

86 N Garro, A Cantarero, M Cardona, T Ruf, A Gobel, C Lin, K Reimann, S Rubenacke and M Steube, *Solid State Comm* **98,** 27 (1996)

87 T Goto, T Takahashi and M Ueta, *J Phys Soc Japan* **24,** 314 (1968)

88 Y Kaifu and T Komatsu, *phys stat sol (b)* **48,** K125 (1971)

89 Y Takubo, T Koda and M Mitani, *J Lumin* , **4,** 249 (1971)

90 M Nakayama, H Ichida and H Nishimura, *J Phys Condens Matter*, **11,** 7653 (1999)

91 Y Mimura, K Edamatsu and T Itoh, *J Lumin* **66 & 67,** 401 (1996)

92 S Yano, T Goto, T Itoh and A Kasuya, *Phys Rev B* **55,** 1667 (1997)

93 Hanamura, *Phys Rev B* **37,** 1273 (1998)

94 Y Masumoto and S Ogasawara, *J Lumin* , **87-89**, 360 (2000)

95 M Ikezawa and Y Masumoto, *J Lumin* **87-89**, 482 (2000)

96 J Zhao, M Ikezawa, A V Fedorov and Y Masumoto, *J Lumin* **87-89**, 525 (2000)

97 M Haselhoff, K Reimann and H J Weber, *J Cryst Growth* **196,** 135 (1999)

98 H Kurisu, K Nagoya, N Nakayama, S Yamamoto and M Matsuura, *J Lumin* **87-89**, 390 (2000)

99 J Sasai, K Tanaka and K Hirao, *Scripta mater* , **44,** 1225 (2000)

100 W Ungier and P Janiszewski, *Solid State Comm* , **129**, 701 (2004)

101 V Kutzer, B Lummer, R Heitz, A Hoffmann, I Broser, E Kurtz and D Hommel, *J Cryst Growth* **159**, 776 (1996)

102 H J Ko, Y F Chen, T Yao, K Miyajima, A Yamamoto and T Goto, *Appl Phys Lett* , **77**, 537 (2000)

103 Hanamura, *Solid State Comm* **38**, pp 939-942 (1981)

104 R Levy, J Y Bigot, B Honerlage, F Tomasini and J B Grun, *Solid State Comm* **48**, pp 705-708, (1983)

105 N Peyghambarian, H M Gibbs, M C Rushford and D A Weinberger, *Phys Rev Lett* , **51**, pp 1692-1695 (1983)

106 N Peyghambarian, L L Chase and A Mysyrowicz, *Phys Rev B*, **27**, 2325 (1983)

107 K L Shaklee, R F Leheny and R E Nahory, *Phys Rev Lett* **26**, 888 (1971)

108 M Ojima, Y Oka, T Kushida and S Shionoya, *Solid State Comm* **24**, 845 (1977)

109 Y Masumoto, T Kawamura and K Era, *Appl Phys Lett* **62**, 225 (1993)

110 Y Kagotani, K Miyajima, G Oohata, S Saito, M Ashida, K Edamatsu and T Itoh, *J Lumin* **112**, 113 (2005)

111 Oohata, Y Kagotani, K Miyajima, M Ashida, S Saito, K Edamatsu and T Itoh, *Physcia E*, **26**, 347 (2005)

112 K Reimann and St Rubenacke, *J Appl Phys* , **76**, 4897 (1994)

113 J B Wagner, C Wagner, *J Chem Phys* **26**, 1597 (1957)

114 A V Joshi and J B Wagner Jr , *J Electrochem Soc Electrochem Sci Tech* **122**, 1071 (1975)

115 N J Parada and G W Pratt Jr , *Phys Rev Lett* **22**, 180 (1969)

116 Bridges, G Davies, J Robertson and A M Stoneham, *J Phys Condens Matter* **2**, 2875 (1990)

117 T Matsui and J B Wagner Jr , *J Electrochem Soc Solid-State Sci Tech* **124**, 610 (1977)

118 T Jow and J B Wagner Jr , *J Electrochem Soc Solid-State Sci Tech* **126**, 1963 (1979)

119 J A Schmidt, G M Lescano, M R Prat and J A Dristas, *Solid State Ionics* **112**, 63 (1998)

120 P Knauth, Y Massiani, M Pasquinelli, *phys stat sol (a)* **165**, 461 (1998)

121 J -L Seguin, M Bendahan, G Lollmun, M Pasquinelli, and P Knauth, *Thin Solid Films* **323**, 31 (1998)

122 P Lauque, M Bendahan, J -L Seguin, M Pasquinelli and P Knauth, *J European Ceramic Soc* **19**, 823 (1999)

123 J -L Seguin, M Bendahan, P Lanque, C Jacolin, M Pasquinelli and P Knauth, *Sensors and Actuators* **74**, 237 (1999)

124 L G Carpenter, "Vacuum Technology, an Introduction", 2nd edition Adam Hilger Ltd , Bristol (1983) pp 18-20

125 Jenny Pickworth Glusker and Kenneth N Trueblood, "Crystal Structure Analysis A Primer", 2nd edition, Oxford University Press, (1985)

126 Bruker Advanced X-Ray Solutions, D8 X-Ray Diffractometer User's Manual Volume I, pp 1-2

127 D Keith Bowen and Brian K Tanner, "X-Ray Metrology in Semiconductor Manufacturing", CRC Press Taylor & Francis Group 2006, pp 8-9

128 J -R Duclère, R O'Haire, A Meaney, K Johnston, I Reid, G Tobin, J -P Mosnier, M Guilloux-Viry, E McGlynn and M O Henry, *J Mater Sci Mater Electron* **16**, 421 (2005)

129 C V Raman, *Ind J Phys* **2**, 387 (1928)

130 [online] Available from <http //allserv rug ac be/~lmoens/Raman/theory htm> (Accessed on 15th May 2005)

131 Sidney Perkowitz, "Optical Characterization of Semiconductors, Infrared, Raman and Photoluminescence Spectroscopy", Academic Press 1993, pp 23

132 John R Ferraro and Kazuo Nakamoto, "Introductory Raman Spectroscopy", Academic Press 1994, pp 12, 15

133 Ingrid de Wolf, *Semicond Sci Technol* **11**, pp 139-154 (1996)

134 Takahashi J-I and Makino T , *J Appl Phys* **63**, pp 87-91 (1988)

135 European Commission, Raman and Luminescence Spectroscopy for Microelectronics, Catalogue of optical and physical parameters "Nostradamus" project SMT4-CT-95-2024

136 Aspnes D E and A A Studna, *Phys Rev B* **27**, (2) pp 985-1008 (1983)

137 G Rech, J Lee, E B Norman, R -M Larimer and L Guthrie [online] Available from <http //ie lbl gov/xray/> (accessed 04/05/2006)

138 "Scanning Electron Microscope and Energy Dispersive –Ray Analyser", Aine Allen, Course notes (2003)

139 B G Yacobi and D B Holt, *J Appl Phys*, **59**, R1 (1986)

140 J I Pankove, "Optical Processes in Semiconductors", Dover Publications, Inc (1971), pp 14-16

141 Schroder, Dieter K, "Semiconductor material and device characterization", 2nd edition New York John Wiley and Sons, pp 623-625 (1998)

142 M Grasserbauer and H W Werner, "Analysis of Microelectronic Materials and Devices", John Wiley & Sons, pp 232 (1991)

143 Gatan U K Operator Handbook (2001)

144 K Kanaya and S Okayama, *J Phys D Appl Phys* 5, 43 (1972)

145 Casino [online] Available from <http //www gel usherb ca/casino/> (accessed 5th May 2006)

146 P D Rack and P H Holloway, *Mater Sci Eng* **R21**, 171 (1998)

147 S Takata, T Minami and H Nanto, *J Lumin*, **40-41**, 794 (1988)

148 W Tang and D C Cameron, *Thin Solid Films*, **238**, 83 (1994)

149 J I Pankove, "Optical Processes in Semiconductors", Dover Publications, Inc (1971), pp 34

150 Schroder, Dieter K, *Semiconductor material and device characterization*, 2nd edition New York John Wiley and Sons, pp 2-22 (1998)

151 L J van der Pauw, *Philips Res Rep*, **13**, pp 1-9 (1958)

152 "Analysis of Microelectronic Materials and Devices", M Grasserbauer and H W Werner, John Wiley & Sons, pp 881-882 (1991)

153 A A Ramadan, R D Gould and A Ashour, *Thin Solid Films* **239**, pp 272-275 (1994)

154 D K Schroder, "Semiconductor Material and Device Characterization", Wiley-Interscience, New York, 1990, pp 30-32

155 [online] <http //chem ch huji ac il/~eugenik/history/hall html> (accessed on 04/05/06)

156 D K Schroder, "Semiconductor Material and Device Characterization", Wiley-Interscience, New York, 1990, pp 73-76

157 G E Stillman and C M Wolfe, *Thin Solid Films* **31**, 69 (1976)

158 E H Rhoderick and R H Williams, "Metal-Semiconductor Contacts", 2nd edition, Oxford University Press (1988) pp 11-15

159 E H Rhoderick and R H Williams, "Metal-Semiconductor Contacts", 2nd edition, Oxford University Press (1988) pp 66-68

160 D C Look, "Electrical Characterization of GaAs Materials and Devices", John Wiley & Sons (1989)

161 D K Schroder, “Semiconductor Material and Device Characterization”, Wiley-Interscience, New York, 1990, pp 101-104

162 Bruker Advanced X-ray Solutions, powder diffraction files, (www icdd com)

163 C T Lin, E, Schonherr, A Schmeding, T Ruf, A Gobel, M Cardona, *J Cryst Growth* **167**, pp 612-615 (1996)

164 P J McNally, R Rantamaki, T Tuomi, A N Danilewsky, D Lowney, J W Curley and P A F Herbert, *IEEE Transactions on Components and Packaging Technologies*, **24**, pp 76-83 (2001)

165 Berkeley Lab, X-ray interactions with matter [online] Available from <http //cindy lbl gov/optical_constants/> (Accessed on 20th May 2004)

166 X-ray data booklet, Technical and Electronic Information Department, Lawrence Berkeley Laboratory, Berkeley, California 94720, (2001)

167 B D Cullity, in “Elements of X-ray Diffraction” 2nd Edition, (Reading, Mass Addison-Wesley, 1978) p 144, 543

168 B-H Hwang, *J Phys D Appl Phys* , **34**, pp 2469-2474 (2001)

169 F Boulc’h, M -C Schoulder, P Donnadieu, J -M Chaix and E Djurado, *Image Anal Sterol* **20**, 157 (2001)

170 I P Kaminow and E H Turner, *Phys Review B* **5**, pp 1564-1578 (1972)

171 M L Shand, H D Hochheimer, M Krauzman, J E Potts, R C Hanson and C T Walker, *Phys Review B* **14**, pp 4637-4645 (1972)

172 A Gobel, T Ruf, C T Lin, M Cardona, J C Merle and M Joucla, *Phys Review B* **56**, pp 210-220 (1997)

173 M Krauzmann, R M Pick, H Poulet, G Hamel and B Prevot, *Phys Review Lett* **33**, pp 528-530 (1974)

174 H D Hochheimer, M L Shand, J E Potts, R C Hanson and C T Walker, *Phys Review B* **14**, pp 4630-4636 (1976)

175 G Weber, M Gourgouillon, D Viale, B Gillot and P Barret, *Reactivity of Solids* **6**, 75 (1988)

176 G Weber, D Viale H Souha, B Gillot and P Barret, *Solid State Ionics*, **32/33**, 250 (1989)

177 H Souha, F Bernard, E Gaffet and B Gillot, *Thermochimica Acta*, **351**, 71 (2000)

178 A R Miedema, *Philips Technical Review* **36**, 217 (1976)

179 McGraw-Hill Handbooks, "Lange's Handbook of Chemistry", 15th edition by John A Dean, pp 540 (1999)

180 J Sasai, K Tanaka and K Hirao, *Scrpta mater* **44**, 1225 (2001)

181 F O Lucas, L O'Reilly, G Natarajan, P J McNally, S Daniels, D M Taylor, S William, D C Cameron, A L Bradley and A Miltra, *J Cryst Growth* **287**, 112 (2006)

182 J Fryar, E McGlynn, M O Henry and J -P Mosnier, *Nanotechnology* **16**, 2625 (2005)

183 E McGlynn, J Fryar, G Tobin, C Roy, M O Henry, J -P Mosnier, E de Posada, J G Lunney, *Thin Solid Films* **458**, 330 (2004)

184 T Koda, T Murahashi, T Mitani, S Sakoda, and Y Onodera *Phys Rev B* **5**, 705 (1972)

185 P M Ratheesh Kumar, C Sudha Kartha, K P Vijayakumar, T Abe, Y Kashiwaba, F Singh and D K Avasthi, *Semicond Sci Technol* **20**, 120 (2005)

186 D K Shuh and R S Williams, *Phys Rev B* **44**, 5827 (1991)

187 M Certier, C Wecker, and S Nikitine, *J Phys Chem Solids* **30**, 2135 (1969)

188 J I Pankove, "Optical Processes in Semiconductors", Dover Publications, Inc (1971), pp 124

189 A Mitra, L O'Reilly, O F Lucas, G Natarajan, A L Bradley, P J McNally, S Daniels , D C Cameron, A Reader, and M Martinez-Rosas, *Submitted to Journal of Luminescence*

190 J Zhao, L Hu, Z Wang, Z Wang, H Zhang, Y Zhao, X Liang, *J Cryst Growth* **280**, 455 (2005)

191 D -W Kim, C -R Lee, *J Cryst Growth* **286**, 235 (2006)

192 Y Masumoto, S Okamoto, S Katayangi, *Phys Rev B* **50**, 18658 (1994)

193 H J Ko, Y F Chen, T Yao,, K Miyajima, A Yamamoto and T Goto , *Appl Phys Lett* **77**, 537 (2000)

194 H -C Lin, S Senanayake, K -Y Cheng, M Hong, J Raynien Kwo, B Yang and J P Mannaerts, *IEEE Transactions on Electron Devices* **50**, 880 (2003)

195 E H Rhoderick and R H Williams, "Metal-Semiconductor Contacts", 2nd edition, Oxford University Press (1988) pp 48

196 J N Koster, *Crsyt Res Technol* **34**, 1129 (1999)

197 Y -H Lee, B -K Ju, D -H Kim and M -H Oh, *IEEE Trans Electron Devices* **48**, 653 (2001)

198 Madelung, Semiconductor Data Handbook

199 CRC Handbook of Chemistry and Physics 84th edition, Boca Raton, Florida CRC press, 2004, p 6-70

200 E H Rhoderick and R H Williams, "Metal-Semiconductor Contacts", 2nd edition, Oxford University Press (1988) pp 48

201 D C Look, B Claflin, Ya I Alivov and S J Park, *phys stat sol (a)* **201**, 2203 (2004)

202 D K Bowen, B K Tanner, "High Resolution X-ray Diffractometry and Topography", Taylor & Francis, London, 1998, p 57

203 H Nagai, *J Appl Phys* **45**, 3789 (1974)

204 CRC Handbook of chemistry and physics, 84th edition, p 4-95

205 L O'Reilly, Gomathi Natarajan, O F Lucas, P J McNally, S Daniels, D C Cameron, A Reader, A Mitra, M Martinez-Rosas and A L Bradley, *J Appl Phys* **98**, (2005)

206 P M Ratheesh Kumar, C Sudha Kartha, K P Vijayakumar, T Abe, Y Kashiwaba, F Singh and D K Avasthi, *Semicond Sci Technol* **20**, (2005) 120

207 R Stanley Williams and D K Shuh, *J Vac Sci Technol* **A6**, 1950 (1988)

208 K Ip, G T Thaler, Hyucksoo Yang, Sang Youn Han, Yuanjie Li, D P Norton, S J Pearton, Soowhan Jang and F Ren, *J Cryst Growth* **287**, 149 (2006)

Appendix A

Characterisation of Si-SiGe Heterostructures using Micro-Raman Spectroscopy and Synchrotron X-Ray Topography

A 1 Introduction

Heteroepitaxy of Ge on Si is a research topic of significant technological importance for the fabrication of novel electronic and optoelectronic devices However in heteroepitaxy of Ge on Si, the 4% lattice mismatch between the two materials introduces defects like misfit dislocations, surface roughness, and compositional non-homogeneity that affect device performance [a] The combination of a substrate and a fully or partially relaxed buffer layer can be considered as a virtual substrate Compositionally graded SiGe layers are designed to accommodate the lattice mismatch between the underlying Si substrate and the overlying active epilayers High quality strain-relaxed $Si_{1-x}Ge_x$ virtual substrates offer a new degree of freedom in strain and band structure engineering for devices as they can be used to create a tensile strain in Si overlayers [b] A tensile strain in the Si device region leads to improvements in electrical properties such as enhanced carrier mobility and it is expected that within the next few years, strain engineering to enhance CMOS operating speeds will be almost universal [c] The ability to assess parameters such as Ge content and strain in a fast and efficient way is essential to the development of SiGe technology Micro-Raman spectroscopy (section 2 3) has proven to be an effective, convenient and non-destructive measurement method for the stress of semiconductor epitaxial structures [d] In this section I will present the results of a study of Si-SiGe heterostructures using synchrotron x-ray topography (section A 2) and micro-Raman spectroscopy

The Si-SiGe epitaxially grown samples were prepared in Southampton University using a low pressure chemical vapour deposition (LPCVD) system [o] It is nominally graded 0-30% in germanium composition, with grading at 15%/μm A schematic diagram is shown in fig A 1 below

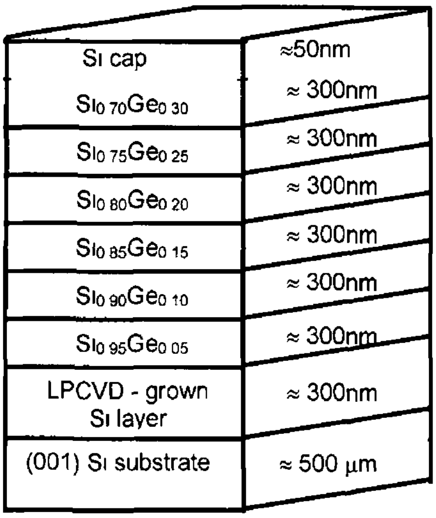

Fig A 1 Schematic diagram of Si-SiGe virtual substrate heterostructure

A 2 White beam Synchrotron X-ray Topography

X-ray topography (XRT) is a non-destructive imaging technique based on the difference in reflecting power between perfect and distorted parts of a crystal It can provide detailed information on the defect distribution in crystals It is sensitive to strain fields extending over several microns and is therefore used mainly for the study of dislocations, planar defects, stacking faults, domain walls in ferromagnetic materials, growth defects or large precipitates [e,f,g]

When a single crystal is immersed in a white x-ray beam, the lattice planes (*hkl*) can select a wavelength from the continuous spectrum which will result in diffraction in accordance with Bragg's law $2d_{hkl}\sin\theta = n\lambda$, where d_{hkl} is the interplanar spacing of the (*hkl*) lattice planes, θ is half the scattering angle and n is an integer In this way various reflections occur at specific angles and the resulting Laue pattern are recorded using x-ray films Each of these topographs contains detailed sample information Localised imperfections within the sample modify the diffraction condition resulting in an intensity variation within the topographs It is not the defect itself which is being imaged, rather it is the strains induced by the defect that modify the Bragg condition with respect to the perfect sample regions which are evident in the topographic image

Different sample geometries such as back-reflection, transmission and grazing incidence can be used as described below to obtain a variety of information about the sample under investigation Large area back reflection topography (fig A 2) is used to examine highly absorbing samples It can characterise epitaxial layers or electronic devices on substrates with dominating defect structure

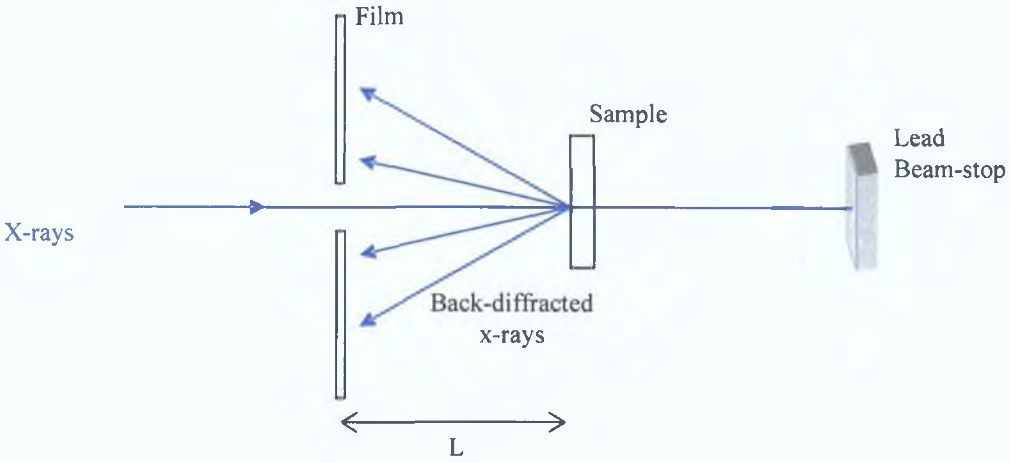

Fig. A.2 Experimental Set-up for Back-Reflection Topography

The typical spot size of a large area topograph is 2mm x 2mm. This geometry has been successfully used to characterise sapphire [h] and GaAs [i] samples as well as highly absorbing samples such as (Cd,Zn)Te [j]. Large area transmission topography (fig.A.3) can also be used to investigate the distribution of strain and dislocations, dislocation types and densities, and for a Burgers vectors analysis of dislocations [k].

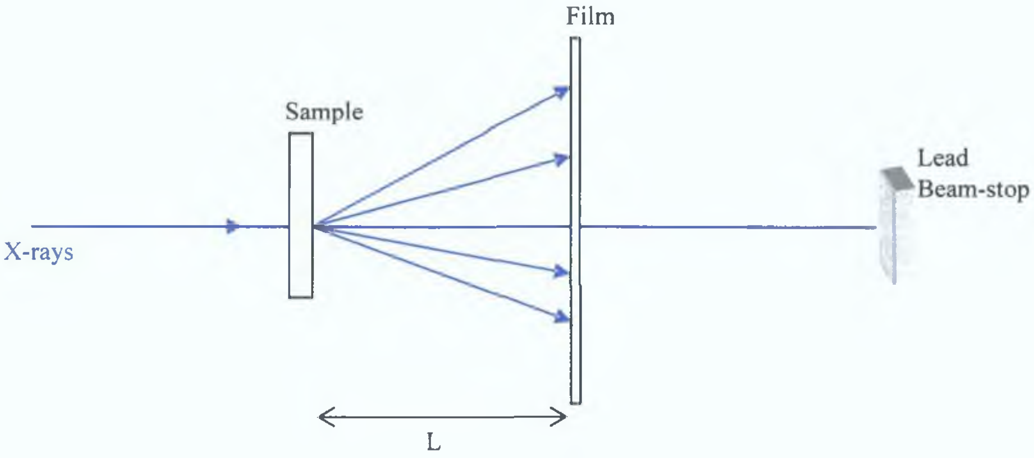

Fig. A.3 Experimental Set-up for Transmission Topography

Edge dislocations having a Burgers vector parallel to <110>, along with evidence of stacking faults and circular dislocations have been found in InAs epitaxial films grown by vapour-phase epitaxy using the large area transmission geometry [l]. Section transmission in which a long narrow beam (~4mm x 0.015mm) is used to acquire a cross section through the sample can be used to verify the crystal quality. Pendellösung fringes, which are typical of nearly perfect crystals [m] were present in the transmission section topographs of InSb epitaxial layers grown by MOVPE [n].

Grazing incidence topography (fig.A.4) can be applied for a wavelength dependent depth profile of defect and strain distributions by using a range of incident angles.

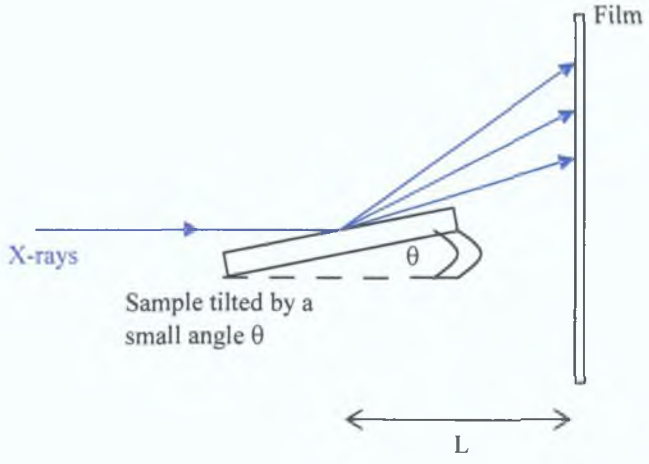

Fig. A.4 Experimental Set-up for Grazing Incidence Topography

As the condition for total internal reflection is approached, the penetration depth of the x-rays into the sample is of the order of nanometres. The work of McNally et *al.* [o,p]

established the use of a total reflection grazing geometry to analysis the surface roughness of a thin strained Si layer on a SiGe virtual substrate

The x-ray synchrotron topography measurements in this report were performed at two synchrotrons, HASYLAB-DESY and ANKA The Hamburger Synchrotronstrahlungslabor am Deutschen Elektronen-Synchrotron, (Hamburg, Germany), utilises the continuous spectrum of synchrotron radiation from the DORIS storage ring bending magnet The ring operates at positron energies of 4 45 GeV and at typical currents of 80-150 mA At the recently constructed Angstromquelle Karlsruhe, (ANKA, Karlsruhe, Germany) synchrotron light source, a small point source of 0 5×0 2 mm^2 at a bending magnet of the 2 5 GeV storage ring provides light with a characteristic wavelength of 2 Å [k] and typical beam currents of 100-200 mA

The topograph patterns are recorded on normal resolution Kodak Industrex SR film, grain size ~ 1μm, or high-resolution Slavich VRP-M x-ray films with a grain size of approximately 0 05μm

A 3 X-Ray Topography Results

An example of the Laue pattern produced from a Si-SiGe heterostructure grown on Si with (100) orientation using large area back reflection topography (LA-BRT) is shown in fig A 5

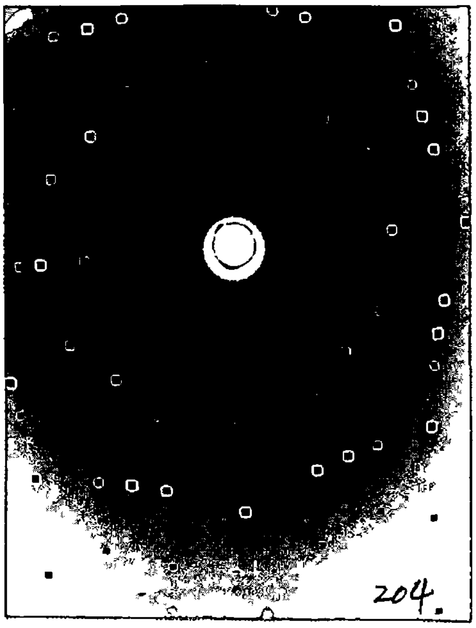

Fig A 5 Laue Pattern of a Si-SiGe Heterostructure on (001) Si substrate Each spot represents an x-ray topograph

Indexing of the diffraction pattern was achieved using a computer program called "Orient Express" [q] which makes it possible to orient a single crystal of known unit cell dimensions from a single Laue pattern The penetration depth t_p, at which the intensity of the outgoing reflected beam has dropped to e^{1} that of the incident beam due to absorption, was calculated using the kinematical approximation given by [r]

$$t_p = \frac{1}{\mu(\lambda)\left(\frac{1}{\sin\phi_i} + \frac{1}{\sin\phi_f}\right)}, \phi_i, \phi_f >> \phi_c$$

where $\mu(\lambda)$ is the wavelength –dependent linear absorption coefficient, ϕ_i is the incidence angle, ϕ_f is the exit angle, and ϕ_c is the critical angle of total reflection measured from the wafer surface

An example LA-BRT for reflection 117 of the Laue pattern is shown in fig A 6 The penetration depth of the x-rays at this reflection is 37 4μm Therefore the entire SiGe buffer layer is being imaged in this geometry The projection of the diffraction vector **g**, onto the plane of the recording film is indicated in the topograph

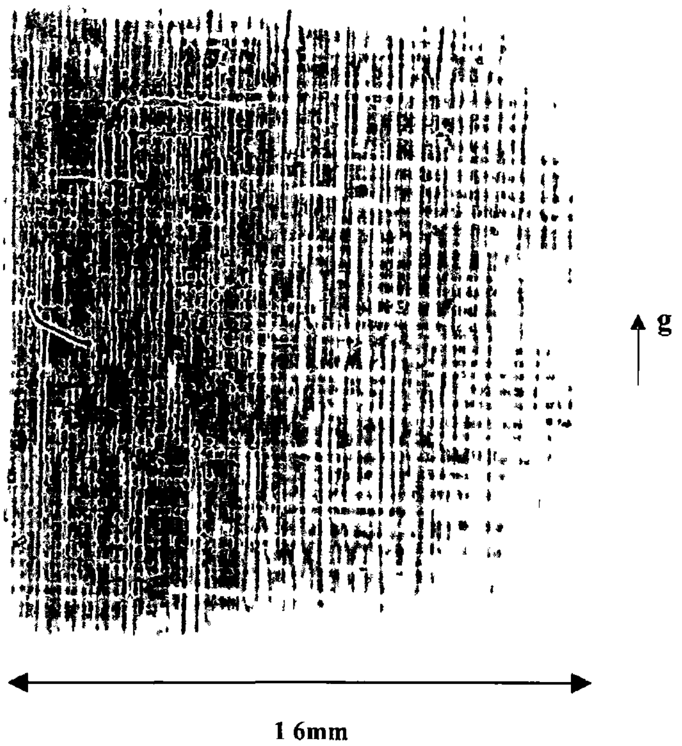

Fig A 6 Si-SiGe 3-525 LA-BRT Reflection 117 t_p=37 4μm

We see a well-defined crosshatched pattern with ridges running along two perpendicular <011> directions This is characteristic of misfit dislocations The presence of misfit dislocations indicates that there is strain relaxation in the SiGe buffer layers The dislocation density is ~ 1 4 x 10^5cm^2 The dislocation density, ρ, was calculated using the equation [h]

$$\rho = L / V$$

where V is the volume of the wafer exposed to the x-rays during the experiment and L is the total dislocation length in that volume V is calculated using the x-ray penetration depth and the experimental beam size

Changing the angle of incidence can vary the penetration depth of x-rays into the sample The general kinematical approach to the penetration depth calculation is no longer valid when ϕ_i and ϕ_f, the incidence angle and exit angle, respectively, approach ϕ_c, the critical angle of total reflection measured from the wafer surface In such a case t_p is calculated by [s],

$$t_p = \frac{\lambda}{4\pi\left(l_i + l_f\right)}$$

where

$$l_{i,f} = \frac{1}{\sqrt{2}}\left[\left(2\delta - \sin^2\phi_{i,f}\right) + \left\{\left(\sin^2\phi_{i,f} - 2\delta\right)^2 + \left(2\beta\right)^2\right\}^{1/2}\right]^{1/2}$$

In these two equations λ is the vacuum wavelength, $\beta = \frac{\lambda\mu}{4\pi}$, $\delta = \frac{\overline{\rho_e} e^2 \lambda^2}{2 m_e \varepsilon_0 \left(2\pi c\right)^2}$, where

$\overline{\rho_e}$ is the number of electrons per unit volume, m_e is the electron mass and e is the elementary charge, ε_0 is the vacuum permittivity and c is the velocity of light

Fig A 7 below shows a topographic image taken at a grazing angle of 1° Although the misfit dislocation pattern is still evident, the appearance is much rougher than for the back reflection topograph in fig A 6

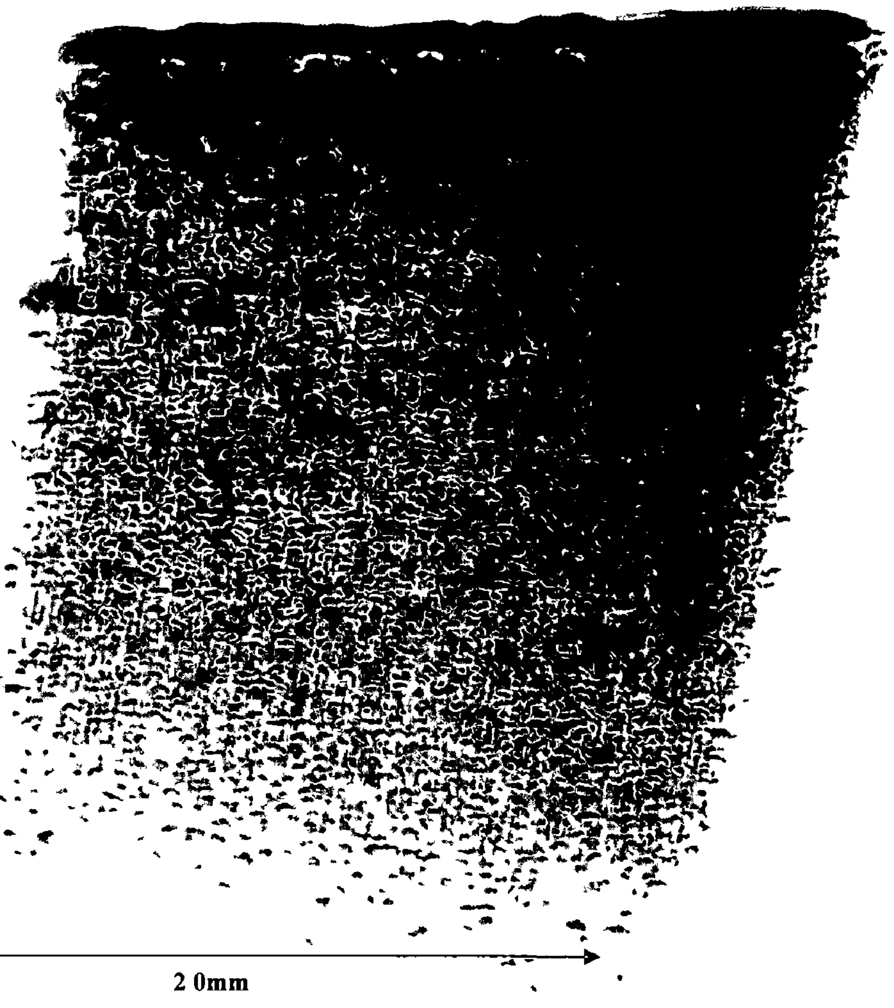

Fig A 7 Si-SiGe 3-525, Grazing Incidence 1°, Reflection 012

As the grazing angle is further decreased towards the critical angle, $\phi_c \sim 0\ 05^{\circ}$, at which total internal reflection occurs, the radiation penetrates only a few angstroms into the sample and we can obtain a detailed image of the surface layer as shown in fig A 8 Although the misfit dislocations are no longer visible at this point, the "bumpy" structure of the surface is related to the underlying misfit dislocations

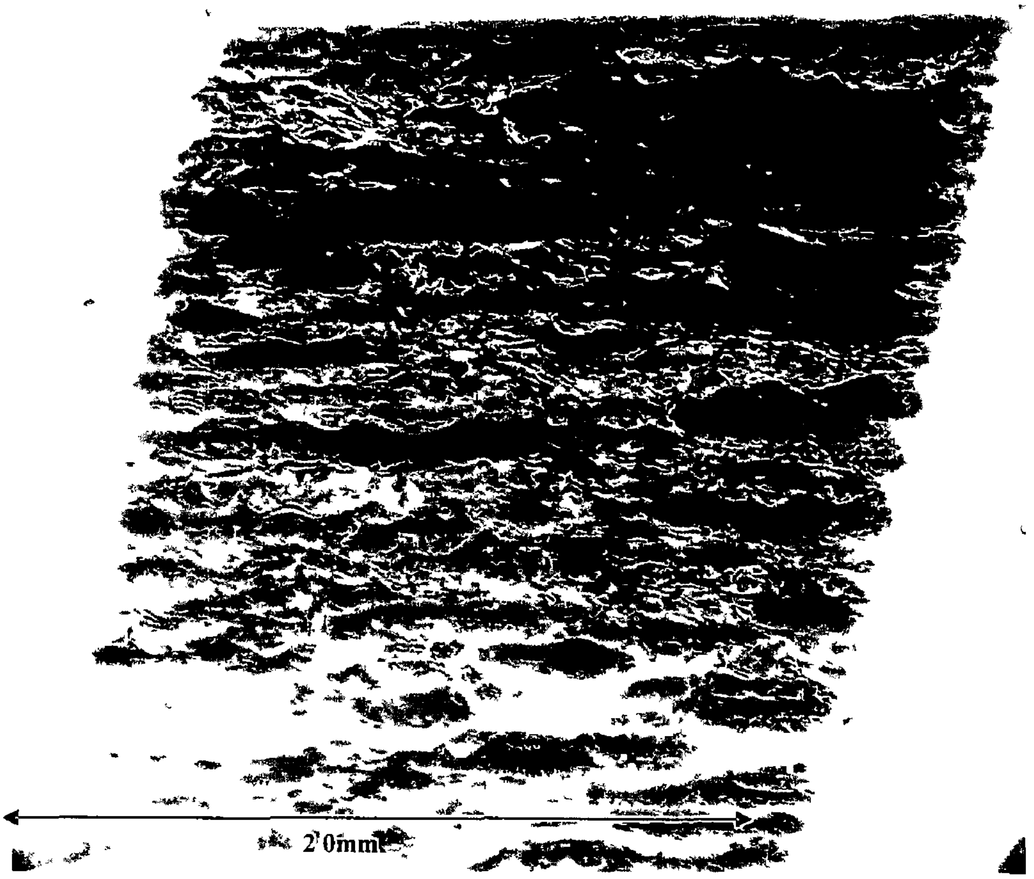

Fig A 8 Si-SiGe 3-525, Grazing Incidence 0 05^0, Reflection 012

It has been observed that, for some strained epitaxial systems, the surface of the layer develops roughness or waviness, correlated spatially with the positions of the underlying misfit dislocations [o] The strain fields due to this waviness are being imaged in the total reflection topography mode

A 4 Micro-Raman Spectroscopy Results

Micro-Raman measurements were performed by a Jobin Yvon LabRam HR800 system in backscattering geometry using both a 488nm Ar$^+$ laser and a 325nm He-Cd UV laser excitation at room temperature An 100x (or 40x for the UV laser) objective was used to focus the laser source to a diameter of about 1μm on the sample surface The sample was placed on a motorized X-Y stage which enables the line scans The Raman signal from the sample was collected by the same objective and detected by a liquid nitrogen cooled CCD detector A confocal hole of 200μm and a grating of 1800g/mm were chosen for the experiment Before performing the measurements, the system was carefully calibrated with a reference unstrained Si sample The Raman spectra were averaged for three accumulation times to reduce noise effects In order to extract accurately the Si Raman peak position, the original experimental data was fitted with a Gauss/Lorentz function using the software provided by the manufacturer

The advantage of using two lasers is that it is possible to obtain depth dependent spectra The penetration depth d_p of the laser in the measured sample is estimated according the following equation [v],

$$d_p=2\ 3/(2\alpha)$$

where α is the absorption coefficient of the laser source in the measured sample Its value can be obtained via an interpolation of data listed in Aspnes and Studna [t] for Si and Ge crystals The calculated penetration depths for the 488 nm and 325nm lasers in Si and Ge crystals are listed in Table A1

For $Si_{1\ x}Ge_x$, the penetration depth depends on the composition and lies between the values of Si and Ge It can be estimated with the following equation [u],

$$d_{p\ SiGe}=(1-x)d_{p\ Si}+xd_{p\ Ge}$$

Crystal	Laser wavelength (nm)	Laser energy (eV)	$10^{3}\alpha$ (cm ^{1})	d_p (nm)
Si	325	3 81	1235 18	9
	488	2 54	20 61	558
Ge	325	3 81	1159 28	10
	488	2 54	605 94	19

Table A 1 Absorption coefficient (α) and penetration depth (d_p) in crystalline Si and Ge for 325 nm and 488 nm laser excitation sources

Assuming a Ge content of 30%, we get a penetration depth of ~397nm for the Ar^+ laser In effect this means that the Raman signal mostly comes from the $Si_{0 7}Ge_{0 3}$ region but there is also a small contribution from $Si_{0 75}Ge_{0 25}$ as shown schematically below

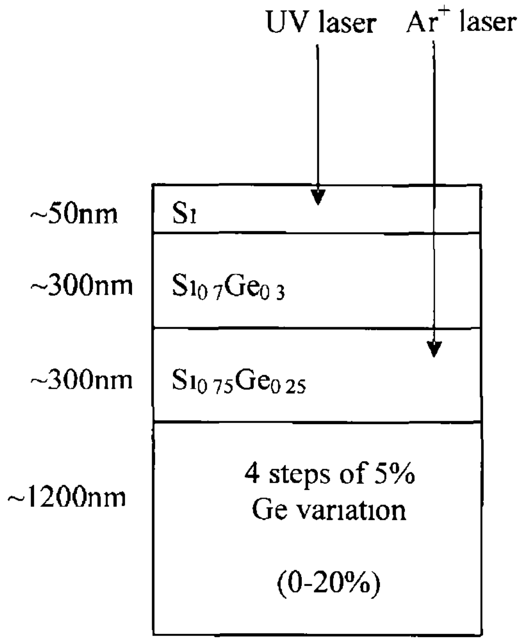

Fig A 9 Laser Penetration depth into sample

The penetration depth of the UV laser into the sample is calculated to be ~9nm. Since the extinction depth is quite small, the use of such a short-wavelength excitation enables the measurement of the Raman signal from the thin silicon cap layer without the interference of the underlying SiGe layer.

Figures A.10 and A.11 are examples of Raman spectra using the 488nm Ar^+ ion laser.

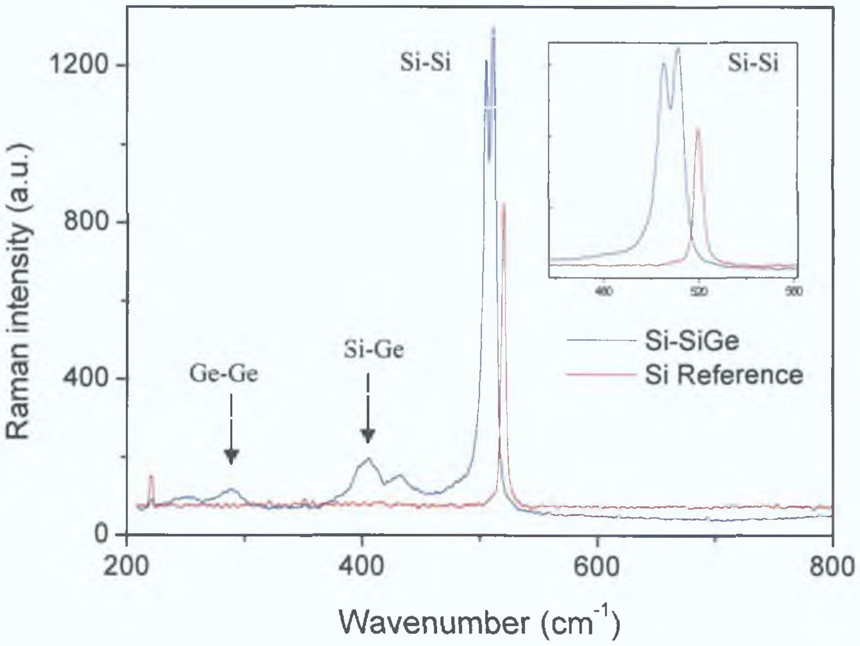

Fig. A.10 488nm Ar^+ laser, Raman Spectrum of unstrained reference Si and Si-SiGe Heterostructure. The inset shows clearly the shift in the Si-Si peak position.

The spectrum for the Si-SiGe sample is dominated by the Raman peak of the first order Si-Si mode at ~ 510cm^{-1} but peaks due to Si-Ge alloying and Ge-Ge modes at ~ 404cm^{-1} and ~ 290cm^{-1}, respectively, can also be identified. In the inset I have rescaled to show only the Si-Si modes. Two Si-Si peaks can be identified for the Si-SiGe structure and are clearly red-shifted compared to the reference unstrained Si sample in which the Si-Si mode appears at ~ 520cm^{-1}. The peak at ~512cm^{-1} arises from the strain-shifted Si-Si mode of the thin Si cap layer. A tensile biaxial stress in the Si cap layer was calculated from the downward shift in the Si Raman peak position, $\Delta\omega_{Si}$, using the equation $\sigma_{xx} = \sigma_{yy} = -\Delta\omega_{Si}/4$ (GPa) [v]. The average $\Delta\omega_{Si} = -8.02\text{cm}^{-1}$, therefore $\sigma_{xx} = 2.01$ GPa. The peak at ~ 505cm^{-1} is the Si-Si phonon mode peak of the $Si_{1-x}Ge_x$ buffer in which the Ge content induces a red shift of the Si-Si peak.

It is also possible to extract the Ge content of the Si-Ge buffer layer by analysing the ratio of the intensities of the Si-Ge and Ge-Ge modes which to a good approximation are independent of strain. These modes are shown in fig. A11.

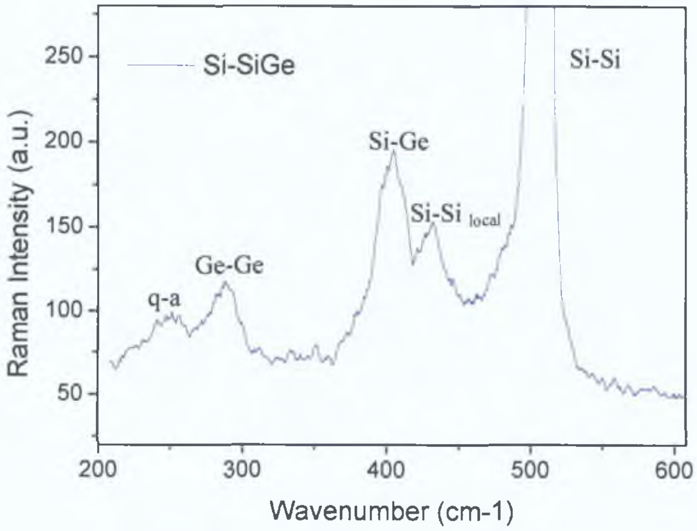

Fig. A.11 488nm Ar$^+$ laser, Raman Spectrum of Si-SiGe Heterostructure.

On the high energy side of the main Si-Ge mode at ~ 400cm^{-1} a peak appears at ~ 426 cm^{-1} which has been attributed to a local Si-Si vibration perturbed by Ge [w] A broad feature (labeled as q-a), on the low energy side of the Ge-Ge mode is generally termed as 'quasi-amorphous' because a similar feature is reported in amorphous $Si_{1-x}Ge_x$ alloys The ratio of the intensities of the Si-Ge (I_{Si-Ge}) and Ge-Ge (I_{Ge-Ge}) modes can be used to calculate the Ge content x according to

$$I_{Si-Ge} / I_{Ge-Ge} = 2(1-x)/Bx$$

where the coefficient B =2 218 is related to the Bose factor and the frequencies of Ge-Ge and Si-Ge optical modes of the alloy [x,y] Using this relationship the Ge content is estimated as ~27% This is slightly lower than the planned Ge content of 30% However it should be noted that the determination of the Ge content by analysing Si-Ge and Ge-Ge intensity ratios is complicated by the low intensity quasi-amorphous features which make it difficult to analyse the peaks accurately using standard curve-fitting procedures This can be circumvented by using polarization techniques [w] but such facilities were not available at the time of these studies

Fig A 12 below shows an example of the Raman spectra obtained with the UV laser for the Si-SiGe heterostructure compared to that of a reference unstrained silicon sample As the laser penetration depth is ~ 9nm, the entire signal is from the thin Si cap layer In agreement with the results of the Ar^+ laser, there is a clear red shift in the Si Raman peak position of the strained Si cap compared to that of the reference unstrained Si sample indicating that a tensile stress is present in the Si cap layer

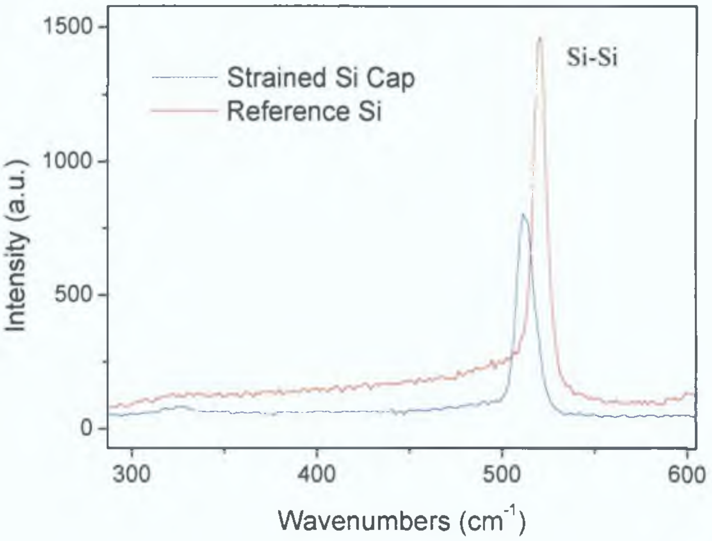

Fig. A.12 325nm UV laser, Raman Spectrum of Si-SiGe Heterostructure.

It is interesting to note that the Si-Si peak of the reference Si sample has a greater intensity than that of the strained Si layer for the same experimental conditions. The reference Si also has a narrower FWHM of 6.78 compared to 9.18 for the strained Si cap layer. This indicates that the crystalline quality of the LDCVD grown Si cap layer is not as good as that of a standard Si wafer.

In order to extract accurately the Si-Si peak position, a line scan was performed over a distance of ~100μm. The average Si-Si peak position is 512.8±0.1 cm^{-1}. From the average $\Delta\omega_{Si}$ value of -7.6 cm^{-1}, the tensile biaxial stress was calculated as before resulting in a value of 1.89±0.03 GPa. This value differs by about 6% from the result obtained using the Ar$^+$ 488nm laser, suggesting that there may be a slight relaxation in upper region of the ~50nm Si cap as we know that the signal of the UV laser is from the top 9nm while the visible laser penetrates into the SiGe buffer layer so the measured Si peak position is the average value over the entire Si cap In the case of a fully strained Si cap layer, the tensile stress σ_f in the Si cap can be calculated with the following equation [z]

$$\sigma_f = Y_f m/(1-v)$$

where Y_f is the film Young's modulus, m is the misfit between the film and the substrate lattice parameters and v is Poisson's ratio of the film The lattice constants of Si and Ge are 0 543088 nm and 0 565760 nm, respectively [aa] The lattice constant of a fully relaxed $Si_{0\,7}Ge_{0\,3}$ buffer layer was estimated from Vegard's law to be 0 54989 nm, and therefore the misfit between the Si cap and SiGe buffer layer is ~ 1 24% Thus the tensile stress for a fully strained Si layer on $Si_{0\,7}Ge_{0\,3}$ is calculated as 2 24GPa However, the Raman measurements have indicated that the Ge content is only ~ 27% The theoretical stress of a strained Si layer grown on a buffer with 27% Ge concentration is 2 02GPa This is in close agreement with the stress value extracted using the Ar^+ laser confirming that the SiGe buffer layers are fully relaxed and that at least close to the Si-SiGe interface the Si cap layer is fully strained

A 5 Conclusions

Synchrotron x-ray topography reveals a high density of misfit dislocations in the Si-SiGe strain-relaxed buffer down to a penetration depth of 37 4μm At an incidence angle of 0 05° the x-rays approach the sample surface at grazing angles below the critical angle for a number of reflections and we see a "bumpy" structure no more than nominally 10Å from the surface resulting from the strain fields related to the underlying misfit dislocations Micro-Raman spectroscopy estimates the Ge content at ~27% The average strain in the Si cap layer is ~2GPa UV laser measurements indicate a small strain relaxation of ~ 6% in the top 10nm of the 50nm Si cap layer

A 6 References

a L Di Gaspare, A Notargiacomo, F Evangelisti, E Palange, S Pascarelli and J Susini, *Solid State Communications* **122**, 359 (2002)

b W M Chen, G D M Dilliway, P J McNally, T Tuomi, A F W Willoughby and J Bonar, *J Mater Sci Mater Elect*, **14**, 455 (2003)

c The International Technology Roadmap for Semiconductors, (2003)

d I De Wolf, *Semicond Sci Technol* **11**, 139 (1996)

e M Sauvage and J F Petroff, " Application of Synchrotron Radiation to X-Ray Topography" in *Synchrotron Radiation Research*, H Winick and S Doniach, Editors, Plenum Press, New York, pp 607-638 (1980)

f P J McNally, J Curley, A Krier, Y Mao, J Richardson, T Tuomi, M Taskinen, R Rantamaki, E Prieur and A, Danilewsky, *Semicond Sci Technol* **13**, 345 (1998)

g A N Danilewsky, R Simon, A Fauler, M Fiederle and K W Benz, *Nuclear Instruments and Methods in Physics Research Section B Beam Interactions with Materials and Atoms*, **199**, 71(2003)

h W M Chen, P J McNally, Yu V Shvydko, T Tuomi, M Lerche, A N Danilewsky, J Janatharana, D Lowney, M O'Hare, L Knuuttila, J Riikonen and R Rantamaki, *phys stat sol (a)*, **186** (3), 365 (2001)

i R Rantamaki, T Tuomi, Z R Zytkiewicz, J Domagala, P J McNally and A N Danilewsky, *J Appl Phys*, **86**, 4298 (1999)

j A N Danilewsky , A Fauler , M Fiederle , P McNally , L O'Reilly and R Simon, *3rd ANKA Users Meeting 23-24September*, 2004, Karlsruhe

k A N Danilewsky, P McNally, L O'Reilly, T Tuomi, A Lankinen and R Simon, *2nd ANKA Users Meeting 16-18 September*, 2003, Karlsruhe

l A Lankinen, T Tuomi, J Riikonen, L Knuuttila, H Lipsanen, M Sopanen, A Danilewsky, P J McNally, L O'Reilly, Y Zhilyaev, L Fedorov, H Sipila, S Vaijarvi, R Simon, D Lumb, A Owens, *J Cryst Growth* **283**, 320 (2005) m T Tuomi, *J Synchr Radiation* 9, 174 (2002)

n J Riikonen, T Tuomi,, A Lankinen, J Sormunen, A Saynatjoki, L Knuuttila, H Lipsanen, P J McNally, L O'Reilly, A Danilewsky , H Sipila, S Vaijarvi, D Lumb, A Owens, *J Mater Sci Mater Electron* **16**, 449 (2005)

o Patrick J McNally, G Dilliway, J M Bonar, A Willoughby, T Tuomi, R Rantamaki, A N Danilewsky and D Lowney, *J X-Ray Sci Technol* , **9**, 121 (2001)

p Patrick J McNally, G Dilliway, J M Bonar, A Willoughby, T Tuomi, R Rantamaki, A N Danilewsky and D Lowney, *Appl Phys Lett* , 77 (11), 1644 (2000)

q [online] <http //www ccp14 ac uk/ccp/web-mirrors/lmgp-laugier-bochu/ > (Accessed on 22/06/04)

r P J McNally, R Rantamaki, T Tuomi, A N Danilewsky, D Lowney, J W Curley and P A F Herbert, *IEEE Transactions on Components and Packaging Technologies,* **24**, 76 (2001)

s P J McNally, G Dilliway, J M Bonar, A Willoughby, T Tuomi, R Rantamaki, A N Danilewsky and D Lowney, *J X-ray Sci Technol , 9,* 121 (2001)

t D E Aspnes, A A Studna, *Phys Rev B,* **27**, 985 (1983)

u European Commission, Raman and Luminescence Spectroscopy for Microelectronics, Catalogue of optical and physical parameters "Nostradamus" project SMT4-CT-95-2024 (1998)

v I De Wolf, *Semicond Sci Technol* **11**, 139 (1996)

w S Rath, M L Hsieh, P Etchegoin and R A Stradling, *Semicond Sci Technol* **18**, 566 (2003)

x L Xu, P J McNally, G D M Dilliway, N E B Cowern, C Jeynes, E Mendoza, P Ashburn, D M Bagnall, *J Mater Sci Mater Electron* **16**, 469 (2005)

y J L Liu, J Wan, Z M Jiang, A Khitun, K L Wang and D P Yu, *J Appl Phys* **92**, 6804, (2002)

z B Pichaud, M Putero and N Burle, *phys stat sol (a)* **171**, 251 (1999)

aa Bruker Advanced X-Ray Solutions, Powder Diffraction files (www iccd com)

Appendix B

Micro-Raman Study of Self-Assembled Ge Quantum Dots on Silicon

B 1 Introduction

Nanometer-sized particles show unique electrical and optical properties due to quantum confinement effects, which are not observed in bulk materials [1] One growth method is by self-assembly of nano-sized islands by strained epitaxial growth of a semiconductor of a larger lattice constant on a semiconductor of smaller lattice constant, e g Germanium on Silicon Obtaining quantum structures through self-organisation has the advantage of enabling fabrication of electronic and optical devices of smaller dimensions than accessible by lithography Understanding the process of self-assembly of Ge nanostructures on Si with controlled size distribution is a key requirement for their application to devices Micro-Raman spectroscopy was used to investigate samples of self-assembled Ge quantum dots grown by low-pressure chemical vapour deposition (LPCVD) using the parameters in Table B 1 The samples were prepared in Southampton University's Microelectronics Centre by Dr Gabriela Dilliway

Sample Number	Si (for 20 mins) Temperature (°C)	Ge Temperature (°C)	Time (s)
5367	900	650	10
5368	900	650	5
5369	900	650	7.5

Table B.1. LPCVD-grown Ge islands on epi Si on (001) Si wafer: growth parameters

Prior to Ge island growth, a 500nm thick Si buffer layer was grown on an n-type (001) Si wafer to ensure an inhomogeneity free growth surface. The size and shape of the samples depend on the growth duration. Figures B.1-3 are atomic force microscopy (AFM) images taken from Dilliway *et al.* [ii] showing the structural characteristics of the three different samples.

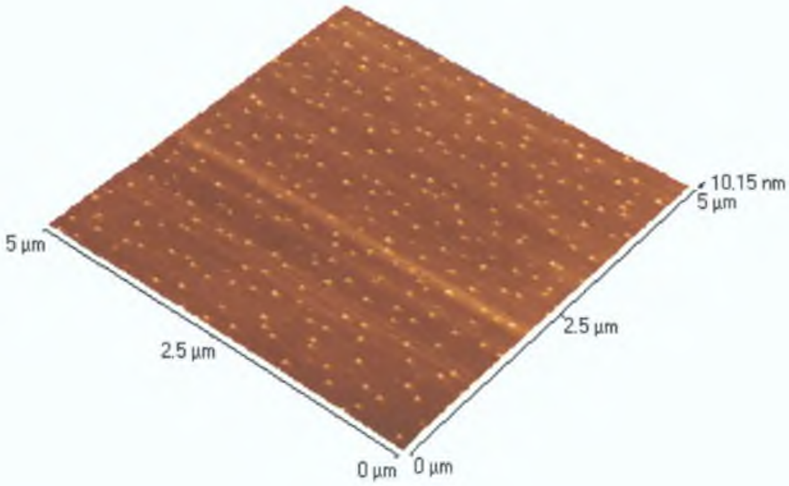

Fig. B.1 3D AFM images of 5 x 5 μm^2 scanned area of sample 5368, the shortest growth duration sample

For the shortest growth duration of five seconds, small ‘lens-shaped’ islands with a surface density of ~16μm^{-2} and a narrow size distribution, ranging from 20-30nm in width and 2-4nm in height were grown.

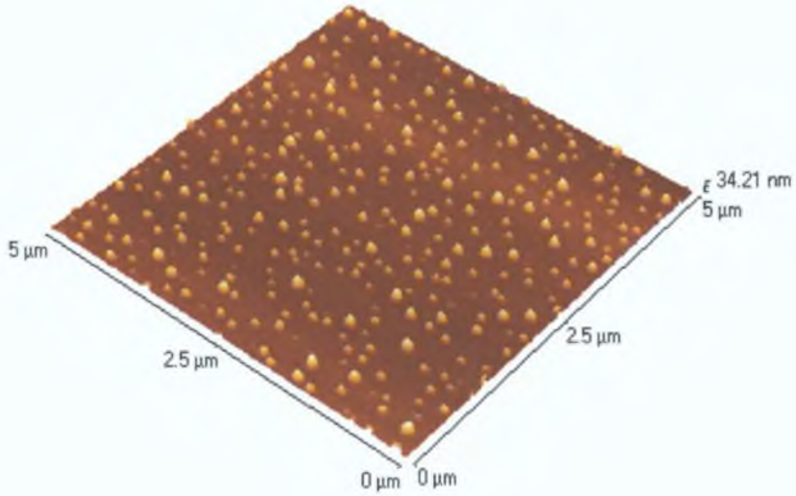

Fig. B.2 3D AFM images of 5 x 5 μm^2 scanned area of sample 5369, the intermediate growth duration sample.

Increasing the growth duration to 7.5 seconds resulted in the deposition of a mixed population of small and larger ‘lens-shaped’ islands. The total surface density of ~19μm^{-2} has not significantly increased compared to that seen for the shortest growth duration, but the islands have generally increased in size. Most islands are between 100-150nm in width and 10-25nm in height.

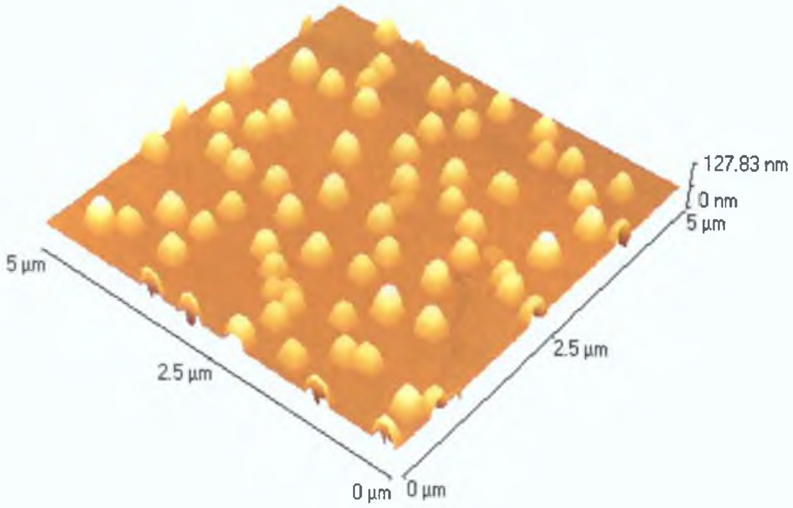

Fig. B.3 3D AFM images of 5 x 5 µm^2 scanned area of sample 5367, the longest growth duration sample.

Growth for 10 seconds leads to a dramatically different island shape and distribution. The island surface density has fallen to just ~3µm^{-2} and the shape of the islands are large square-based truncated pyramids. The majority of the islands are ~250nm wide and have increased to ~50nm high.

B.2 Micro-Raman Spectroscopy Results

Micro-Raman Spectroscopy was used to investigate the influence of the growth duration at 650°C on the composition and strain effects in the LPCVD-grown self-assembled Ge islands on (001) Si substrates. As for Appendix A, a Jobin-Yvon LabRam800 system was used in backscattering mode (laser beam and scattered light are perpendicular to the sample plane) with a 488 nm Ar$^+$ laser as previously described. The laser was focused to a diameter of approximately 1µm on the sample surface and penetrates into the sample at least as far as the silicon substrate. Each sample was scanned in a number of different positions on the sample and it was found that the Raman spectra did not vary significantly from point to point within the sample. Some small variations in intensity and position were evident arising from the slight difference in the size and shape of the islands across the sample, with the strongest Ge signal coming from the largest islands. A control spectrum of bare unprocessed silicon was also recorded under exactly the same experimental conditions. Typical spectra are shown in fig.B.4.

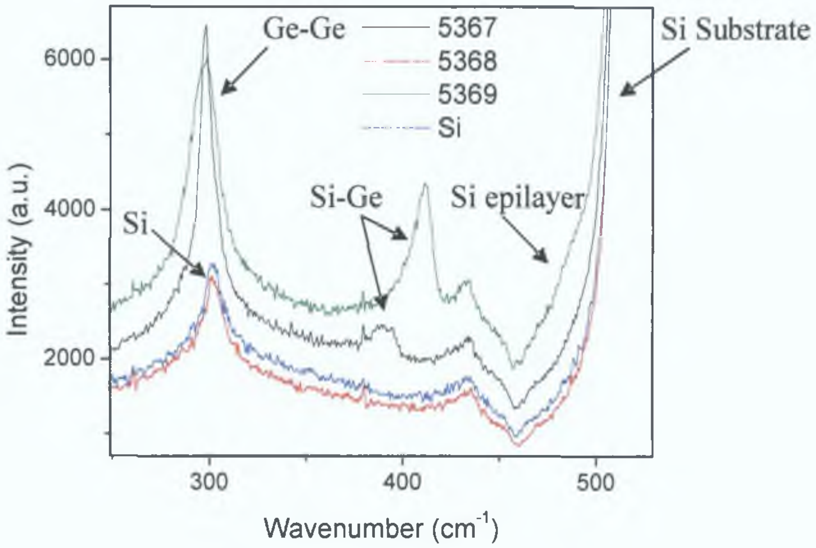

Fig. B.4 Raman spectra using 488nm Ar$^+$ laser for samples 5367, 5368 and 5369, islands of longest, shortest and intermediate growth duration, respectively, together with a spectrum for a reference Si sample.

The two most important Si-Si peaks, located at ~520cm^{-1} and ~300cm^{-1}, are visible in the control spectrum (we show only the flank of the very strong Si peak at 520 cm^{-1}). The intensity of the main TO-LO triply degenerate silicon substrate peak at 520.0cm^{-1} is saturated (greater than 64000 a.u.). This dominates the spectra making it difficult to detect any individual signal from the thin (~500nm) layer of epi silicon, which would appear, as a peak at approximately 500cm^{1} [iii] The spectrum for the small Ge islands of shortest growth duration (5368) is almost identical to that of the control Si There seems to be little doubt that the small peak we see at ≈ 302cm^{1} is in fact from the silicon substrate and cannot be attributed to a Ge-Ge mode This implies that either the Ge is not present (unlikely as small lens-shaped islands are seen in AFM, fig B1) or, that there is little interaction of the exciting source with the Ge islands The presence of a silicon peak around ~302cm^{1} due to a two phonon transverse acoustic (TA) mode has been reported [iv] and has been known to dominate the spectrum from germanium quantum structures [v] This appears to be the case for this sample It is also worth noting that a peak also occurs at ~ 433cm^{1} in the spectrum of the Si substrate also due to a two phonon TA Si mode

A baseline correction was applied to the spectrum followed by a Gauss/Lorentz band-fitting algorithm in order to accurately extract the Ge-Ge and Si-Ge peak position, amplitude and full width at half maximum (FWHM) For the truncated pyramidal islands resulting from the longest growth duration (5367) the position of the Ge-Ge peak is 298 15cm^{1} This is slightly red-shifted compared to the expected value of ~301cm^{1} for an unstrained bulk Ge sample [vi] The Ge-Ge peak is relatively narrow with an extracted FWHM of 7 96cm^{1}, indicating that the Ge is crystalline in nature A small peak around 389 6cm^{1} is most likely due to a Si-Ge mode resulting from the intermixing of the two compounds [vii]

The Raman spectrum for the intermediate growth duration, larger 'lens-shaped' Ge islands (5369) is compared to that of the other samples Unlike the longer growth duration sample (5367) another peak is now clearly evident at approximately 410cm^{1} This is attributed to a Si-Ge mode resulting from substantial intermixing of Si and Ge in the islands In this case the Ge-Ge mode appears at 297 12cm^{1} Comparing the Ge-Ge Raman peak position of the Ge islands to that of a totally unstrained Ge-Ge mode which appears at 300 65cm^{1} [viii] we detect a red-shift of –3 53cm^{1} and –2 41cm^{1} for the islands of intermediate (5369) and longest (5367) growth duration respectively, indicating that there is a small tensile stress in the Ge islands In fig B4 we can see that the Ge-Ge mode of the intermediate growth duration sample is much broader than that of the longest growth duration This is reflected in a FWHM value of 13 49cm^{1} This suggests that the large pyramidal shaped islands (5367) are the most crystalline (i e contain the largest crystals as expected) as they have a smaller FWHM (7 96cm^{1}) than the sample with a mixture of small and large lens-shaped islands (5369) The ratio of the intensities of the Si-Ge ($I_{Si\ Ge}$) and Ge-Ge ($I_{Ge\ Ge}$) modes can be used to calculate the degree of Si and Ge interface intermixing according to

$$I_{Si-Ge}/I_{Ge-Ge}=2(1-x)/Bx$$

where x is the average Ge concentration and B is 2 218 [iv,ix] Using this relation the large pyramidal islands are estimated to have a Ge content of ~88%, and the 'lens-shaped' islands, which experience greater intermixing with Si have a Ge content of ~55%

As both the Ge-Ge and Si-Ge Raman modes are overlapping with the two phonon TA Si modes, we have subtracted the characteristic Si background from the spectra of the Ge islands as shown in fig. B.5.

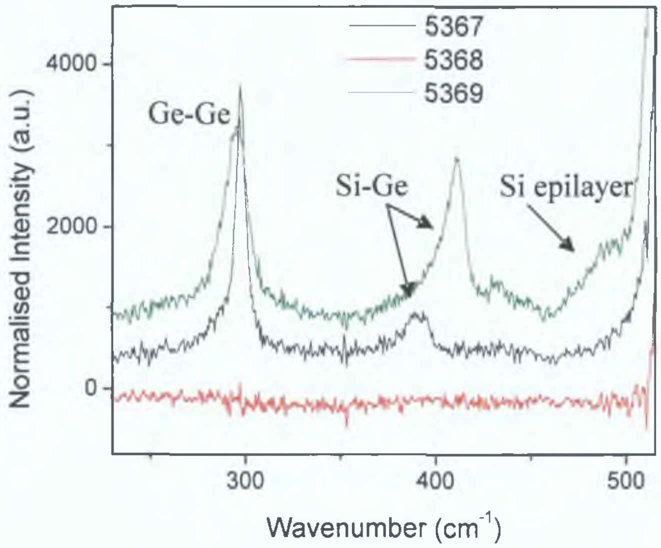

Fig. B.5 Raman spectra for the three samples after removal of the Si background.

The removal of the Si background allows us to inspect closely the interaction of the deposited Ge with the underlying Si. Three peaks of interest remain: one at ~ 297 cm^{-1}, which although close to the Si-Si 302 cm^{-1} peak, is in fact attributable to a Ge-Ge mode [iii,x,xi,v], one at ~400 cm^{-1}, which is attributable to a Si-Ge mode [iii,xii], and a small flank at ~485 cm-^{1}, especially visible for the islands of intermediate growth duration, which is a Si-Si mode in the epilayer [iii]. For the case of the small islands of shortest growth duration (5368), the Ge-Ge and Si-Ge modes are absent, confirming that the very small Ge islands present in this sample could not be detected. For the longest growth duration islands (5367), the two Ge-related modes are now observed at ~ 297 cm^{-1} and

391cm^{1} As before, the sample of intermediate growth duration (5369) has a well-defined peak at 410 89cm^{1} that is attributed to the Si-Ge mode and a Ge-Ge mode peak at ~ 295cm^{1} The Ge-Ge peaks appear at lower wavenumbers compared to the unsubtracted spectra which were influenced by the Si Raman peak at ~ 302cm^{1} The Ge peak position was calibrated using an intense plasma line, which appears at approximately 221cm^{1}, as an internal reference The ratio of the intensities of the Ge-Ge and Si-Ge modes were used as before to estimate the Ge content in the islands For the corrected spectra the Ge content is estimated at 78% for the large truncated pyramidal islands and 50% for the 'lens-shaped' islands The Si epilayer peak at ~485 cm^{1} is absent in the large island case, which is consistent with greater 488 nm light absorption in the islands to the detriment of the Si epilayer peak [iii] The Si-Ge peak for the larger islands is broader in width and is shifted to lower wavenumbers (i e 411 cm^{1} *vs* 391 cm^{1}) when compared to the intermediate island case This is suggestive of (i) perhaps greater dislocation densities in the large islands and/or (ii) that quantum confinement effects may be significant for the smaller island distributions [xiii]

If the Ge concentration is known, the value of in-plane strain in Ge islands can be estimated using the expression for the Ge-Ge peak position in a Si-Ge alloy according to

$$\omega_{Ge-Ge} = 282\ 5 + 16x - 384\varepsilon$$

where ε is the strain in the Ge islands [xiv] Using the Ge content calculated above, and the Ge-Ge peak position extracted by band-fitting, the strain in the islands is estimated as -0 57% for the large truncated pyramidal islands and -1 24% for the 'lens-shaped' islands There seems to be a greater compressive strain in the lens-shaped islands of intermediate size than in the large pyramidal islands This may suggest that as the island grows larger it is less constrained by the smaller lattice constant of silicon (a_{Si} = 0 543nm, a_{Ge}= 0 566nm) and therefore more relaxed Lattice relaxation in the large pyramidal islands may also have occurred through generation of misfit dislocations, which have been detected in cross-sectional transmission electron microscopy measurements of the sample [11]

B 3 Conclusions

Micro-Raman spectroscopy could not be used to analyse Ge islands with sizes of 20-30nm wide and 2-4 nm in height as the spectrum was dominated by the silicon substrate obscuring any signal from the Ge islands A Ge-Ge Raman peak at approximately 297 cm ^{1} is seen for the sample of longest growth duration (5367) indicating the presence of germanium islands It is likely that a broad peak appearing around 391cm ^{1} is a signal from a Si-Ge mode, indicating a weak intermixing of Si and Ge The germanium content is approximately 78% For the sample of intermediate growth duration (5369) we see a Ge-Ge Raman peak at 295cm ^{1} and a Si-Ge Raman peak at 411cm ^{1} The relative intensities of these peaks indicate that there is considerable alloying with silicon in the islands The germanium content of the islands is estimated at 50% A red-shift of – 3 48cm^{-1} and –5 36cm ^{1} compared to the position of strain free bulk Ge, is seen for the islands of longest (5367) and intermediate (5369) growth duration, respectively Calculation of the strain indicates that both the large pyramidal and smaller lens-shaped islands are compressively strained Greater strain relaxation in the case of the large islands is probably due to the generation of dislocations at the Si – Ge interface

B 4 References

i P Holister, C Roman, T Harper, *Cientifica Quantum Dots Technology White Papers* **nr 13**, (2003)

ii G D M Dilliway, N E B Cowern, C Jeynes, L O'Reilly, P J McNally, D M Bagnall, *Mat Res Soc Symp Proc* **775**, P9 25 1 (2003)

iii A Eshed, J Zhu, J Yan, R Beserman, A H Weiss, *Mat Res Soc Symp Proc* **696**, N 3 5 1 (2002)

iv L Xu, P J McNally, G D M Dilliway, N E B Cowern, C Jeynes, E Mendoza, P Ashburn, D M Bagnall, *J Mater Sci Mater Electron* **16**, 469 (2005)

v G B Wright *et al*, *Phys Rev Lett*, **18**, 607 (1967)

vi I De Wolf, *Semicond Sci Technol* **11**, 139 (1996)

vii P M Mooney, F H Dacol, J C Tsang and J O Chu, *Appl Phys Lett* **62**, 2069 (1993)

viii Landolt-Bornstein New Series III/22a

ix J L Liu, J Wan, Z M Jiang, A Khitun, K L Wang and D P Yu, *J Appl Phys*, **92**, 6804, (2002)

x T Kobayashi, T Endoh, H Fukuda, S Noamura, A Sakai, Y Ueda, *Appl Phys Lett*, **71**, 1195 (1997)

xi X L Wu, T Gao, X M Bao, F Yan, S S Jiang, D Feng, *J Appl Phys* **82**, 2704 (1997)

xii P M Mooney, F H Dacol, J C Tsang and J O Chu, *Appl Phys Lett*, **62**, 2069 (1993)

xiii P M Fauchet and I H Campbell, *CRC Critical Reviews in Solid State and Materials Sciences* **14**, S79, Suppl 1 (1988)

xiv J Groenen, R Carles, S Christiansen, M Albrecht, W Dorsch, H P Strunk, H Wawra and G Wagner, *Appl Phys Lett* **71**, 3856 (1997)